RECONFIGURABLE MICROSTRIP BANDPASS FILTERS, PHASE SHIFTERS USING PIEZOELECTRIC TRANSDUCERS, AND BEAM-SCANNING LEAKY-WAVE ANTENNAS

A Dissertation

by

CHAN HO KIM

Submitted to the Office of Graduate Studies of
Texas A&M University
in partial fulfillment of the requirements for the degree of

DOCTOR OF PHILOSOPHY

May 2012

Major Subject: Electrical Engineering

Reconfigurable Microstrip Bandpass Filters, Phase Shifters Using Piezoelectric Transducers, and Beam-scanning Leaky-wave Antennas

RECONFIGURABLE MICROSTRIP BANDPASS FILTERS, PHASE SHIFTERS USING PIEZOELECTRIC TRANSDUCERS, AND BEAM-SCANNING LEAKY-WAVE ANTENNAS

A Dissertation

by

CHAN HO KIM

Submitted to the Office of Graduate Studies of
Texas A&M University
in partial fulfillment of the requirements for the degree of

DOCTOR OF PHILOSOPHY

Approved by:

Chair of Committee,	Kai Chang
Committee Members,	Robert D. Nevels
	Laszlo B. Kish
	Kenith Meissner
Head of Department,	Costas N. Georghiades

May 2012

Major Subject: Electrical Engineering

ABSTRACT

Reconfigurable Microstrip Bandpass Filters, Phase Shifters Using Piezoelectric Transducers, and Beam-scanning Leaky-wave Antennas. (May 2012)

Chan Ho Kim, B.E., Chung-Ang University, Seoul, Korea;

B.E., Korea University, Seoul, Korea;

M.S., University of Maryland, College Park

Chair of Advisory Committee: Dr. Kai Chang

In modern wireless communication and radar systems, filters play an important role in getting a high-quality signal while rejecting spurious and neighboring unwanted signals. The filters with reconfigurable features, such as tunable bandwidths or switchable dual bands, also play a key part both in realizing the compact size of the system and in supporting multi-communication services. The Chapters II-IV of this dissertation show the studies of the filters for microwave communication. Bandpass filters realized in ring resonators with stepped impedance stubs are introduced. The effective locations of resonant frequencies and transmission zeros are analyzed, and harmonic suppression by interdigital-coupled feed lines is discussed. To vary mid-upper and mid-lower passband bandwidths separately, the characteristic impedances of the open-circuited stubs are changed. Simultaneous change of each width of the open-circuited stub results in variable passband bandwidths. Asymmetric stepped-impedance resonators are also used to develop independently controllable dual-band (2.4 and 5.2

GHz) bandpass filters. By extending feed lines, a transmission zero is created, which results in the suppression of the second resonance of 2.4-GHz resonators. To determine the precise transmission zeros, an external quality factor at feeders is fixed while extracting coupling coefficients between the resonators. Two kinds of feed lines, such as hook-type and spiral-type, are developed, and PIN diodes are controlled to achieve four states of switchable dual-band filters.

Beam-scanning features of the antennas are very important in the radar systems. Phase shifters using piezoelectric transducers and dielectric leaky-wave antennas using metal strips are studied in the Chapters V-VII of this dissertation. Meandered microstrip lines are used to reduce the size of the phase shifters working up to 10 GHz, and reflection-type phase shifters using piezoelectric transducers are developed. A dielectric film with metal strips fed by an image line with a high dielectric constant is developed to obtain wide and symmetrical beam-steering angle.

In short, many techniques are presented for realizing reconfigurable filters and large beam-scan features in this dissertation. The result of this work should have many applications in various wireless communication and radar systems.

DEDICATION

To my parents

and

my wife, Chan Yee

ACKNOWLEDGEMENTS

I would like to express my sincere appreciation to my advisor Dr. Kai Chang for his guidance and support with regards to my graduate studies and research. My appreciation also goes to Dr. Robert D. Nevels, Dr. Laszlo B. Kish, and Dr. Kenith Meissner for serving as my committee members and for their helpful comments and advice.

I would also like to thank all of the members of Electromagnetics and Microwave Laboratory at Texas A&M University. I deeply thank Mr. Ming-Yi Li for his outstanding technical assistance with my research.

I would like to express thanks to Dr. Lei Zhu in Nanyang Technological University for giving me valuable opportunities to review many good papers.

I would also like to express my gratitude to my beloved wife, Chan Yee, for her thoughtful consideration and great support during this long period of my graduate studies.

Finally, I would like to thank my father and mother for their ceaseless prayer, without which this work would not have been possible.

TABLE OF CONTENTS

CHAPTER Page

LIST OF FIGURES

FIGURE Page

FIGURE Page

FIGURE Page

FIGURE Page

LIST OF TABLES

CHAPTER I

INTRODUCTION

The microwave bandpass filters are important components in wireless communication and radar systems. They are designed to control the frequency response of transmitted or received wireless signals with low loss while avoiding interferences with neighboring unwanted signals. As there are many frequency bands providing various services in modern communication frequency spectrums, the role of the microwave bandpass filters is very essential. The requirements of the modern filter technologies include not only the features of low insertion losses, sharp cutoff rejections, wide stopbands, and multi-passbands, but also the reconfigurable characteristics such as tunable passband bandwidths and switchable multi-bands.

Reconfigurable microwave bandpass filters especially have many advantages to meet the demands of modern communication and radar systems. The filters with features of controllable passband bandwidths can contribute toward realizing compact-size systems and can support multi-communication services at the same time. The capabilities of the reconfigurable filters with separate control of mid-lower or mid-upper passband bandwidths could add much more applications to the current reconfigurable filters. Besides, the multi-band filters with the capabilities of switching on or off each band separately, are able to provide multi-service applications and flexible control of each band simultaneously.

The journal model for this dissertation is *IEEE Transactions on Microwave Theory and Techniques*.

Over the last decade, the applications of the bandpass filters to cover an ultra-wideband (UWB) spectrum from 3.1 GHz to 10.6 GHz have become highly interesting topic in academic and industrial researches. The technologies of the UWB filters avoiding the interference with the existing diverse communication service spectrums have also been researched inevitably. Asymmetric structures of the feed lines for the microstrip bandpass filters are introduced to create a notch band within UWB spectrum in this work.

Ring and stepped-impedance resonators have been widely used for many decades in the filter applications because of their good performance of a low insertion loss, a sharp rejection, and features of the reconfigurable passbands. In this dissertation, they have been mainly used for the fabrications of the microstrip filters, and their characteristics of resonant frequencies and the location of transmission zeros are analyzed. External quality factors and coupling coefficients are calculated and compared to the simulated results in order to achieve the precise positioning of the transmission zeros.

In satellite communication and radar systems, beam-scanning capabilities of the antennas are principal to detect moving targets. For the one-dimensional linear array, scanning angle θ_0 is expressed by

$$\theta_0 = \sin^{-1}\left(\frac{\Phi}{k_0 d}\right) \tag{1}$$

where Φ is the progressive phase shift across the phased array, k_0 is the propagation constant in free space, and d is the element spacing between two antenna elements [1].

This equation shows that the phase shifters are very significant components to make scanning beams because they provide progressive phase shift Φ to each element of the phased antenna array. Therefore, making large progressive phase shifts with the features of a compact circuit size, a low loss, and wideband applications is critical requirements in the phase shifters. Over the last decade, techniques of the perturbation on microstrip lines, controlled by piezoelectric transducers (PETs), have shown good performance in the application to the phase shifters. In this dissertation, meandered microstrip lines are designed to miniaturize the conventional phase shifter using the PET, and the PET-controlled techniques are also applied to the reflection-type phase shifters. Moreover, dielectric leaky-wave antennas with wide beam-scan capabilities are discussed. A fan-shaped beam is radiated into space due to the perturbation of the metal strips on top of an image line. Both the feasible cross-section size and the dielectric constant of the image line are determined by appropriate trade-off among the characteristics of a wide beam scan angle, which is symmetric to the broadside radiation, and a single mode operation. By alternating the spacing of the metal strips, perturbing the image line, the beam scanning effects are clearly demonstrated in *E*-plane at 31 GHz.

This dissertation consists of eight chapters. Chapter II presents a wideband ring bandpass filter with switchable passband bandwidths, which uses multiple stepped open-circuited stubs and interdigital-coupled feed lines. Analyses of the resonant frequencies and transmission zeros are presented to optimize the design of the stepped open-circuited stubs. Chapter III presents an application of the ring resonator with the open-circuited stubs to ultra-wideband bandpass filters. A notched band is also achieved by using

asymmetric feed structures. Chapter IV introduces microstrip bandpass filters using asymmetric stepped-impedance resonators, which create independently controllable dual bands. Two kinds of feed lines are developed and optimized both for achieving wide stopbands and for positioning of PIN diodes. Chapter V describes miniaturized phase shifters, using meandered microstrip lines, controlled by a piezoelectric transducer. Their measured results are compared with those of the conventional phase shifters using straight microstrip lines. Chapter VI introduces reflection-type phase shifters controlled by a piezoelectric transducer. A quadrature coupler is used to combine reflected signals from the open-circuited microstrip lines under the dielectric perturbation. Chapter VII presents leaky-wave antennas using metal strips on top of an image line. Symmetric and wide beam-scan angle is achieved by using high dielectric-constant material in the image line. Chapter VIII summarizes the whole results of the studies in this dissertation.

CHAPTER II

RING RESONATOR BANDPASS FILTER WITH SWITCHABLE BANDWIDTH USING STEPPED-IMPEDANCE STUBS*

1. Introduction

The bandpass filters (BPFs) with the characteristics of a sharp rejection, a low insertion loss, and a tunable passband have wide applications in various communication and radar systems. For these BPFs to be realized, microstrip stepped-impedance resonators (SIRs) and microstrip ring resonators have effectively been used [2]-[14]. Firstly, since a design formula was introduced for the BPF using SIRs [2], many different SIR BPFs have been investigated. Ultra-wideband BPFs with five resonant frequencies with parallel-coupled feed lines [3], Quasi-Chebyshev BPFs of order up to 9 [4], and the SIR adding four tapped stubs with the effect of sharp rejections at cutoff regions [5] were proposed. The asymmetric SIR with one-step discontinuity has achieved a wide stopband by using tapped ports [6]. Secondly, the ring resonators have been used in many BPFs. An analyzing method of resonances in the ring resonator perturbed by an impedance step was discussed in [7], and a periodic stepped-impedance ring resonator was used for designing dual-mode miniaturized BPFs [8]. By tuning the stubs attached on a square ring resonator with dual-mode effects, a wide passband, sharp rejections, and increased stopband bandwidth [9] were achieved. Also, rectangular

perturbation elements were used to perturb the ring resonator [10], and interdigital-coupled feed lines were used to add two transmission zeros outside of the passband [11].

Moreover, reconfigurable filters have received increasing attention to meet the various demands of wireless communication and radar systems. Many researches on reconfigurable filters have been conducted to switch center frequencies of the passband while keeping low in-band insertion losses and high rejection levels. Recently, in addition to this typical center-frequency tuning filter, the BPF with tunable bandwidths has attracted attention to be used as a means to provide multi-functional and flexible communication services. Usually, PIN diodes [15]-[19] or varactors [20] have been used to tune the passband bandwidth. Wide discrete passband ratio, which is 3:1, was presented with a center frequency at 10 GHz, but 8 PIN diodes resulted in the complexity of bias circuits [15]. The signal distortion resulting from the nonlinearity of the PIN diodes was investigated in [16]. The switching mechanisms of the PIN diodes for connecting a tuning stub, an open loop, or short stubs with the rest of the circuits were presented in [17]-[19], respectively. In addition, the simultaneous tunings in both the bandwidth and the center frequency were achieved by using coupling reducers implemented by varactors [20].

In this chapter, the ring resonator with multiple open stubs is introduced to exhibit the tunability of the passband bandwidth. Even- and odd-mode equivalent circuits of the ring are used to calculate the resonant frequencies, and *ABCD*- and *Y*-parameters are calculated to achieve transmission zeros. Both the length and the characteristic impedance of the stepped open-circuited stubs are estimated by

investigating the passband variations according to the variations of the two parameters. As a result, the effects of the tunable bandwidth are obtained. The designs of the interdigital-coupled feed lines are made by comparing the frequency responses of the ring fed by direct-connected lines to those by the interdigital-coupled feed lines. After that, the method of switching bandwidth by alternating the characteristic impedances of each section of the stepped open stubs is presented. Finally, three states of the switching bandwidths are demonstrated by controlling the bias voltages to the PIN diodes. The proposed BPFs herein uses an RT/Duroid 6006 substrate with a thickness h = 0.635 mm and a relative dielectric constant ε_r = 6.15. Electromagnetic (EM) simulations and circuit simulations in this chapter are carried out by Zeland IE3D and Agilent ADS, respectively.

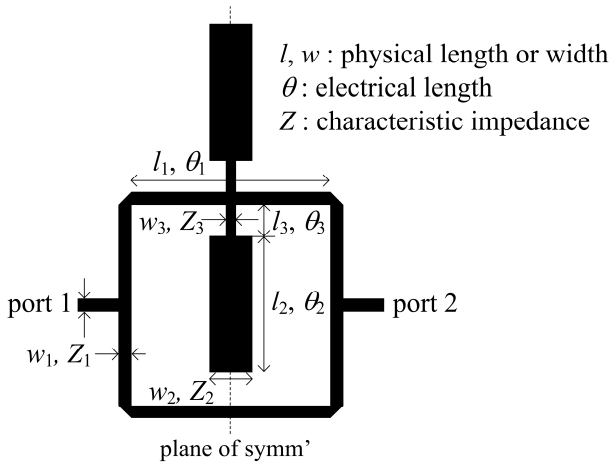

Fig. 1. Square ring resonator possessing two identical stepped-impedance stubs and direct-connected feed lines.

2. Ring resonator BPF design

A. Ring resonator with direct-connected feed lines

Fig. 1 shows the configuration of a square ring resonator possessing two identical stepped-impedance stubs fed by colinear direct-connected feed lines. These two open, stepped-impedance stubs have wide and narrow parts, which are placed on the symmetrical plane to perturb the ring resonator. In this figure, Z_1 is the characteristic impedance of both the feed lines and the square ring, while Z_2 and Z_3 are those of the stepped-impedance stub. The electrical length of one quarter of the ring is denoted by θ_1, while θ_2 and θ_3 are those of two sections of the open stubs. The physical lengths or widths are denoted by l or w in this figure, respectively. The reason for adding two identical open stubs is to make it easy to achieve more tunable states of the passband bandwidth. More explanations about three tunable states, achieved by taking advantage of four open stubs and PIN diodes, will be given in Section 3.

To calculate the resonant frequencies of this ring resonator, even- and odd-mode equivalent circuits are used [7]. The circuit in Fig. 1 can be divided using the symmetrical plane, one of which is regarded as an open circuit or a short circuit for even or odd modes, respectively. In the even mode, $2Z_2$ and $2Z_3$ result from dividing the stepped-impedance stubs in half along the plane of symmetry, as shown in Fig. 2(a). In the odd mode, because the plane of symmetry can be considered as ground plane, a simple equivalent circuit is made in Fig. 2(b). The resonance frequencies can be calculated when $Y_{in} = 0$ or $Z_{in} = 0$ from the one end of the even- and odd-mode circuit, respectively, which are expressed by

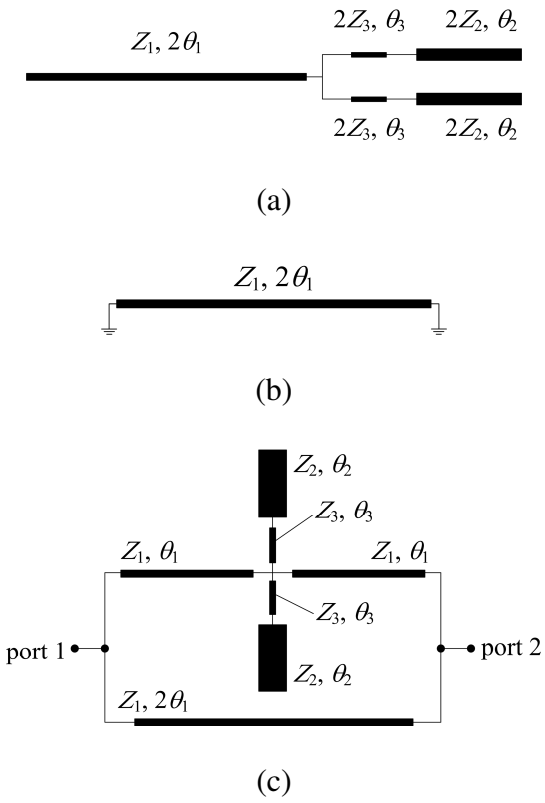

Fig. 2. Equivalent circuits of the ring resonator in Fig. 1. (a) Even mode. (b) Odd mode. (c) Circuit for obtaining transmission zero frequencies.

$$K' + K\cot\theta_2\tan\theta_3 + K'\tan 2\theta_1(K\cot\theta_2 - K'\tan\theta_3) = 0 \quad \text{for even modes} \quad (2)$$

and

$$\tan 2\theta_1 = 0 \quad \text{for odd modes} \quad (3)$$

where K and K' in (2) are defined as Z_2/Z_1 and Z_3/Z_1, respectively. The transmission zero frequencies are obtained when $Y_{21} = Y_{12} = 0$, where the admittance matrices are calculated by adding upper and lower Y-parameters of the two paths connected in shunt between port 1 and 2 in Fig. 1. The upper and lower Y-parameters are acquired through

the conversion of *ABCD*-parameters. Fig. 2(c) is used for obtaining these transmission zeros, and the calculated results are expressed by

$$\left\{\cos\theta_1 - \frac{\sin\theta_1}{K'}\frac{(K'+K\cot\theta_2\tan\theta_3)}{(K\cot\theta_2 - K'\tan\theta_3)}\right\}^{-1} + \sec\theta_1 = 0. \quad (4)$$

The electrical length of θ_1 in Fig. 1 is easily decided by using both the desired center frequency and the substrate's information [13], [14], so the physical length l_1 is chosen to be 14 mm for the center frequency of 2.5 GHz. 50-Ω transmission lines are used for Z_1. The remaining four variables such as θ_2, θ_3, Z_2, and Z_3 need to be determined by taking into account not only the characteristics of the BPF but also the tunability of the passband. These undecided values can be estimated by using the previous three conditions (2)-(4).

Fig. 3 plots the first two even-mode resonant frequencies (f_E) and the first two transmission zero frequencies (f_Z) normalized by the first odd-mode resonant frequency (f_{O1}) against θ_2/θ_1 under different values of K and K'. Figs. 3(a), (b), and (c) are for θ_3/θ_1 = 0.2/14, 2.2/14, and 4.2/14, respectively. For each figure in Fig. 3, K' is fixed at 1.15 for the left-hand figures, while K is fixed at 0.42 for the right-hand figures. If f_{O1} is considered as the desired center frequency, f_{E2} - f_{E1} at a certain θ_2/θ_1 can be considered approximately as the passband bandwidth. In every figure in Fig. 3, f_E and f_Z progressively move to lower frequencies as θ_2/θ_1 increases to 1. Moreover, the varying range of the bandwidth due to the variations of K or K' at a certain θ_2/θ_1 seems to become different as θ_2/θ_1 varies. At point *A* in the left-hand figure of Fig. 3(b), which indicates $\theta_2/\theta_1 = 9.5/14 \approx 0.68$, the mid-lower passband bandwidth (f_{O1} - f_{E1}) increases

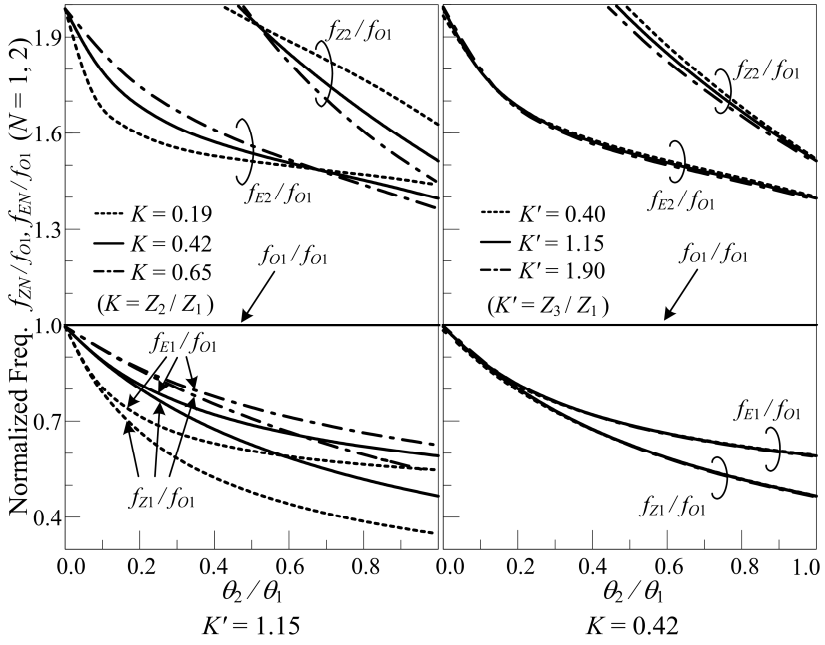

(a)

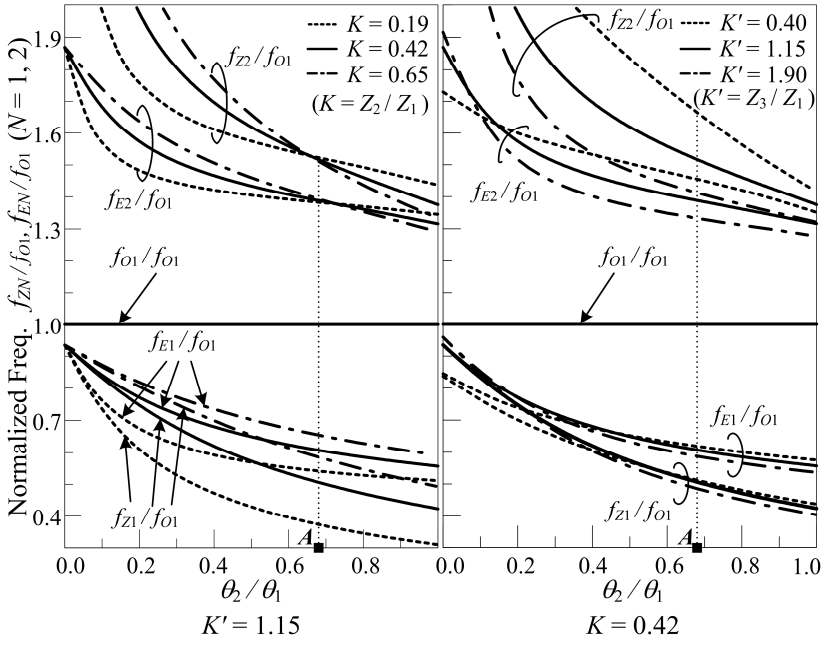

(b)

Fig. 3. Resonant frequencies (f_E: even-mode, f_O: odd-mode) and transmission zero frequencies (f_Z) normalized by f_{O1} for the resonator in Fig. 1. (a) $\theta_3/\theta_1 = 0.2/14$. (b) $\theta_3/\theta_1 = 2.2/14$. (c) $\theta_3/\theta_1 = 4.2/14$.

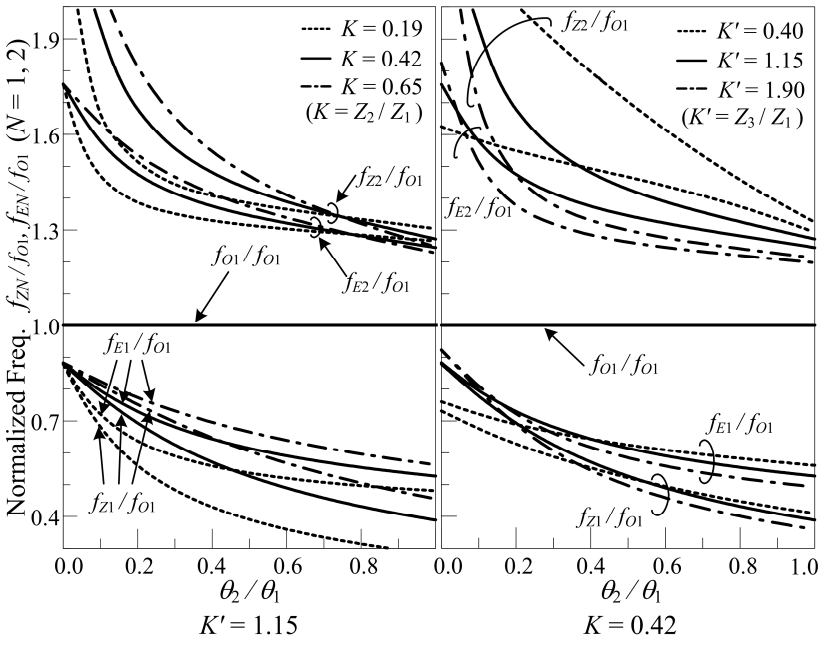

(c)

Fig. 3. Continued.

by using a smaller K while the mid-upper passband bandwidth (f_{E2} - f_{O1}) hardly changes. Besides, at the point A in the right-hand figure of Fig. 3(b), the mid-upper passband bandwidth increases by using a smaller K' with very small variations of the mid-lower passband bandwidth. These characteristics make it possible to design a BPF with the capability to control the mid-lower and mid-upper passband bandwidth separately. Therefore, $\theta_2/\theta_1 = 9.5/14$ and $\theta_3/\theta_1 = 2.2/14$ is tentatively chosen from the point A in Fig. 3(b). On the other hand, the right-hand figure of Fig. 3(a) shows that relatively low value of θ_3/θ_1 is not good for the tunability of the mid-upper passband because there are almost no bandwidth variations under different K's. In the left-hand figure of Fig. 3(c), even though the tuning of the mid-lower passband bandwidth is good at about $\theta_2/\theta_1 = 0.75$, the desired center frequency (f_{O1}) is not located at the center of the passband. In addition,

in the right-hand figure of Fig. 3(c), the mid-lower passband bandwidth varies considerably as well while the mid-upper passband is switched by changing K', which makes it difficult to design the BPF with the separate control on the upper or lower side of the passband.

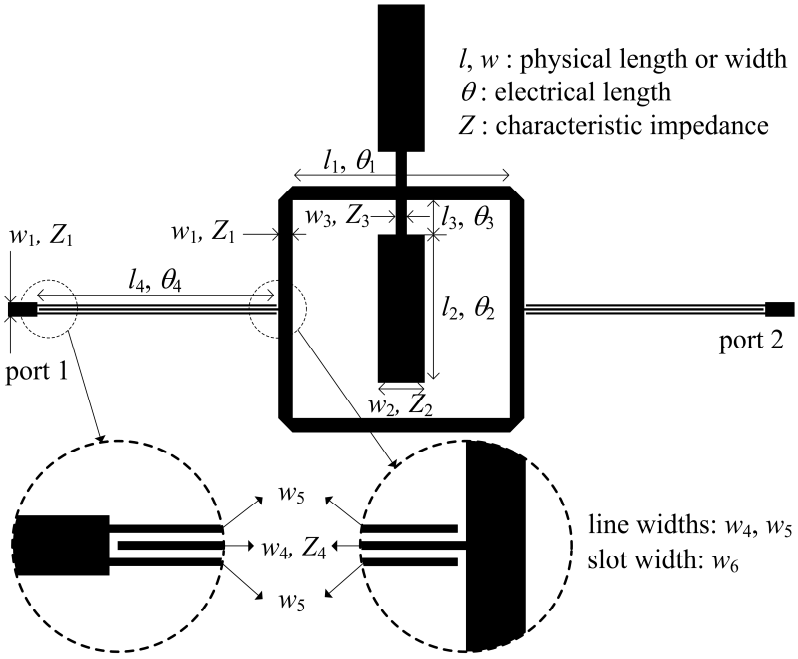

Fig. 4. Square ring resonator possessing two identical stepped-impedance stubs fed by interdigital-coupled feed lines.

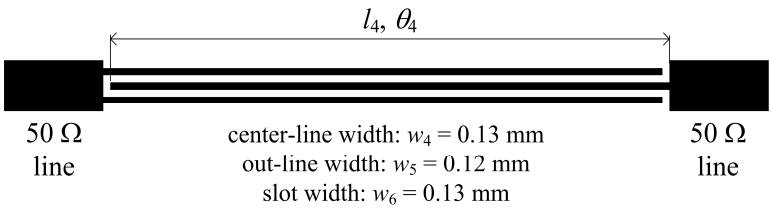

Fig. 5. Interdigital-coupled feed lines used in Fig. 4.

B. Characteristics of interdigital-coupled feed lines

Fig. 4 shows the ring BPF where the direct-connected feed lines shown in Fig. 1 are replaced by the interdigital-coupled feed lines while the same square ring is used. Z_4 and θ_4 are the characteristic impedance and the electrical length, respectively, of a center open stub forming the interdigital-coupled feed lines, which has the physical width w_4 and the physical length l_4 shown in Figs. 4 and 5. The physical line widths (w_4, w_5) and the slot width (w_6) for the interdigital-coupled feed lines are decided as shown in Fig. 5 by EM simulations to achieve a low loss and tight coupling between the ring resonator and the 50-Ω line ports. Specifically, w_4 = 0.13 mm corresponds to K'' = 2.12 where K'' is defined as Z_4/Z_1. To examine the characteristics of the interdigital-coupled lines, only the feed lines in Fig. 5 with three different lengths of l_4 are simulated.

These three kinds of simulated results are shown in Fig. 6, and, in the same figure, they are compared with the simulated result of the ring resonator fed by the direct-connected lines in Fig. 1. For the simulation of this ring with direct feed lines, the results of the previous section are used as follows: θ_2/θ_1 = 9.5/14, θ_3/θ_1 = 2.2/14, that is, l_1 = 14 mm, l_2 = 9.5 mm, l_3 = 2.2 mm. Also, the widths of the lines are selected with the characteristic impedances as follows: w_1 = 0.91 mm (Z_1 = 50 Ω), w_2 = 3.4 mm (K = 0.42), and w_3 = 0.7 mm (K' = 1.15). In Fig. 6, the transmission zeros of the interdigital-coupled lines are very close to the transmission poles of the ring resonator at about 0 and 5.5 GHz. The effect of these overlaps can be displayed when the ring and the interdigital-coupled lines are used together.

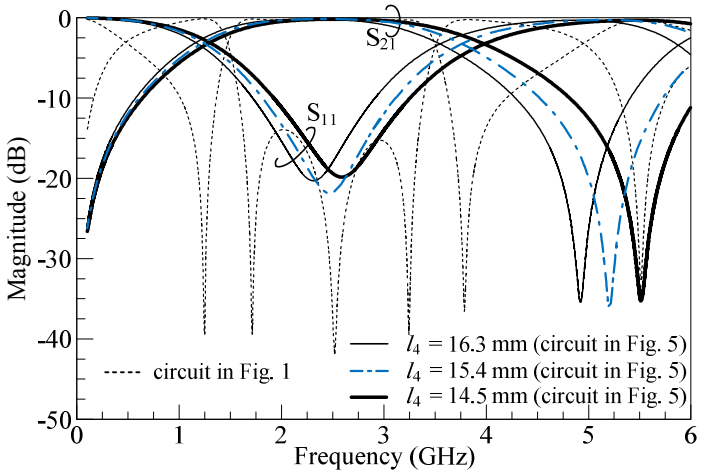

Fig. 6. Simulated results for both the interdigital-coupled feed lines in Fig. 5 using three kinds of l_4 and the ring resonator fed by direct-connected feed lines in Fig. 1.

Fig. 7 shows the simulated results of the ring fed by the interdigital-coupled lines shown in Figs. 4 and 5 with three different lengths of l_4. The dimensions of the ring and the two stepped-impedance stubs are the same as those of the ring with the direct feed lines used in the simulations of Fig. 6. The overlaps of zeros and poles shown in Fig. 6 result in harmonic suppression in Fig. 7, causing improved stopbands, sharper rejections at cutoff regions, and the wider passband in Fig. 7 compared to the result of the ring with direct feed lines in Fig. 6. l_4 is almost a quarter guide-wavelength at the center frequency of 2.5 GHz. If l_4 is longer than a quarter guide-wavelength, the center transmission pole of the five poles in Fig. 7 tends to move to lower frequencies, and then the return loss becomes worse in the mid-upper passband. Conversely, if l_4 is shorter than a quarter guide-wavelength, the center transmission pole tends to move to higher frequencies, and then the return loss becomes worse in the mid-lower passband. Among the results from

three values of l_4 in Fig. 7, 15.4 mm is chosen to obtain the better return loss and the lower insertion loss within the passband.

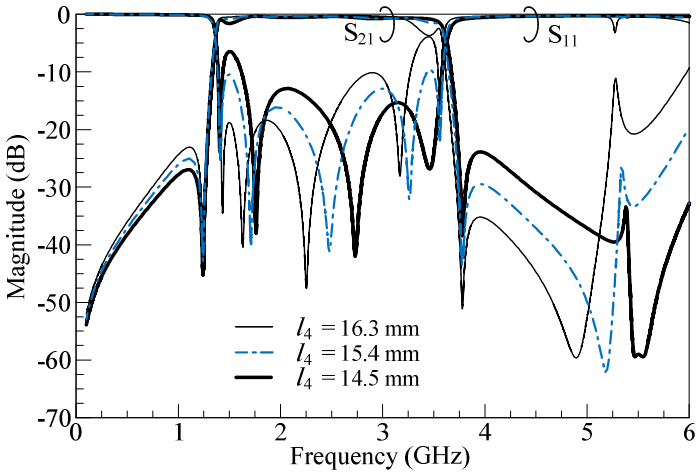

Fig. 7. Simulated results of the ring resonator fed by the interdigital-coupled feed lines in Fig. 4 with three kinds of l_4.

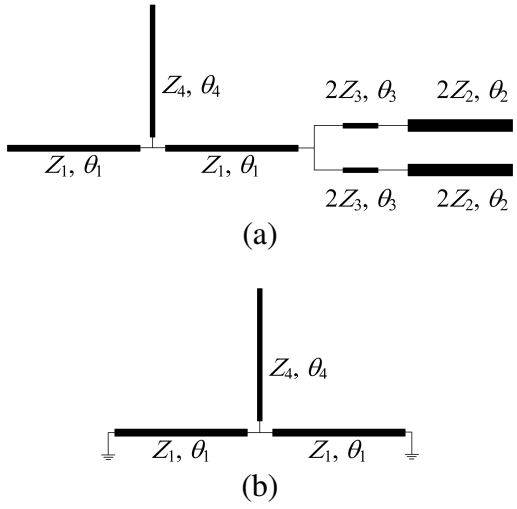

Fig. 8. Equivalent circuits of the ring resonator in Fig. 4. (a) Even-mode. (b) Odd-mode.

3. Reconfigurable BPF design

A. Design of BPF with discrete bandwidths

Even- and odd-mode equivalent circuits for the ring resonator fed by interdigital-coupled lines in Fig. 4 are shown in Figs. 8(a) and (b), respectively. Following the similar procedures in the previous section, the resonance conditions can be achieved and expressed by

$$\frac{M + K''^{-1}\tan\theta_4 + \tan\theta_1}{1 - \tan\theta_1(M + K''^{-1}\tan\theta_4)} = 0 \qquad \text{for even modes} \quad (5)$$

where

$$M = \frac{\left\{\dfrac{(K' + K\cot\theta_2\tan\theta_3)}{K'(K\cot\theta_2 - K'\tan\theta_3)} + \tan\theta_1\right\}}{\left\{1 - \dfrac{(K' + K\cot\theta_2\tan\theta_3)}{K'(K\cot\theta_2 - K'\tan\theta_3)}\tan\theta_1\right\}}$$

and

$$\frac{\tan\theta_1(\tan\theta_1 - 2K''\cot\theta_4)}{\tan\theta_1 + K''\cot\theta_4(\tan^2\theta_1 - 1)} = 0 \qquad \text{for odd modes.} \quad (6)$$

The transmission zeros for this ring fed by the interdigital-coupled lines are the same as those for the ring possessing direct-connected feed lines, which are expressed in (4), because transmission phases should be stationary along the two paths between port 1 and 2 [11].

Fig. 9 plots the first three even-mode resonant frequencies (f_E'), the first two odd-mode resonant frequencies (f_O') and the two transmission zeros (f_Z) normalized by the first odd-mode resonant frequency (f_{O1}) used in Fig. 3 against θ_2/θ_1 under different

values of K or K' when $\theta_3/\theta_1 = 2.2/14$, $\theta_4/\theta_1 = 15.4/14$, and $K'' = 2.12$. K' is fixed at 1.15 for the left-hand figure, while K is fixed at 0.42 for the right-hand figure of the Fig. 9. The values of f_{O1}' and f_{O2}' keep constant because the odd-mode equivalent circuit in Fig. 8(b) or the odd-mode resonant condition in (6) do not relate to θ_2, K, and K'. The values of f_{E2}' seem to vary quite slightly in the low level of θ_2/θ_1. The values of f_{Z1} and f_{Z2} are the same as those shown in Fig. 3(b), and the varying patterns of f_{E1}' and f_{E3}' are very similar to those of f_{E1} and f_{E2} in Fig. 3(b).

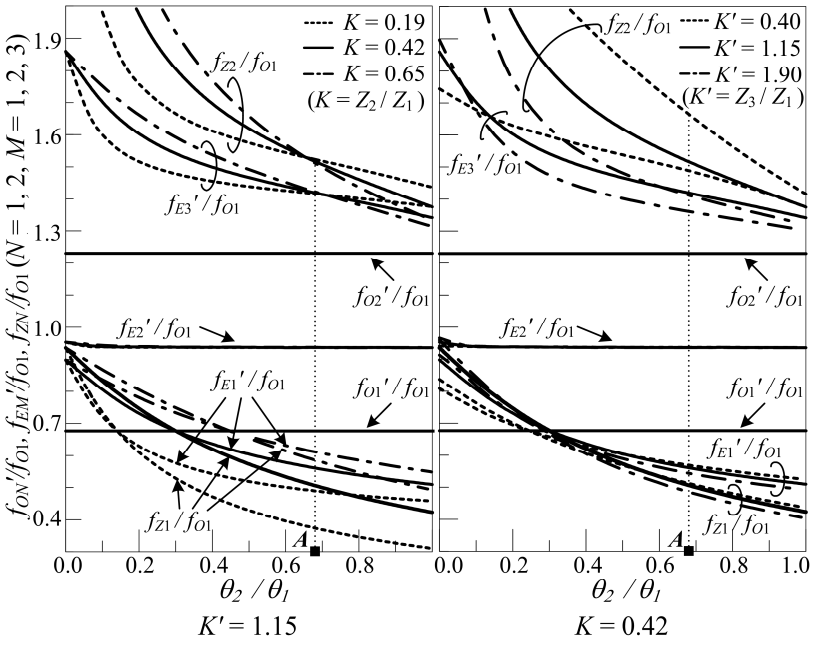

Fig. 9. Resonant frequencies (f_E': even-mode, f_O': odd-mode) and transmission zero frequencies (f_Z) normalized by f_{O1} for the ring resonator in Fig. 4 when $\theta_3/\theta_1 = 2.2/14$, $\theta_4/\theta_1 = 15.4/14$, and $K'' = 2.12$.

Owing to these similarities between Figs. 3(b) and 9, θ_2 and θ_3 of the ring fed by interdigital-coupled lines shown in Fig. 4 can be decided by just analyzing the ring with

direct feed lines shown in Fig. 1 to obtain the switching capability of the passband bandwidth. Consequently, the point *A* in Fig. 9 is chosen as the same point *A* shown in Fig. 3(b), which denotes θ_2/θ_1 = 9.5/14 when θ_3/θ_1 = 2.2/14, and the tunable characteristics is exhibited the same way as Fig. 3(b) shows. The left-hand figure of Fig. 9 shows that the mid-lower passband bandwidth (f_{O1} - f_{E1}') can be increased by using the lower *K* while the mid-upper passband bandwidth (f_{E3}' - f_{O1}) hardly changes at *A*. The right-hand figure of Fig. 9 also shows, at the same *A*, the mid-upper passband bandwidth can be increased by using the lower *K′* with very small variations of the mid-lower passband bandwidth.

Next, the mutual effect of *K* and *K′* on the passband bandwidth needs to be examined when θ_2/θ_1, θ_3/θ_1, θ_4/θ_1 and *K″* are fixed as the preceding values. Fig. 10 shows the five resonance frequencies and two transmission zeros when θ_2/θ_1 = 9.5/14, θ_3/θ_1 = 2.2/14, θ_4/θ_1 = 15.4/14, and *K″* = 2.12. Fig. 10(a) shows 7-frequency variations against *K* under three values of *K′* such as 0.4, 1.15, and 1.9, and Fig. 10(b) shows 7-frequency variations against *K′* under three values of *K* such as 0.19, 0.42, and 0.65. In Fig. 10(a), the mid-lower passband bandwidth decreases and the mid-upper passband bandwidth keeps almost constant as *K* increases for all three kinds of *K′*. In Fig. 10(b), the mid-upper passband bandwidth decreases and the mid-lower passband bandwidth increases very slightly as *K′* increases for all three kinds of *K*. From these results, it is verified that the mid-lower and the mid-upper passbands are mainly affected by *K* and *K′*, respectively, and they are not influenced a lot in reverse order when θ_2, θ_3, and feed lines, designed in the previous section, are used.

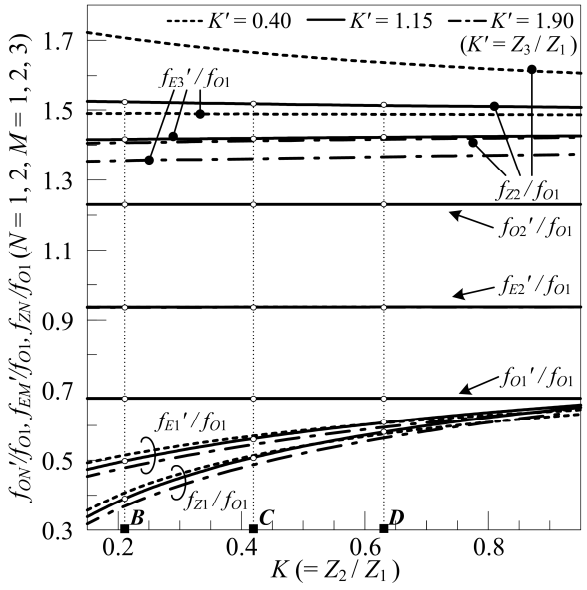

Fig. 10. Resonant and transmission zero frequencies normalized by f_{O1} for the ring resonator in Fig. 4 when $\theta_2/\theta_1 = 9.5/14$, $\theta_3/\theta_1 = 2.2/14$, $\theta_4/\theta_1 = 15.4/14$, and $K'' = 2.12$. (a) Frequency variations vs. K. (b) Frequency variations vs. K'.

For validating the separate tunings, BPFs are designed and fabricated by using the information in Fig. 10. When K' = 1.15, three kinds of K (0.21, 0.42 and 0.63

denoted by *B*, *C* and *D*) in Fig. 10(a) are chosen for checking the simulated and measured results, which are shown in Fig. 11. Similarly, when K = 0.42, three kinds of K' (0.66, 1.15 and 1.64 denoted by *E*, *F* and *G*) in Fig. 10(b) are selected, and the simulated and measured results are shown in Fig. 12. For these results, l_1 = 14 mm, w_1 =

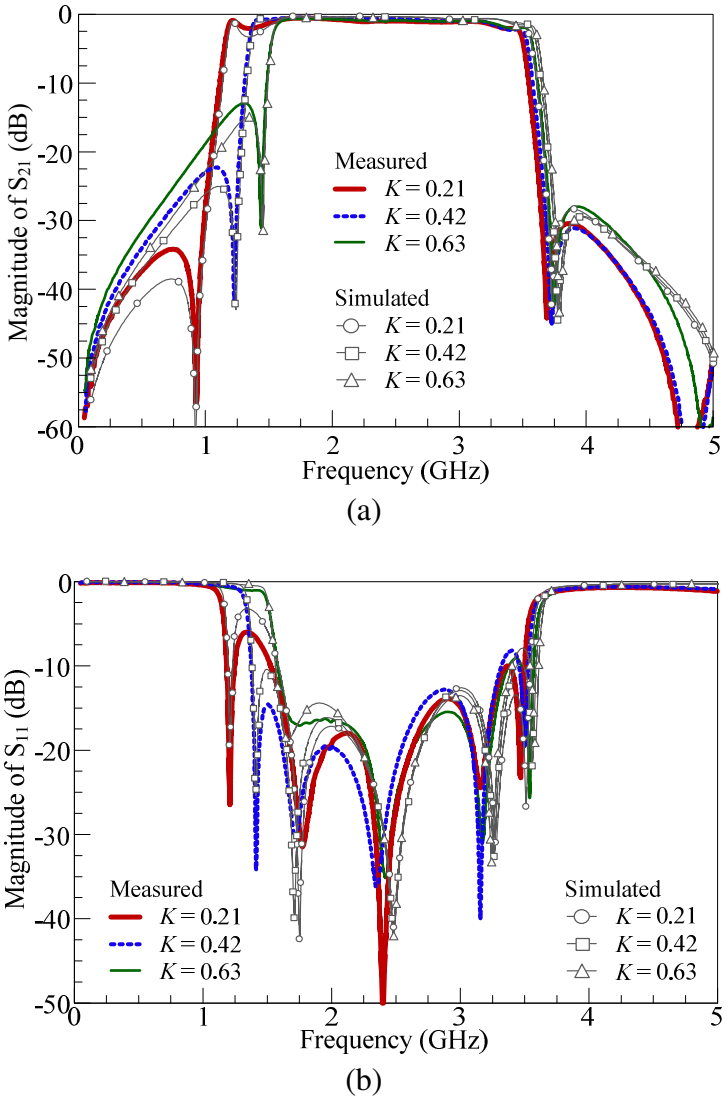

Fig. 11. Simulated and measured results for three *K*s (points *B*, *C*, and *D*) in Fig. 10(a) when K' = 1.15. (a) S_{21}. (b) S_{11}.

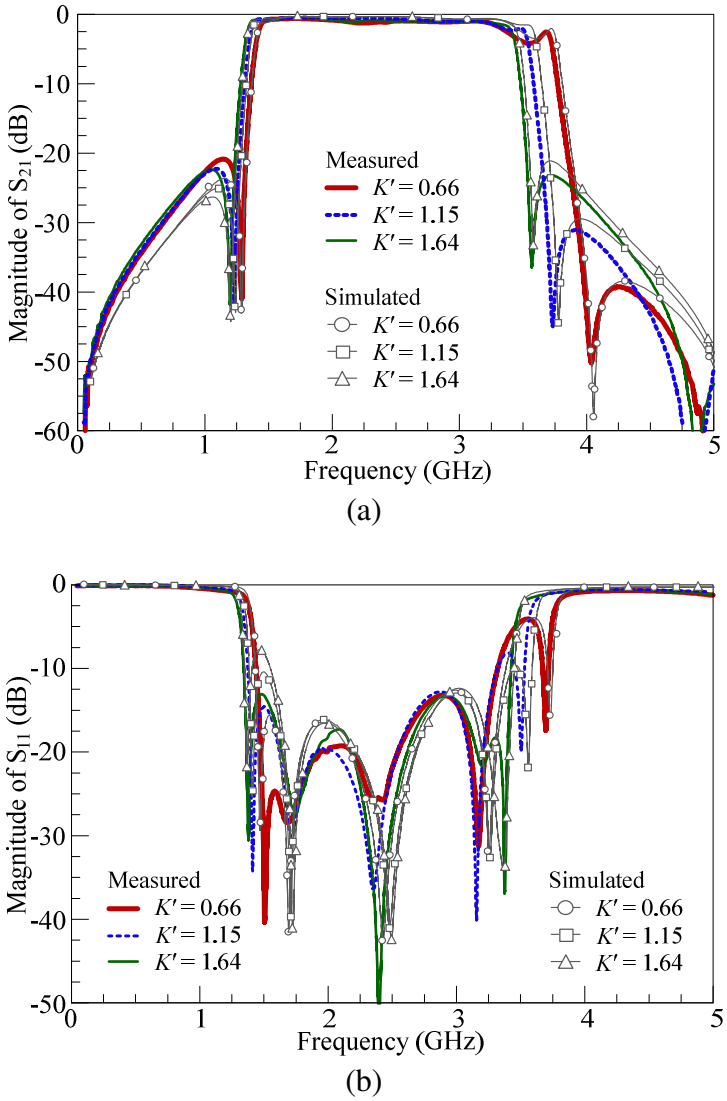

Fig. 12. Simulated and measured results for three K's (points E, F, and G) in Fig. 10(b) when $K = 0.42$. (a) S_{21}. (b) S_{11}.

0.91 mm, l_2 = 9.5 mm, l_3 = 2.2 mm and the feed lines in Fig. 5 with l_4 = 15.4 mm are used. In Fig. 11, w_2 is 7.77, 3.4, and 1.94 mm for K = 0.21, 0.42, and 0.63, respectively, while w_3 = 0.7 mm for K' = 1.15. For Fig. 12, w_3 is 1.8, 0.7, and 0.3 mm for K' = 0.66, 1.15, and 1.64, respectively, while w_2 = 3.4 mm for K = 0.42. As expected, Figs. 11 and 12 clearly show the bandwidth tunability by varying the values of K or K'. In other

words, Fig. 11 shows that the mid-lower passband bandwidth can be increased by increasing w_2, and Fig. 12 shows that the mid-upper passband bandwidth can be increased by increasing w_3.

Hence, after choosing appropriate θ_2, θ_3, θ_4, and K'' by utilizing the methods shown in the previous section, the mid-upper and the mid-lower passband bandwidth can be separately tunable by varying the characteristic impedances of the two sections of the stepped open stubs. However, both Figs. 11 and 12 also show the insertion losses become slightly higher and the return losses become slightly worse within the passband near the cutoff regions as the passband bandwidths are increased. Moreover, the center frequencies in both figures are not stationary because of the one-sided variation of the bandwidth.

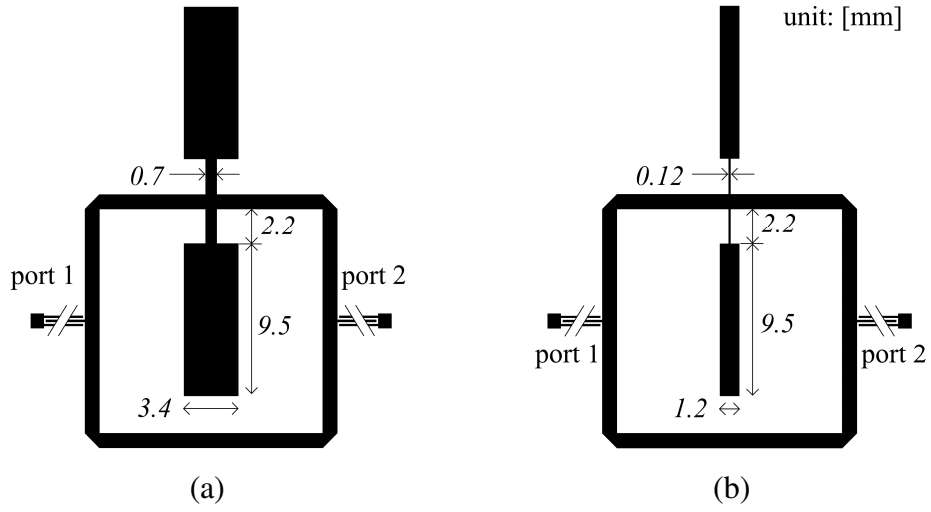

Fig. 13. Ring resonator with interdigital-coupled feed lines. (a) Wideband BPF when K = 0.42, K' = 1.15. (b) Narrowband BPF when K = 0.85, K' = 2.16.

B. Tunable passband with stationary center frequency

For switching the bandwidth with the stationary center frequency, w_2 and w_3 in Fig. 4 (or K and K') need to be changed simultaneously. For the wideband BPF to be realized, wide w_2 (low K) and wide w_3 (low K') are necessary for both the wide mid-lower and the wide mid-upper passbands, respectively. Conversely, for the narrowband BPF to be realized, narrow w_2 (high K) and narrow w_3 (high K') are necessary for both the narrow mid-lower and the narrow mid-upper passbands, respectively. For simulations and measurements of these two BPFs, all the dimensions are the same as those of the BPFs used in Figs. 11 and 12 except w_2 and w_3. As shown in Fig. 13, K = 0.42 (w_2 = 3.4 mm), K' = 1.15 (w_3 = 0.7 mm) are used for the wideband BPF in Fig. 13(a), and K = 0.85 (w_2 = 1.2 mm), K' = 2.16 (w_3 = 0.12 mm) are used for the narrowband BPF in Fig. 13(b). The measured and simulated results are shown in Fig. 14.

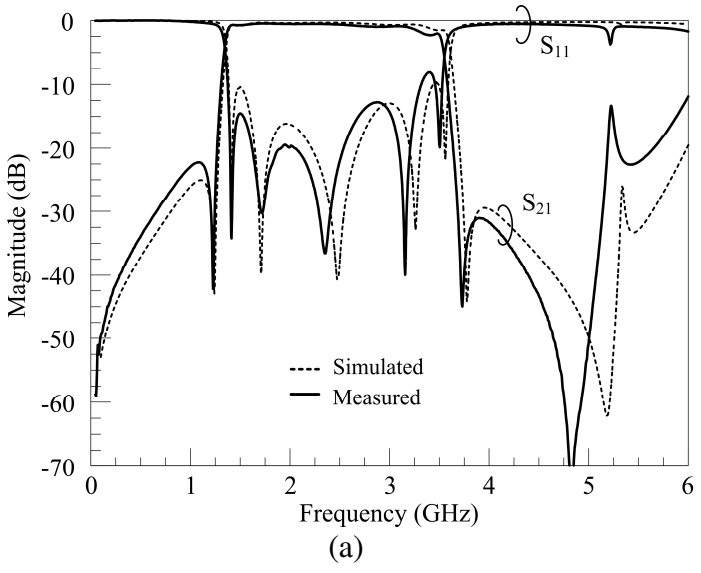

Fig. 14. Measured and simulated results of the filter in Fig. 13. (a) Wideband BPF. (b) Narrowband BPF.

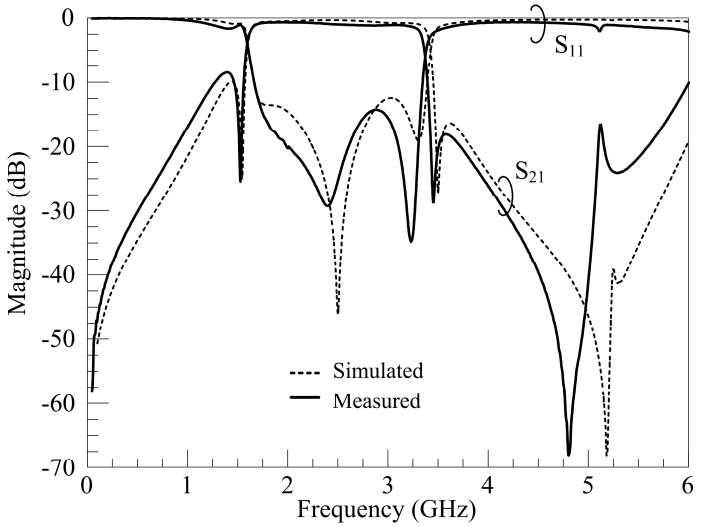

(b)

Fig. 14. Continued.

Table 1. Performance of the filter in Fig. 13.

Result	Wideband		Narrowband	
	Measured	Simulated	Measured	Simulated
3-dB FBW	89.3 %	90.3 %	70.4 %	71.3 %
Cent. freq.	2.44 GHz	2.48 GHz	2.47 GHz	2.51 GHz
Insert. loss	< 2.30 dB	< 1.54 dB	< 1.20 dB	< 0.79 dB
Return loss	> 8.15 dB	> 9.68 dB	> 14.26 dB	> 12.43 dB

To design the stepped-impedance stub of each filter, specifications for both the minimum return loss within the passband and the minimum insertion loss outside of the passband near the cutoff regions are set up as 10 dB. For the wideband response in Fig. 14(a), w_2 and w_3 are stretched to obtain the widest possible passband with the center frequency of 2.5 GHz. As w_2 or w_3 are increased, the return loss becomes worse within

the passband, and finally the loss reaches 10 dB. At this point, w_2 and w_3 have the maximum widths, and the passband has the maximum bandwidth. For the narrowband response in Fig. 14(b), w_2 and w_3 are decreased to obtain the narrowest possible passband with the same center frequency. w_2 can be decreased until the insertion loss at the lower stopband decreases to 10 dB. w_3 is also decreased until it meets the limit on fabrication. When these two limits are reached for w_2 and w_3, they have the minimum values, and the passband has the minimum bandwidth. Comparing S_{11} in Fig. 14(b) with that in Fig. 14(a), the simultaneous decreases of w_2 and w_3 give rise to the reduction of the number of resonances within the passband. Table 1 summarizes the performance of these filters in Fig. 13. Both the measured and the simulated results of the passband ratio are 1.27:1 with low losses while the center frequency barely moves.

C. Switchable bandwidth using PIN diodes

Fig. 15 shows the reconfigurable BPF using PIN diodes. To make three discrete states of the passbands, four open stepped-impedance stubs and two PIN diodes are used, where MACOM PIN diodes (MA4AGSBP907) are used in this experiment. It is worth mentioning here that the reason for introducing the ring with two identical stepped-impedance stubs rather than a single stub in Section 2 is to make it easy to realize three states of the passbands. Even if our full-wave simulations of the ring resonator with a single stepped-impedance stub show similar frequency responses to those in Fig. 7, it is difficult to attach additional two stubs near the original stub without changing the given values of θ_2/θ_1 and θ_3/θ_1. Also, the bias control scheme for two identical stubs is simpler

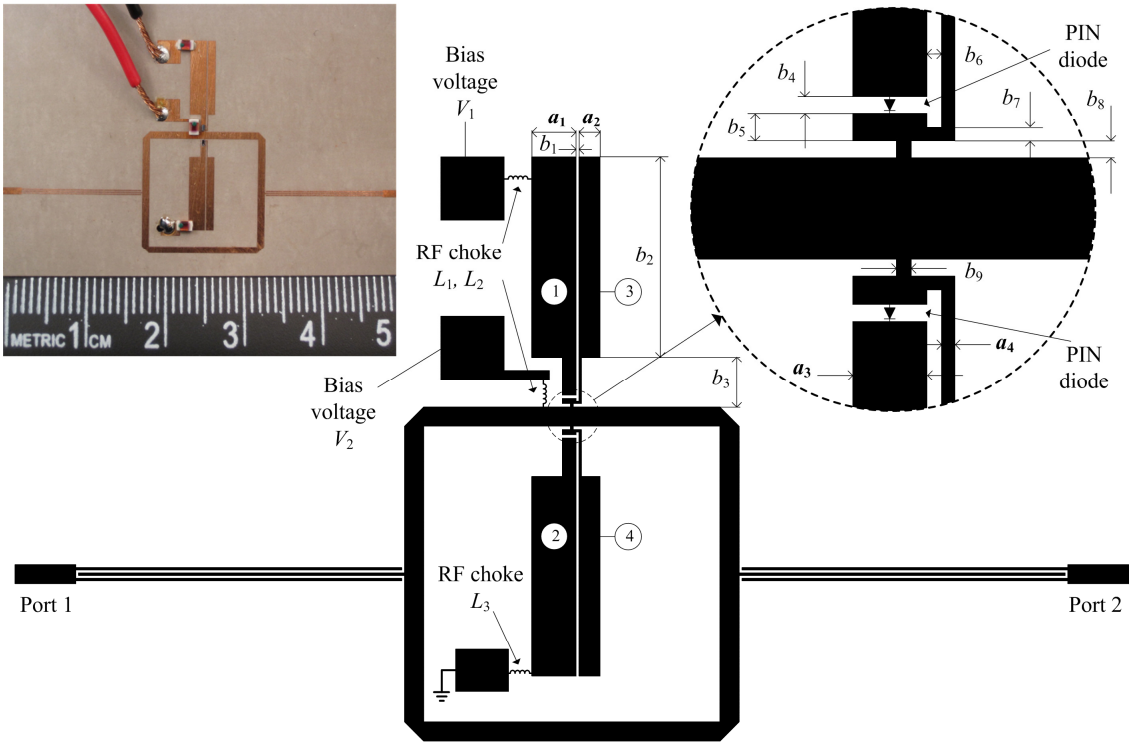

Fig. 15. The reconfigurable BPF with four stepped-impedance stubs using two PIN diodes. (a_1 = 2.1, a_2 = 1, a_3 = 0.66, a_4 = 0.12, b_1 = 0.13, b_2 = 9.5, b_3 = 2.35, b_4 = 0.15, b_5 = 0.25, b_6 = 0.13, b_7 = 0.12, b_8 = 0.15, b_9 = 0.13, all in millimeters.)

than that for a single stub. Three inductors L_1, L_2, and L_3 with 330 nH are used for RF chokes. In this experiment, the PIN diodes need to be located at the nearest feasible point to the ring between the open stub 1 or 2 and the ring to give the filter the effective switching capabilities. Allowing for mounting dimensions of the PIN diodes and a design of narrow microstrip necks with the width of b_9, which connect the ring with the four open stubs either inside or outside of the ring, proper positions of the PIN diodes are selected as shown in a dotted circle in Fig. 15. These two PIN diodes serve as switches between the ring and the open stubs 1 or 2. The open stubs 3 and 4 are attached to the

ring all the time without PIN diodes. The PIN diodes are turned on or off to connect or disconnect, respectively, the open stubs 1 or 2 with the ring.

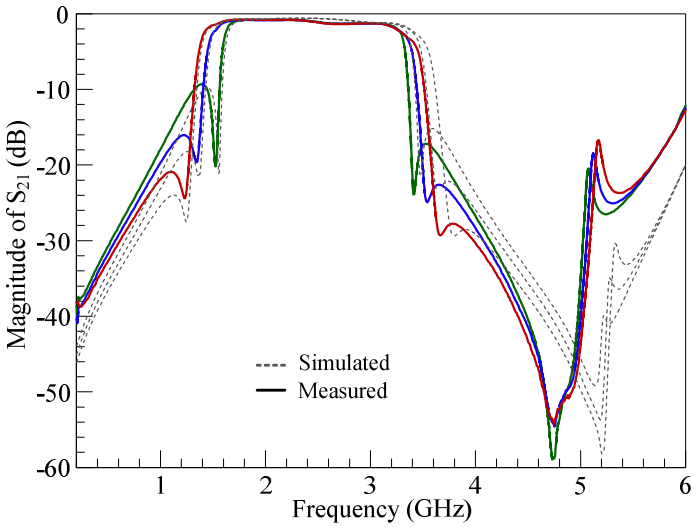

(a)

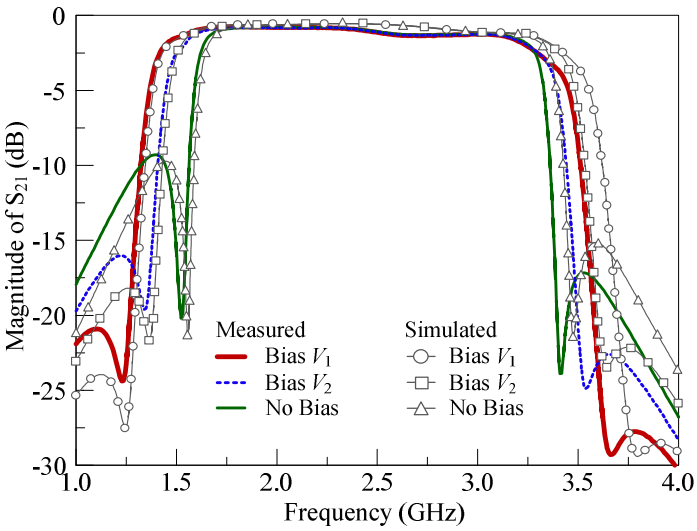

(b)

Fig. 16. Measured and simulated results of BPF with PIN diodes (Fig. 15) for S_{21}. (a) Entire-frequency range. (b) Zoom-in for switching capability.

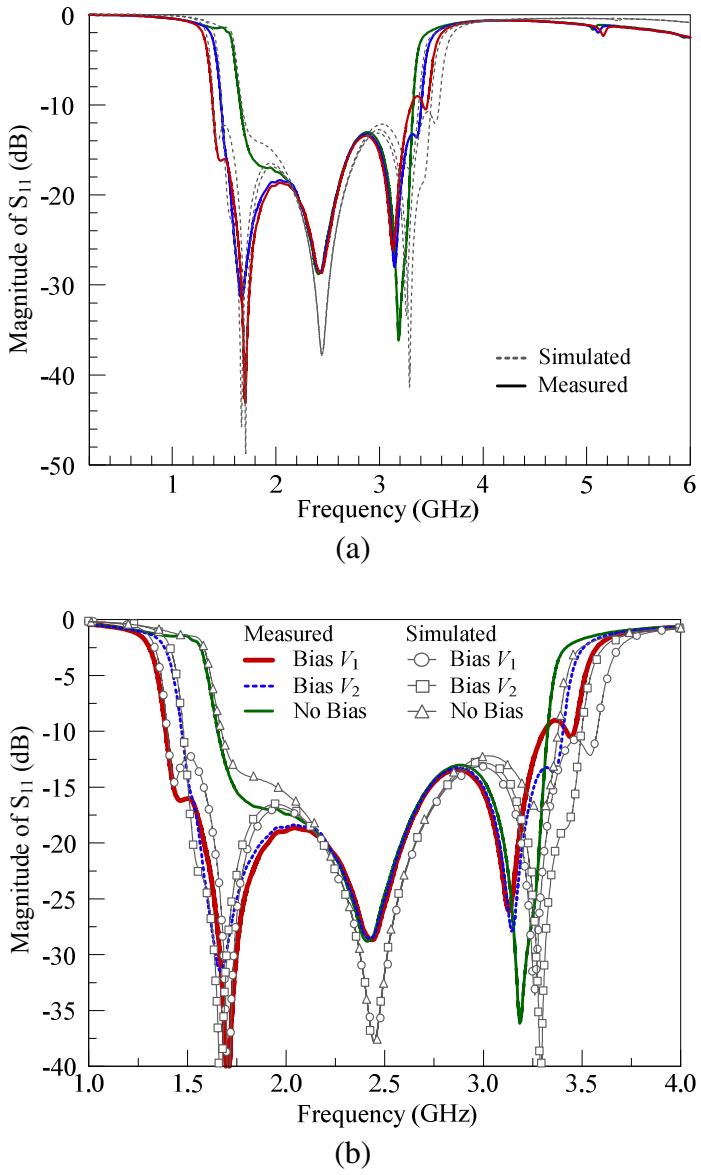

Fig. 17. Measured and simulated results of BPF with PIN diodes (Fig. 15) for S_{11}. (a) Entire-frequency range. (b) Zoom-in for switching capability.

Finally, the switching bandwidths are possible by controlling bias voltages V_1 or V_2, and the simulated and measured results of this filter are shown in Figs. 16 and 17. All the dimensions shown in Fig. 15 and the interdigital-coupled feed lines in Fig. 5 with l_4 = 15.4 mm are used. For the circuit simulations, the PIN diodes are replaced with 4-Ω

resistors or 25-fF capacitors for the on- or off-state of the PIN diodes, respectively. By adding the bias voltage only on V_1 with forward current of 10 mA, the two PIN diodes are turned on. Hence, the open stubs 1 and 2 become connected with the ring, resulting in the widest passband bandwidth in Fig. 16. If the bias voltage is added only on V_2, just one PIN diode located inside the square ring is turned on. Thus, the open stub 1 becomes disconnected and the open stub 2 gets connected with the ring, resulting in the medium passband bandwidth. When there is no bias voltage, the two PIN diodes are turned off. As a result, only two open stubs 3 and 4 remain connected to the ring, resulting in the narrowest passband bandwidth. Three states of the passbands are clearly presented in Figs. 16 and 17. Fig. 17 also shows that the number of resonances is increased or decreased as the bias conditions are changed.

The procedures of designing four stubs are very similar to those of designing two stubs in Fig. 13. All the dimensions are the same as those in Fig. 13 except the widths of the four stubs. Firstly, the simulations for deciding the widths of the stub 3 and 4 are tried without stub 1 and 2. a_2 in Fig. 15 can be decreased for obtaining the narrow mid-lower passband until the insertion loss at the lower stopband near the cutoff region decreases to about 10 dB. a_4 are also decreased for realizing the narrow mid-upper passband until it meets the limit of the fabrication. After the design of stubs 3 and 4 are completed, the widths of the stub 1 and 2 can be decided. While simulating the filter for deciding the widths of the stub 1 and 2, stub 3 and 4 are also simulated together for examining the wideband responses. a_1 and a_3 can be increased for obtaining the wide mid-lower and the wide mid-upper passband, respectively, until the return loss within

the passband decreases to about 10 dB. Table 2 shows the performance of this filter. The measured passband ratio for the three bandwidths is 1.22:1.13:1 with the maximum insertion loss of 1.35 dB. The center frequency is hardly moved as expected. The group delay obtained from the measured results varies between 0.62-2.17 ns, 0.62-2.27 ns, and 0.62-2.72 ns within the wide, mid, and narrow passband, respectively. The measured results agree very well with the simulated results.

Table 2. Performance of the filter in Fig. 15.

Result	Wideband		Mid-band		Narrowband	
	Meas.	Sim.	Meas.	Sim.	Meas.	Sim.
3-dB FBW	84.6 %	85.0 %	78.5 %	79.8 %	69.5 %	69.6 %
Center freq.	2.40 GHz	2.46 GHz	2.42 GHz	2.47 GHz	2.46 GHz	2.50 GHz
Insert. loss	< 1.35 dB	< 1.15 dB	< 1.33 dB	< 1.17 dB	< 1.30 dB	< 1.21 dB
Return loss	> 9.02 dB	> 10.79 dB	> 13.26 dB	> 12.81 dB	> 13.03 dB	> 12.20 dB

4. Conclusion

A novel wideband ring BPF with switchable passband bandwidth, using multiple stepped open stubs and interdigital-coupled feed lines, has been developed. The design on the lengths of each section of the stepped open stubs attached to the ring is made by analyzing the resonant and transmission zero frequencies obtained from the equivalent circuits. The ring with the interdigital-coupled feed lines adds two transmission zeros outside of the passband and achieves improved stopbands, a wider passband, and sharper

rejections compared to the ring with the direct-connected feed lines. After the optimization of the open stubs and the interdigital-coupled feed lines, the bandwidth becomes tunable on either the mid-upper or the mid-lower passbands by changing the characteristic impedances of each section of the stepped-impedance stubs. Wideband and narrowband BPFs are designed and fabricated by changing the number of resonances within the passband, resulting from the simultaneous increases or decreases of each width of the stepped open stubs. Four open stubs and two PIN diodes are used for switching three states of the passband, and the center frequency hardly moves during the tunings of the bandwidth. The passband switching ratio of the measured results is 1.22:1.13:1 with low losses and sharp rejections.

CHAPTER III

ULTRA-WIDEBAND (UWB) RING RESONATOR BANDPASS FILTER WITH A NOTCHED BAND*

1. Introduction

Since the approval of the unlicensed use of the ultra-wideband (UWB) spectrum from 3.1 GHz to 10.6 GHz in 2002 by the Federal Communications Commission (FCC), UWB technologies have received considerable attention from academic and industrial researchers [21]. Among the various UWB technologies, UWB bandpass filters (BPFs) are one of the most essential components in wireless communication systems operating in the UWB. Sharp selectivity and capabilities to avoid interference from existing radio signals are highly demanded to the UWB BPFs. Recently, there has been increasing research on the UWB BPF to satisfy these two essential requirements [22]-[25]. The notched bands have been realized in the UWB through various techniques, such as embedded stubs in transmission lines [22], out-of-phase transmission cancellation [23], meander-line slots [24], and short-circuited stub resonators in a multilayer periodical structure [25].

In this chapter, a ring resonator possessing two stepped-impedance stubs is used as a multiple-mode resonator [26] to develop UWB BPFs with and without a notched band. To obtain wider bandwidth than the results in Chapter II [27], the characteristic

---

impedance of the ring resonator is varied. Analyzing five resonance frequencies leads to the optimized design of the ring and stubs. Stepped-impedance ports are designed to achieve improved return losses at a high-frequency band, and asymmetric-port structures are developed to create a notched band at 5 GHz band. The proposed BPFs use an RT/Duroid 6006 substrate with a thickness of 0.635 mm and a relative dielectric constant of 6.15. Full-wave electromagnetic (EM) simulations in this chapter are carried out by Zeland IE3D.

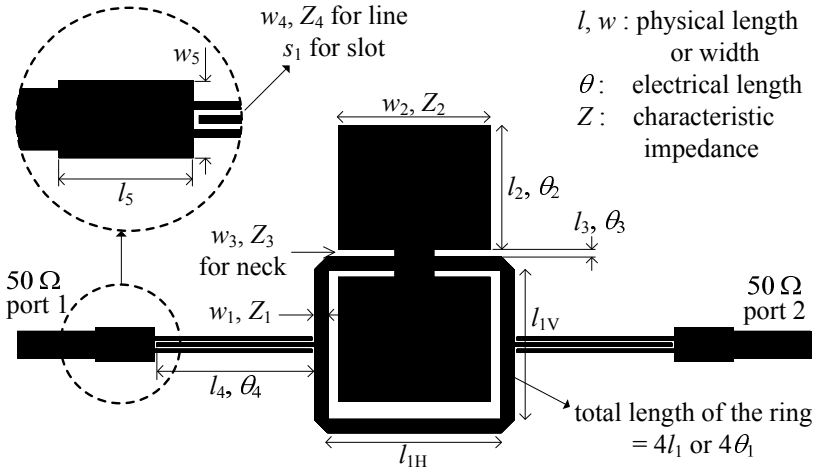

Fig. 18. Proposed UWB ring resonator BPF fed by interdigital-coupled lines possessing stepped-impedance ports. (l_{1H} = 5.92, l_{1V} = 5.12, l_2 = 4.25, l_3 = 0.25, l_4 = 5.39, l_5 = 2.0, w_1 = 0.46, w_2 = 5.2, w_3 = 1.3, w_4 = 0.11, w_5 = 1.15, s_1 = 0.10, all in millimeters.)

2. Design of UWB ring resonator BPF

Fig. 18 shows the configuration of a ring resonator possessing two stepped-impedance stubs fed by interdigital-coupled lines. The notation of a physical/electrical length, a physical width, and a characteristic impedance are the same as those in Chapter II. In addition, l_5 and w_5 denote dimensions of stepped-impedance ports. A quarter length

of the ring (l_1) is calculated to be 5.1, 5.3, and 5.5 mm for Z_1 = 30, 50, and 70 Ω, respectively, with the center frequency (f_O) of 6.8 GHz [13]. Then, after finding roots of the equations (4)-(6) in Chapter II, the approximate bandwidth can be estimated by investigating five resonant frequencies and two transmission zeros in Fig. 19. This figure plots the first three even-mode resonant frequencies (f_{E1}, f_{E2}, f_{E3}), the first two odd-mode resonant frequencies (f_{O1}, f_{O2}), and the two transmission zeros (f_{Z1}, f_{Z2}) normalized by the center frequency (f_O) against θ_2/θ_1 under three values of Z_1 when l_3 = 0.25 mm, l_4 = 5.39 mm, Z_3 = 41 Ω, and Z_4 = 111 Ω. Here, l_3 and Z_3 are decided by the similar procedures in [27]. The length of interdigital-coupled feed lines l_4 is chosen to be about a quarter wavelength at f_O to obtain wide upper and lower stopbands by achieving harmonic suppression [27], and Z_4 is decided by considering the limit on fabrication. Z_2 is fixed at 30 Ω and 15 Ω for the left- and right-hand figures in Fig. 19, respectively. When θ_2/θ_1 is a certain value larger than about 0.4, it is noticeable that each frequency is moving apart from f_O while Z_1 is increased from 30 to 70 Ω except f_{E2}. This shows that the wider bandwidth of the filter can be achieved when the narrower transmission line of the ring is used. Thus, 70 Ω for Z_1 and 5.5 mm for l_1 are chosen to realize the larger bandwidth. For deciding Z_2 and l_2, an approximate bandwidth, which is f_{E3} - f_{E1} at a certain value of θ_2/θ_1, needs to be calculated. By comparing the bandwidths at θ_2/θ_1 = 0.7, 0.8, and 0.9, denoted by *A* to *F* in Fig. 19, θ_2/θ_1 is optimized to realize the UWB bandwidth. The calculated bandwidths are 6.46, 6.39, 6.32, 7.07, 7.0, and 6.94 GHz for the points *A* to *F*. These results verify that lower Z_2 is more effective when Z_1 = 70 Ω. Consequently, the point *E* for l_2 and 15 Ω for Z_2 are chosen because the calculated passband at *E* is from

3.47 to 10.47 GHz, which is very close to the UWB passband. To reflect these calculated results on the design of the ring, the ring takes a shape of a rectangular as shown in Fig. 18.

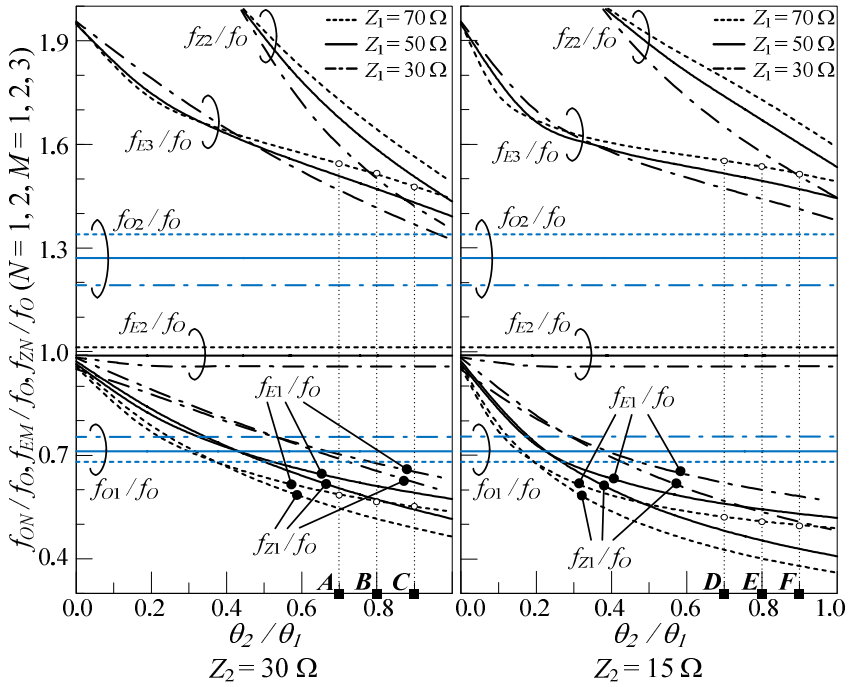

Fig. 19. Resonant frequencies (even-mode: f_{E1} - f_{E3}, odd-mode: f_{O1}, f_{O2}) and transmission zeros (f_{Z1}, f_{Z2}) normalized by the center frequency (f_O) when l_3 = 0.25 mm, l_4 = 5.39 mm, Z_3 = 41 Ω, and Z_4 = 111 Ω.

Fig. 20(a) shows the simulated results of the stepped-impedance port according to the variations of a step length l_5. As l_5 becomes longer from 0 to 4 mm, return losses vary within the passband when w_5 = 1.15 mm. During this continual process, the number of resonances is observed to change from 1 to 2. Fig. 20(b) shows the simulated results of the ring resonator with these stepped-impedance ports, using the dimensions shown in Fig. 18 with three kinds of l_5. Owing to the increased resonances from either stepped-

impedance ports, total number of resonances is observed to change from 5 to 7 while l_5 becomes longer from 0 to 4 mm. l_5 is optimized to be 2 mm because the return loss is improved in the high-frequency band.

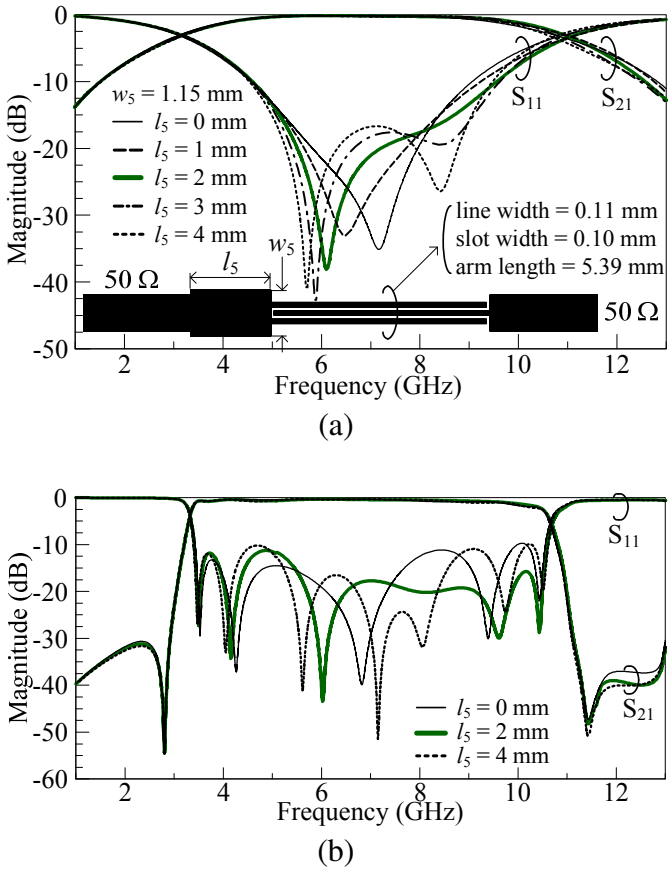

Fig. 20. Simulated results for variations of l_5 from (a) interdigital-coupled feed lines using a stepped-impedance port and (b) a ring resonator fed by the interdigital-coupled feed lines using stepped-impedance ports.

The fabricated filter is shown in Fig. 21(a), and measured and simulated results are compared in Fig. 21(b). For these results, l_3 is modified to 0.3 and 0.2 mm for the upper and lower neck, respectively, to eliminate a small notch observed in the measured

results at 5.0 GHz with a rejection level of 1.73 dB. Except l_3, the dimensions in Fig. 18 are used for Fig. 21. 3-dB FBWs are 103.3 and 103.7 % for measured and simulated results, respectively, which show increases of 15.7 and 14.8 % over the previous data in Table 1 from Chapter II. Moreover, the measured results show that the insertion loss at the center frequency of 6.73 GHz is 0.97 dB, the return loss within the passband is larger than 10.31 dB, and the variation of group delay over the passband is 0.33-1.15 ns.

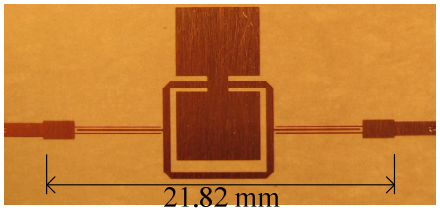

(a)

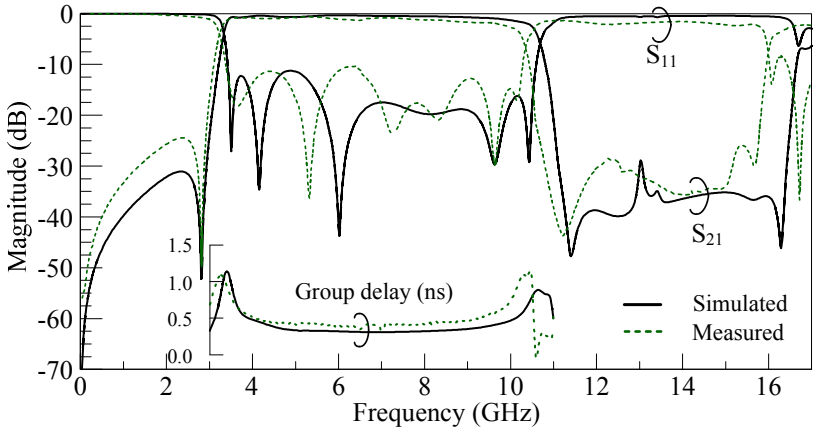

(b)

Fig. 21. (a) Fabricated UWB BPF. (b) Simulated and measured results.

3. UWB BPF with a notched band

To avoid the WLAN signals at 5 GHz band, a notched band is necessary within the passband of the UWB BPF. To create this notch-band, the stepped-impedance port in

Fig. 20(a) is modified to have an asymmetric structure as shown in Fig. 22(a). In this figure, the lengths of the two paths in the interdigital-coupled feed lines are different, resulting in out of phase of the signals on the two paths at a certain frequency. In Fig. 22(b) for l_6 = w_6 = 0 mm, as the slot length l_7 becomes longer from 0.5 to 2 mm, the notched bands are introduced at 6.67, 6.31, 6.01, and 5.68 GHz, consecutively, where low-rejection levels are observed.

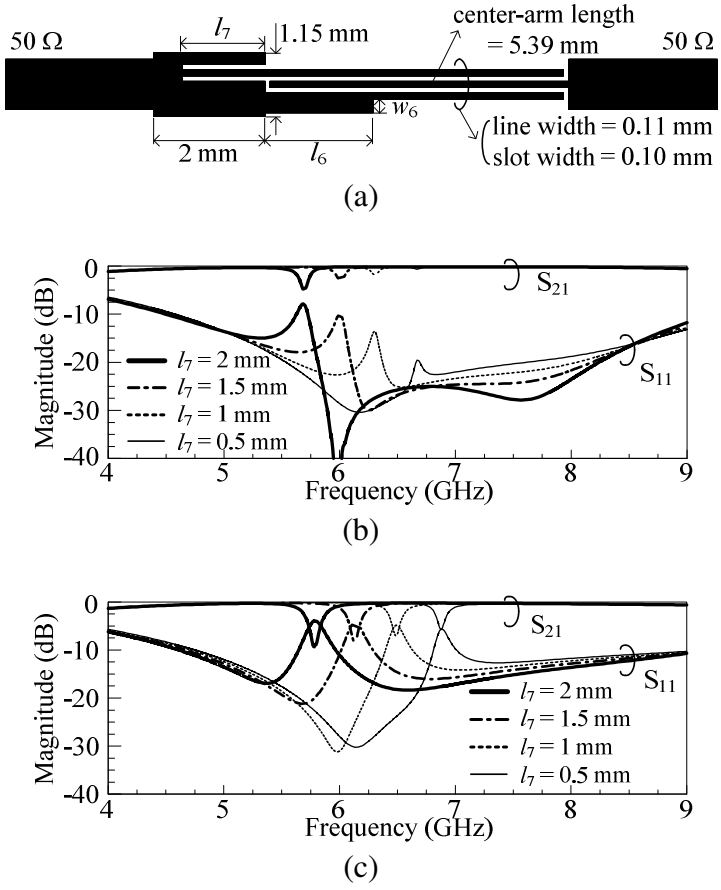

Fig. 22. (a) Interdigital-coupled feed lines with asymmetric structures embedded in the stepped-impedance port. Simulated results with varying l_7 when (b) l_6 = 0 mm, w_6 = 0 mm and (c) l_6 = 1.95 mm, w_6 = 0.25 mm.

To improve these rejection levels, the width of one signal path of the feed lines can be altered in part. By adding a stub with the size of l_6 (= 1.95 mm) × w_6 (= 0.25 mm) to only one path, the rejection levels become improved significantly in Fig. 22(c). Notching frequencies are at 6.88, 6.49, 6.13, and 5.77 GHz, and they are almost the same as those in Fig. 22(b). These results show that the length difference between the two signal paths of the coupled-feed lines controls the notching frequency and the characteristic-impedance difference affects the rejection level of the notched band.

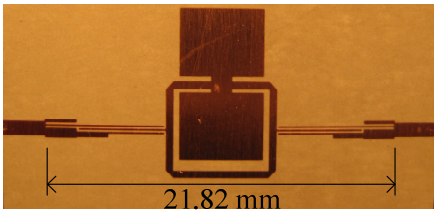

(a)

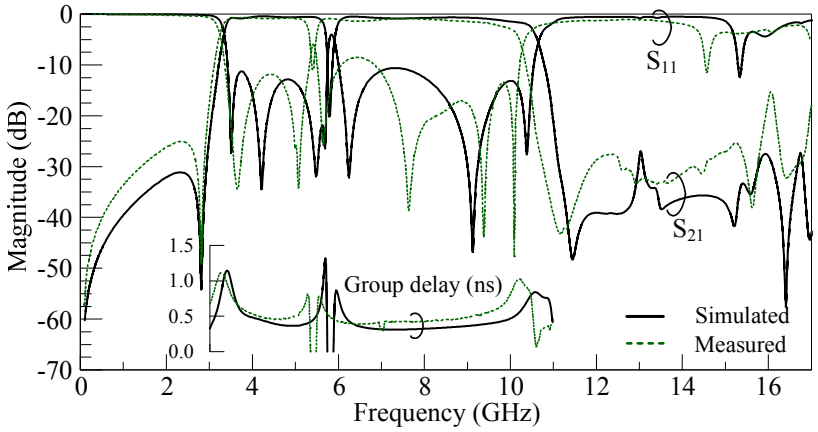

(b)

Fig. 23. (a) Fabricated UWB BPF with a notched band. (b) Simulated and measured results when l_6 = 1.95 mm, w_6 = 0.25 mm, and l_7 = 1.95 mm.

Fig. 23(a) shows the fabricated filter using the same dimensions used in Fig. 21 as well as the asymmetric structure in Fig. 22 with l_6 = 1.95 mm, w_6 = 0.25 mm, and l_7 = 1.95 mm. The measured and simulated results of this filter are shown in Fig. 23(b), where the measured notched band is observed at 5.41 GHz with the rejection level of 11.14 dB and the FBW of 3.5 %. The performance of this filter is summarized and compared with some previous work in Table 3.

Table 3. Comparison with previous work.

UWB BPF with a notched band		Fig. 23		Filter B in [22]	Fig. 13 in [25]
		Measured	Simulated		
FBW		102.8 %	103.3 %	110 %	91.1 % (10-dB)
Center frequency		6.69 GHz	6.95 GHz	6.85 GHz	7.15 GHz
Insertion loss over passband		1.33 dB at cent. freq.	0.75 dB at cent. freq.	<0.7 dB at cent. freq. of each band	N/A
Group delay		0.29-1.12 ns	0.31-1.32 ns	0.5 ns at cent. freq. of each band	< 0.68 ns at cent. freq. of each band
Notch band	Center freq.	5.41 GHz	5.79 GHz	5.83 GHz	6.05 GHz
	Reject. level	11.14 dB	20.20 dB	34 dB	32.64dB
	FBW	3.5 %	4.1 %	6.5 % (10-dB)	5.5 % (10-dB)

4. Conclusion

UWB ring resonator BPFs with and without a notched band have been developed by taking advantage of the wide bandwidth characteristics of the high characteristic-impedance ring resonator. Stepped-impedance ports are used to obtain better return losses in the high-frequency band, and asymmetric coupling structures are designed to

create the notched band at 5.41 GHz. The proposed filters also show promising features such as sharp rejections at both cutoff regions and low losses within the passband.

CHAPTER IV

INDEPENDENTLY CONTROLLABLE DUAL-BAND BANDPASS FILTERS USING ASYMMETRIC STEPPED-IMPEDANCE RESONATORS*

1. Introduction

The bandpass filters (BPFs) have become more attractive and essential components in modern wireless communication systems since a variety of services, such as global positioning system (GPS), Bluetooth, and wireless local area network (WLAN), have been provided. Due to the variously emerging service spectrum, the typical functions of the BPFs, such as an exact selection of wanted signals as well as a sharp stopband rejection, become more critical to prevent the interferences between the services. Moreover, capabilities of accessing dual- or tri-band frequencies are needed not only to minimize the size of the system by reducing the number of RF components, but also to provide effective multi-functional services. These filters with the abilities of supporting multi-band services have been intensively researched [28]-[35]. To design multiple-band resonators, some filters have used the characteristics of stepped-impedance resonators (SIRs) [28]-[31]. Design graphs for selecting desired fractional bandwidths (FBWs) have been provided [28], and a pair of transmission zeros near each passband resulting from cross coupling effects has improved the selectivity [29]. L-shaped SIRs with coupled-fed structures [30], multistub loaded resonators [31], crossed

resonators with short stubs [32], and dual-mode ring resonators [33] have been used for realizing multiple bands. A frequency transformation technique for finding transmission poles and zeros [34] and an individual feed scheme for lower and upper bands [35] have also been presented to realize dual-bands.

Furthermore, much attention has been given to electrical tunability as one of the diverse features of BPFs [36]-[39]. A tunable upper passband has been realized by using controllable even-mode resonant frequencies [36], and harmonic-suppressed tunable filters with two transmission zeros have been presented [37]. Switchable BPFs using a PIN diode have also exhibited two states and a wide stopband [38], and an analytic design procedure for tunable filters using SIRs loaded with varactors has been described [39].

In this chapter, independently switchable dual-band filters are developed. The asymmetric SIRs are designed for WLAN communication services operating in 2.4/5.2-GHz bands. Several design graphs are used to determine appropriate geometric parameters and transmission zeros. By taking advantage of the properties of extended feed lines, the second resonance of 2.4-GHz resonators is suppressed. Two sets of dual-band BPFs are designed by utilizing hook-type and spiral-type feed lines, and the latter is used for realizing switchable dual-bands with due regard to the effects of via-holes and better loss responses. Four switchable states are exhibited as a result of controlling PIN diodes inserted in the dual-band circuit. The proposed dual-band BPFs in this chapter use an RT/Duroid 6006 substrate with a thickness of 0.635 mm and a relative

dielectric constant of 6.15. Electromagnetic (EM) simulations and circuit simulations in this chapter are carried out by Zeland IE3D.

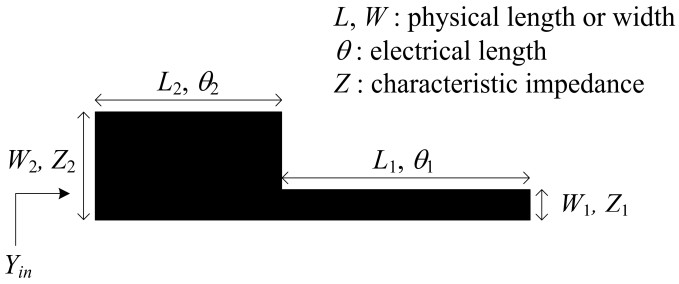

Fig. 24. Structure of an asymmetric SIR.

2. Resonances of asymmetric SIRs

An asymmetric SIR shown in Fig. 24 consists of narrow and wide sections with characteristic impedances Z_1 and Z_2. The physical lengths L_1 and L_2, physical widths W_1 and W_2, and electrical lengths θ_1 and θ_2 are shown for the two sections with Z_1 and Z_2, respectively. The characteristic impedance ratio K and the length ratio u are defined as follows:

$$K = \frac{Z_2}{Z_1} \tag{7}$$

and

$$u = \frac{\theta_2}{\theta_1 + \theta_2}. \tag{8}$$

The resonant frequencies can be calculated when $Y_{\text{in}} = 0$, as shown in Fig. 24, which are expressed by

$$\frac{K\tan\theta_1+\tan\theta_2}{1-K\tan\theta_1\tan\theta_2}=0. \tag{9}$$

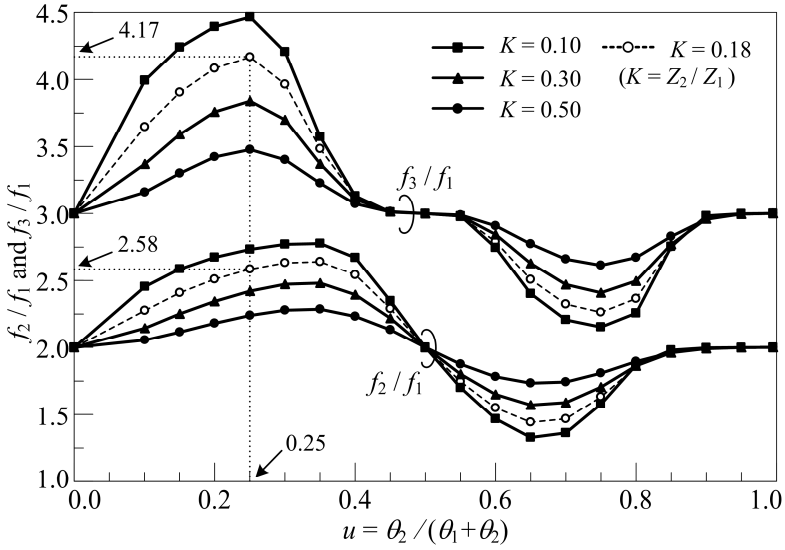

Fig. 25. f_2 (the second resonant frequency) and f_3 (the third one) normalized by f_1 (the first one) for the asymmetric SIR in Fig. 24.

By using the solution to (9), Fig. 25 plots the second and third resonant frequencies, f_2 and f_3, respectively, normalized by the first one (f_1) against u under different values of K. In this figure, when θ_1 and θ_2 are equal to each other, f_2 / f_1 and f_3 / f_1 are observed to be 2 and 3, respectively, since the first three solutions to (9) are calculated as $\theta_1 = \theta_2 = 0.5\pi$, π, 1.5π regardless of K. By suppressing f_2, a large upper rejection band can be obtained. In addition, the larger is f_3 / f_1, the wider is the upper rejection band when the suppression of f_2 is assumed. In order to make $f_3 / f_1 > 4$, we choose 0.25 for u when K = 0.18, resulting in $f_3 / f_1 = 4.17$, as shown in Fig. 25. Also, for these values of u and K, the first solution to θ_1 is calculated to be 1.823 by (9). That is, $L_1 = 1.823\lambda_g / 2\pi$, and

$$f_1 = \frac{c}{\lambda_g \sqrt{\varepsilon_{eff}}} = \frac{1.823 \cdot c}{L_1 \cdot 2\pi \sqrt{\varepsilon_{eff}}} \tag{10}$$

where c is the speed of light, λ_g is the guided wavelength and ε_{eff} is the effective dielectric constant of the microstrip. To aim f_1 at 2.4 GHz by using (10), ε_{eff} and L_1 need to be decided. Of these two variables, ε_{eff} can be fixed when W_1 is assumed to be 0.2 mm for the fabrication limit. L_1 is then the only variable left, which is decided to be 17.1 mm. Now that L_1 and W_1 are fixed, L_2 and W_2 can be fixed under the condition of u = 0.25 and K = 0.18. As a result, the dimensions of the 2.4-GHz resonator are L_1 = 17.1 mm, W_1 = 0.2 mm, L_2 = 5.6 mm and W_2 = 4.5 mm. Moreover, f_2 and f_3 of the 2.4-GHz resonator can be estimated to be 6.19 and 10.01GHz because f_2 / f_1 = 2.58 and f_3 / f_1 = 4.17 as shown in Fig. 25.

3. BPFs using hook-type feed lines

To achieve independently controllable dual-band BPFs, signals from the source need to be divided and sent through 2.4- and 5.2-GHz resonators separately. In Fig. 26, signals passing through lower or upper paths make 2.4- or 5.2-GHz resonances, respectively, where solid circles with numbers 1 and 2 denote 2.4-GHz resonators, and those with numbers 3 and 4 denote 5.2-GHz resonators. By controlling PIN diodes, bypassing the signals that pass through upper or lower paths into the ground plane, the dual bands can be controlled independently. More explanations about the switchable dual bands will be given in Section 5. The denotations in Fig. 26 are for the BPF using hook-type feed lines, and another type of feed lines will be described in Section 4. In this

figure, $Q_{ex1,\,in}$ and $Q_{ex1,\,out}$ are the external quality factors at the input and output ports for 2.4-GHz resonators, respectively, and $Q_{ex2,\,in}$ and $Q_{ex2,\,out}$ are those for 5.2-GHz resonators. M_{12} and M_{34} are the coupling coefficients for 2.4- and 5.2-GHz resonators, respectively.

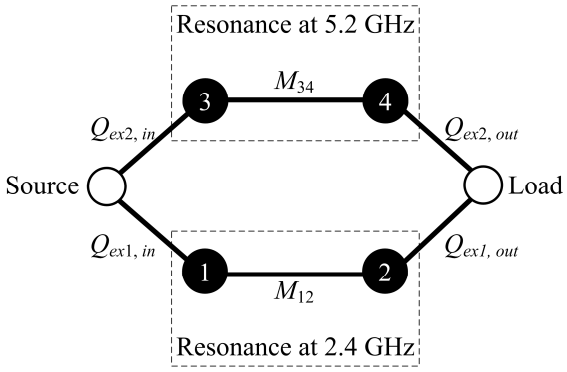

Fig. 26. Coupling structure of BPFs using hook-type feed lines. Solid circles with numbers 1 or 2 denote 2.4-GHz resonators, and those with numbers 3 or 4 denote 5.2-GHz resonators. M denotes the coupling coefficient, and Q_{ex} denotes the external quality factor.

A. 2.4-GHz BPF using hook-type feed lines

A two-pole (n = 2) Butterworth BPF with the FBW of 8.6 % is designed for 2.4-GHz filters. The lowpass prototype element values are $g_0 = g_3 = 1$ and $g_1 = g_2 = 1.4142$. The coupling coefficients and external quality factors of this filter can be calculated by [40]

$$M_{12} = \frac{FBW}{\sqrt{g_1 g_2}} = 0.061 \tag{11}$$

$$Q_{ex1,in} = Q_{ex1,out} = Q_{ex1} = \frac{g_0 g_1}{FBW} = 16.4 \tag{12}$$

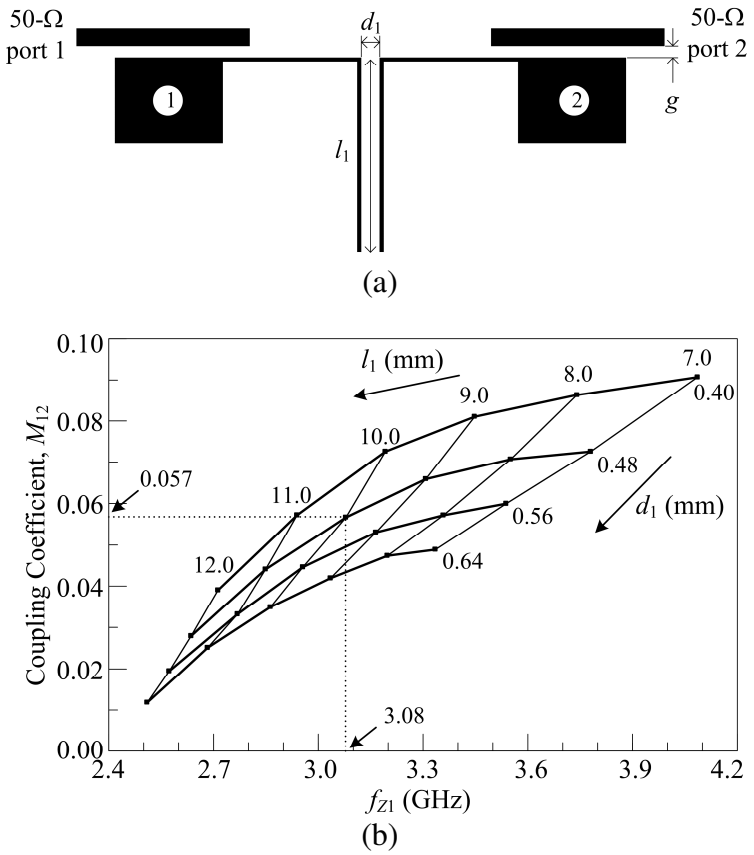

Fig. 27. Analysis of a coupling coefficient M_{12}. (a) Arrangement for EM simulation. (b) Design graph for resonators 1 and 2.

where Q_{ex1} is the external quality factor at the input or output ports for resonators 1 or 2. According to M_{12}, two design parameters in Fig. 27(a), such as d_1, a gap between the resonators 1 and 2, and l_1, a coupling length of the two resonators, can be decided, and an arrangement for EM simulations is shown in the figure. In addition to these two variables, a gap g between the resonators and 50-Ω ports is needed to extract the precise transmission zero created by the coupled section with the length of l_1. The transmission zero f_{Z1} is found to be expressed as [41], [42]

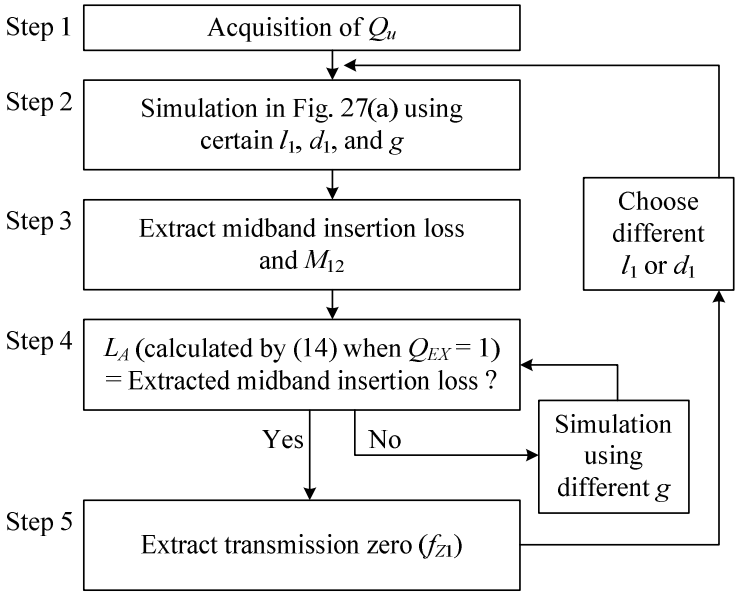

Fig. 28. Flowchart for extracting transmission zeros while obtaining M_{12}.

$$f_{Z1} = nf_1 \frac{90^\circ}{l_1 \cdot (360^\circ / \lambda_g)} = nf_1 \frac{\lambda_g}{4 \cdot l_1}, \qquad n = 1, 2, ... \tag{13}$$

where λ_g is the guided wavelength at f_1 (= 2.4 GHz). Using (13), l_1 can be approximately estimated to be 12.7 mm for having f_{Z1} located at 3 GHz. However, it is necessary to investigate the relation between the two parameters (l_1, d_1) and f_{Z1} in order to decide the transmission zero more precisely. For this purpose, the external quality factors Q_{EX} of the resonators 1 and 2 at the 50-Ω ports in Fig. 27(a) need to be fixed for all the simulations fulfilled by varying l_1 and d_1. In addition, a midband insertion loss L_A can be calculated by [43], [44]

$$L_A = 20 \log \left[\frac{\left(1 + Q_{EX} / Q_u\right)^2}{2 M_{12} Q_{EX}} + \frac{M_{12} Q_{EX}}{2} \right] \text{dB} \tag{14}$$

where Q_u is the unloaded quality factor of one of the resonators in Fig. 27(a). The following is the steps to extract f_{Z1} through a flowchart in Fig. 28. Firstly, Q_u is obtained for the resonator 1 or 2 (Q_u = 142) [43]. Secondly, a simulation is done with certain values of l_1, d_1, and g. Thirdly, based on the simulation results, a midband insertion loss and M_{12} can be extracted. M_{12} can be obtained by [40]

$$M_{12} = \frac{{f_{p2}}^2 - {f_{p1}}^2}{{f_{p2}}^2 + {f_{p1}}^2} \tag{15}$$

where f_{p1} and f_{p2} are two split resonant frequencies near the resonant frequency. Fourthly, L_A can be calculated by substituting the obtained values of Q_u, M_{12}, and Q_{EX} into (14), where Q_{EX} is designated to be 1. Then, this calculated value of L_A is compared with the extracted midband insertion loss obtained from the previous step. If they are different from each other, another simulation is carried out by using different g until they become all much the same. Finally, when this comparison results in coincidence, transmission zero f_{Z1} can be extracted. For another pair of l_1 and d_1, the flowchart can be repeated from Step 2 in Fig. 28. It is noteworthy that Q_u barely changes its value even if l_1 varies with a fixed L_1 (= 17.1 mm), without regard to d_1, so an arrow leads to the point between Step 1 and 2 after choosing different l_1 or d_1. M_{12} also keeps almost the same value even though g varies for certain values of l_1 and d_1. Thus, another arrow leads directly to Step 4 after adjusting g. The results of this flowchart are plotted in the design graph of Fig. 27(b), which shows M_{12} against f_{Z1} under different values of l_1 and d_1. In this figure, considering a sharp rejection at an upper cutoff region and the given value of M_{12} in (11),

geometric parameters in Fig. 27(a) are chosen as l_1 = 10.0 mm, d_1 = 0.48 mm while M_{12} = 0.057, f_{Z1} = 3.08 GHz.

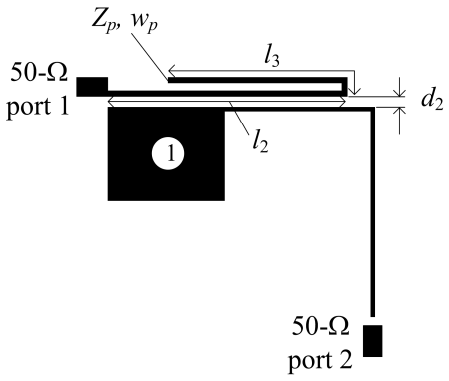

(a)

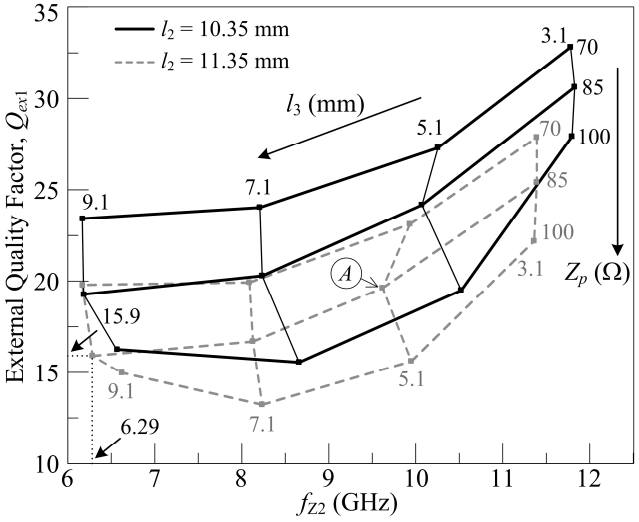

(b)

Fig. 29. Analysis of an external quality factor Q_{ex1}. (a) Arrangement for EM simulation. (b) Design graph for a hook-type feed line when d_2 = 0.18 mm. (c) Design graph for a hook-type feed line when l_3 = 9.1 mm.

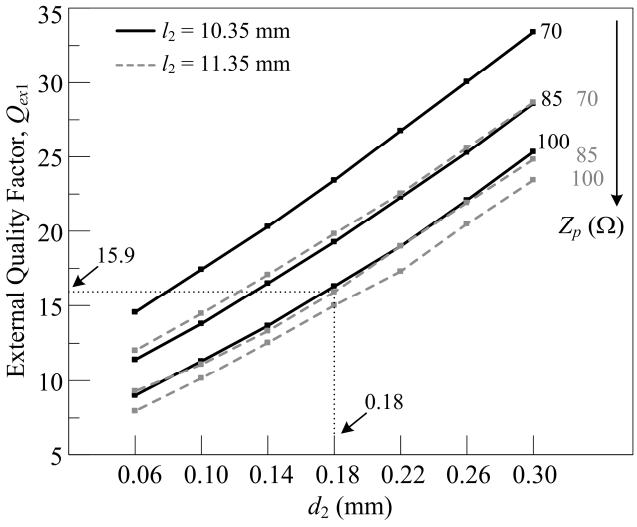

(c)

Fig. 29. Continued.

According to Q_{ex1} in (12), a hook-type feed line can be designed. Fig. 29(a) shows an arrangement for EM simulations, where a coupled-section length l_2, a gap d_2 between the feed line and the resonator, and an extended length of the feed line l_3 are shown. Z_p and w_p are the characteristic impedance and the width of the feed line, respectively. As the feed line is extended, a transmission zero f_{Z2}, created by the coupling between the feed lines and the resonators, tends to move to lower frequencies. Due to the properties of f_{Z2}, the harmonic suppression of the second resonant frequency f_2 of the resonators 1 or 2 is possible when f_{Z2} coincides with f_2 [45], [46]. The similar sharp feed lines and the coupling schemes combining two paths are investigated in [47], but the harmonic suppression and the precise position of the transmission zeros are not fully considered. The 50-Ω port 1 in Fig. 29(a) is directly connected to the hook-type feed line, and 50-Ω port 2 is weakly coupled to the other end of the resonator. Due to the

direct connection at port 1, f_{Z2} is not so sensitive to the gap between resonator 1 and 50-Ω port 2. Therefore, without considering the gap, EM Simulations can be fulfilled simply with varied l_2, l_3, and Z_p when d_2 = 0.18 mm. After each simulation, Q_{ex1} can be extracted by using the following equation [40]:

$$Q_{ex} = \frac{f_0}{\Delta f_{3\text{-dB}}} \tag{16}$$

where f_0 and $\Delta f_{3\text{-dB}}$ is the resonant frequency and the 3-dB bandwidth of the resonator, respectively. Fig. 29(b) shows the result of the simulations, where f_{Z2} moves to lower frequencies as l_3 becomes longer. Also, when l_3 = 9.1 mm, the f_{Z2} is located at around estimated f_2 (= 6.19 GHz). The six points for l_3 = 9.1 mm in Fig. 29(b) are analyzed more by varying l_2, d_2, and Z_p in Fig. 29(c). This figure shows that Q_{ex1} becomes larger as d_2 becomes larger, and Q_{ex1} is in inverse proportion to Z_p at a certain value of d_2. In due consideration of given Q_{ex1} from (12) and the coincidence of f_2 and f_{Z2}, the design parameters in Fig. 29(a) are determined as l_2 = 11.35 mm, l_3 = 9.1 mm, Z_p = 85 Ω (w_p = 0.27 mm), d_2 = 0.18 mm for Q_{ex1} = 15.9, and f_{Z2} = 6.29 GHz.

All the decided geometric parameters result in the layout of the 2.4-GHz BPF in Fig. 30(a). The measured and simulated results of this filter are compared in Fig. 30(b). The thick red dotted line in this figure confirms the effect of the suppression of f_2 by showing the simulated result using information at point *A* in Fig. 29(b) when l_1 = 10.0 mm and d_1 = 0.48 mm. Measured f_2 shows the suppression level of 24.3 dB. The estimated f_{Z1} (= 3.08 GHz) from Fig. 27(b), measured one (= 3.11 GHz), and simulated one (= 3.11GHz) are in good agreement. Measured results of the passband show that the

insertion loss is about 1.84 dB and the return loss is larger than 13.35 dB. Also, the measured ratio of f_3 / f_1 is 4.10, which is very close to the calculated value of 4.17 as shown in Fig. 25.

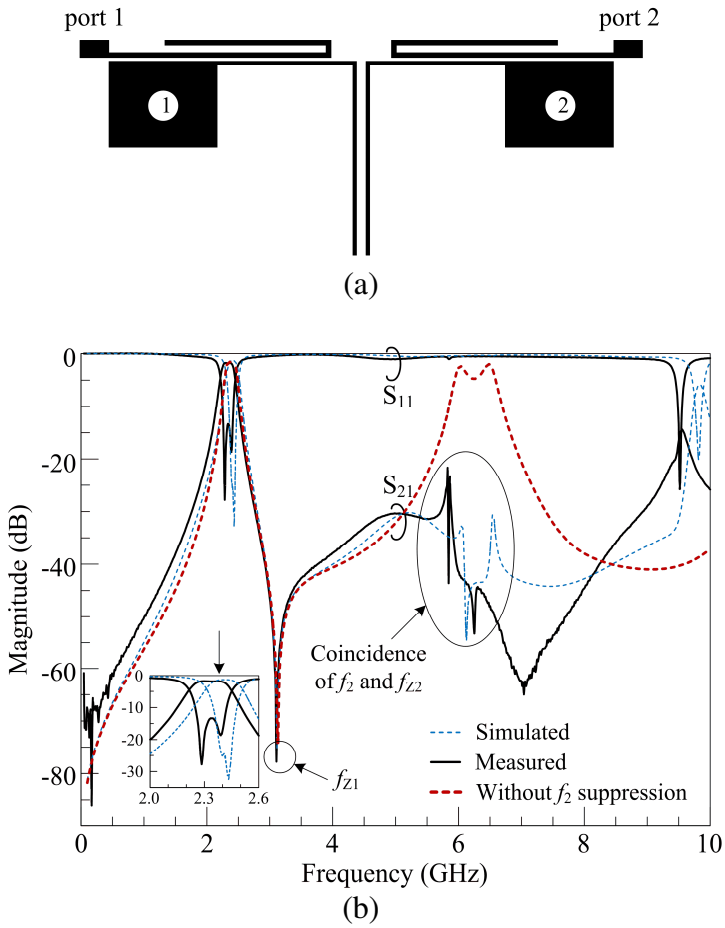

Fig. 30. 2.4-GHz BPF using the hook-type feed line. (a) Layout. (b) Simulated and measured results. Thick red dotted line of "Without f_2 suppression" shows the simulated result using information at point *A* in Fig. 29(b) when l_1 = 10.0 mm and d_1 = 0.48 mm.

B. 5.2-GHz BPF using hook-type feed lines

By following the similar procedure for designing 2.4-GHz resonators in Section 2, the geometric dimensions of the 5.2-GHz resonator can be determined. Since the third

resonant frequency of the 2.4-GHz resonator is estimated to be 10.01 GHz, the second resonance of 5.2-GHz resonator should appear at a frequency higher than 10.01 GHz to achieve a wide upper stopband. That is, $f_2 / f_1 > 1.93$, so u and K are chosen in Fig. 25 as $u = 0.40$ and $K = 0.46$. According to these values, dimensions of the resonator shown in Fig. 24 are decided as follows: $L_1 = 7.57$ mm, $W_1 = 0.37$ mm, $L_2 = 4.98$ mm and $W_2 = 1.67$ mm. The two-pole ($n = 2$) Butterworth BPF with the FBW of 4.2 % is designed. The coupling coefficients and external quality factors of this filter, as shown in Fig. 26, can be calculated by using (11) and (12), respectively, and the results are $M_{34} = 0.030$, $Q_{ex2,\,in} = Q_{ex2,\,out} = Q_{ex2} = 33.7$, where Q_{ex2} is the external quality factor at the input or output ports for resonators 3 or 4.

To extract M_{34}, the coupled resonator filters are arranged as shown in Fig. 31(a), where d_3 and l_4 are a gap between resonators and a coupled length of the resonators, respectively. By using (13), l_4 can be approximately estimated to be 6.2 mm for locating the transmission zero f_{Z3} at 6 GHz. On top of that, f_{Z3} can be precisely decided by following the similar flowchart in Fig. 28. The obtained Q_u (= 167) for resonators 3 or 4 and the designated value of Q_{EX} (= 1) are used for calculating L_A in Step 4 of the flowchart. Through several simulations with varied values of d_3, l_4, and g, the coupling coefficient M_{34} and f_{Z3} can then be extracted. The results of these simulations are plotted in Fig. 31(b), where the effects of the varied geometric parameters on both the coupling coefficients and the transmission zeros are observed to be very similar to those in Fig. 27(b). By considering both the transmission zero, designed to make a sharp upper

rejection, and the given value of M_{34}, design parameters are determined as l_4 = 4.6 mm, d_3 = 0.67 mm while M_{34} = 0.027 and f_{Z3} = 5.79 GHz.

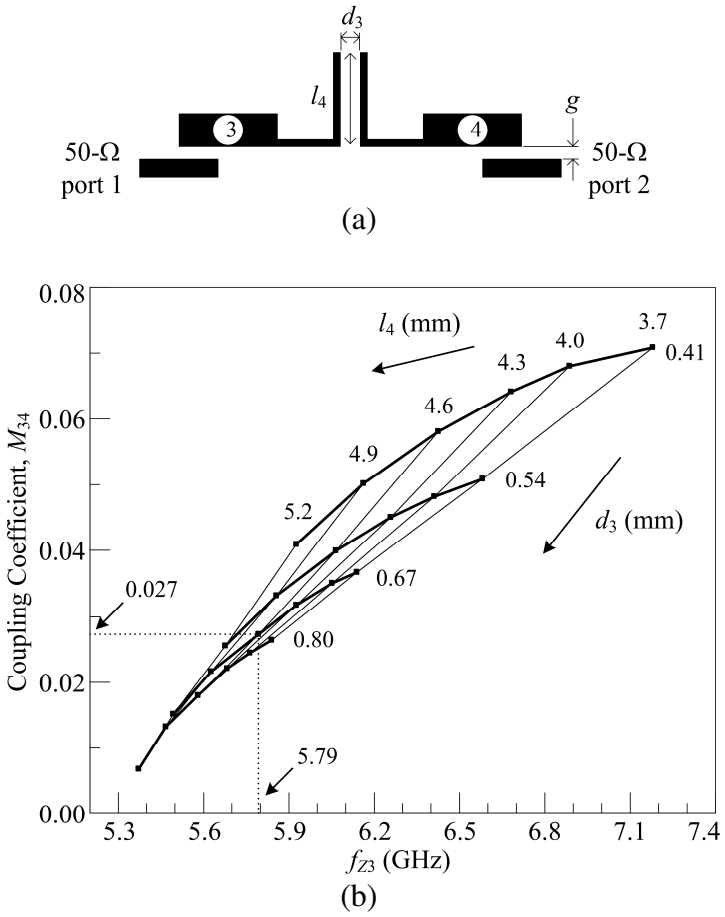

Fig. 31. Analysis of a Coupling coefficient M_{34}. (a) Arrangement for EM simulation. (b) Design graph for resonators 3 and 4.

Since the design of the extended hook-type feed lines has been given in Section 3-A, a gap d_4 between resonator 3 and the feed lines, as shown in Fig. 32(a), is the only parameter left to be decided. An arrangement of EM simulations for extracting Q_{ex2} is shown in Fig. 32(a), and design graphs for d_4 are plotted in Fig. 32(b). A transmission

zero f_{Z4}, resulting from the coupling between the resonator 3 and the feed line, is designed to appear at the lower side of the passband. The two sides of Fig. 32(b) have the same information, and Q_{ex2} is observed to be in almost inverse and direct proportion to f_{Z4} and d_4, respectively. From this figure, the gap is decided as d_4 = 0.40 mm for Q_{ex2} = 32.3 and f_{Z4} = 3.79 GHz.

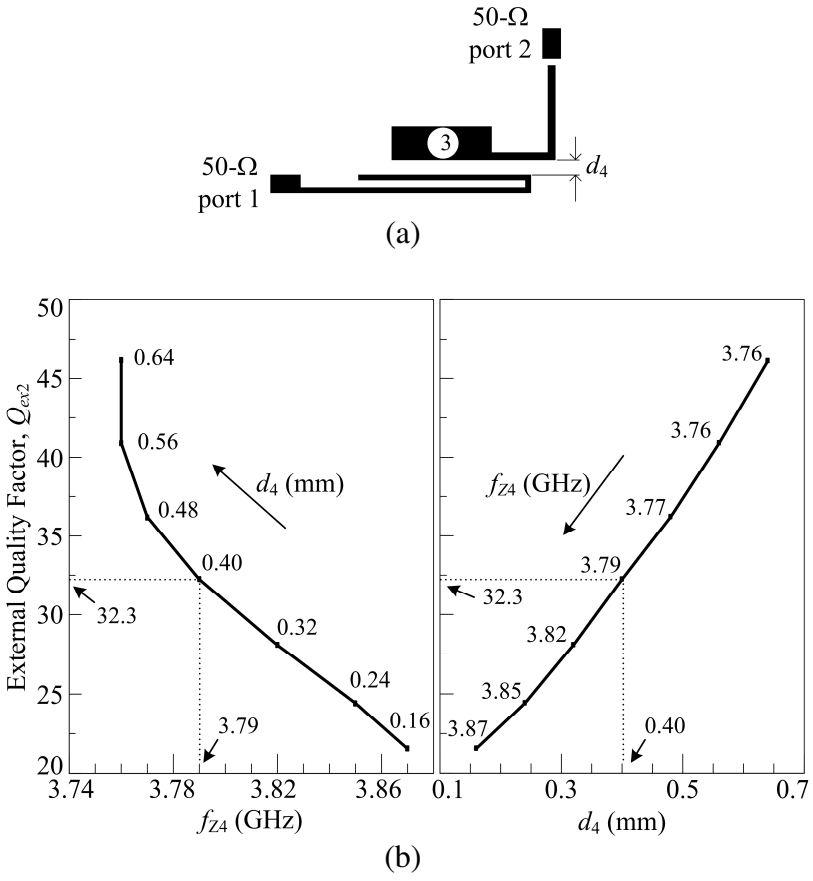

Fig. 32. Analysis of an external quality factor Q_{ex2}. (a) Arrangement for EM simulation. (b) Design graph for a gap d_4.

Fig. 33(a) shows the layout of the 5.2-GHz BPF using the hook-type feed lines based on the decided design parameters. The measured and simulated results are

compared in Fig. 33(b), where the estimated f_{Z3} and f_{Z4} (5.79 and 3.79 GHz) from Figs. 31 and 32, can be compared with the measured results (5.81 and 4.10 GHz), and the simulated results (5.94 and 4.22 GHz), respectively. Measured results of the passband show that the insertion loss is about 2.88 dB and the return loss is larger than 10.15 dB.

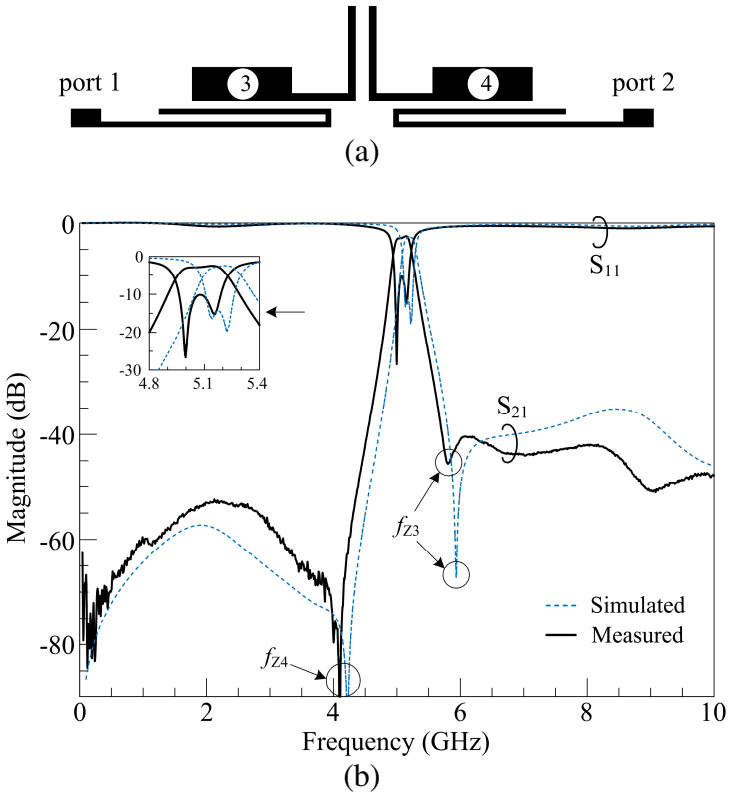

Fig. 33. 5.2-GHz BPF using the hook-type feed line. (a) Layout. (b) Simulated and measured results.

C. Dual-band BPF using hook-type feed lines

The layout of the dual-band BPF is shown in Fig. 34(a), and simulated and measured results are compared in Fig. 34(b). For effective suppression of the second resonance of the resonators 1 or 2, as already shown in Fig. 30(b), either length of the

extended feed lines can be made different to make two split transmission zeros of f_{Z2}. That is, for the layout in Fig. 34, each l_3, indicated in Fig. 29(a), is revised to be increased by 1.0 mm and decreased by 0.1 mm for the left and right feed lines, respectively. As a result, the suppression is measured as the level of 21.6 dB in Fig. 34(b).

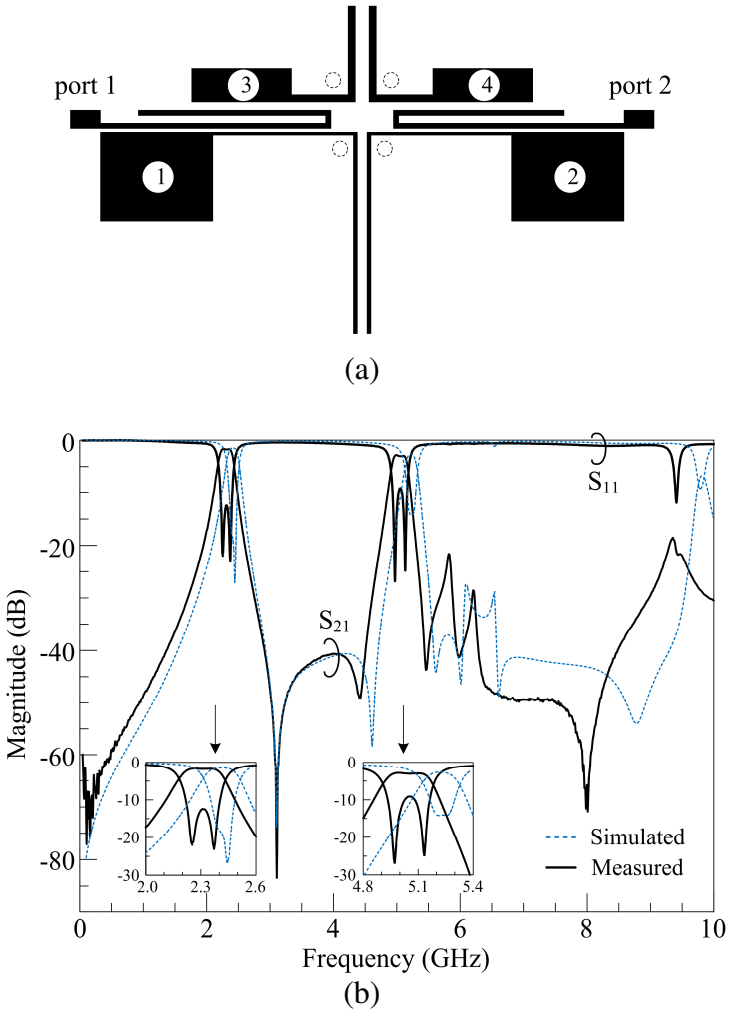

Fig. 34. Dual-band BPF using the hook-type feed line. (a) Layout. Dotted circles indicate prospective locations of via-holes and PIN diodes for an independent control of dual passbands. (b) Simulated and measured results.

In this figure, the measured results show that the FBWs are 9.9 and 5.4 %, insertion losses are approximately 1.75 and 3.03 dB, and return losses are larger than 12.41 and 9.11 dB for the lower and higher passbands, respectively. The losses are mainly caused by fabrication errors in both the sharp feed lines and the narrow coupling gaps, and the unexpected coupling between resonators 1 and 3 or between resonators 2 and 4 could worsen the return losses compared to those in Figs. 30(b) and 33(b). Table 4 lists the geometric dimensions of the layout in Fig. 34(a) based on the previous design graphs.

Table 4. Geometric parameters in Fig. 34.

2.4-GHz resonator				5.2-GHz resonator				unit is mm
L_1	W_1	L_2	W_2	L_1	W_1	L_2	W_2	
17.1	0.2	5.6	4.5	7.57	0.37	4.98	1.67	
l_1	l_2	l_3	l_4	d_1	d_2	d_3	d_4	w_p
10.0	11.35	9.1(+1.0/-0.1)	4.6	0.48	0.18	0.67	0.40	0.27

4. BPFs using spiral-type feed lines

As mentioned briefly at the beginning of Section 3, to control dual bands independently, via-holes and PIN diodes are supposed to be located approximately at dotted circles, as indicated in Fig. 34(a). However, because the upper two dotted circles are surrounded by the resonators 3 and 4, the via-holes could affect the 5.2-GHz resonant frequency as if they were small resonators in a particular state that does not need ground. It can be assumed that resonators 1 and 2 are not affected by the via-holes as much as resonators 3 and 4 because of their relatively large size. Therefore, in this

section, modified resonators 3 and 4, i.e., resonators 3' and 4', are designed to be affected by via-holes as little as possible in the particular state. Moreover, resonators 3 and 4 are coupled with folded parts of the hook-type feed lines. By using spiral-type feed lines, resonators 3' and 4' are attempted to be located as near as possible to the 50-Ω ports in order to improve the loss responses. The coupling structure of the BPF using the spiral-type feed lines is shown in Fig. 35. Solid circles with numbers 1 and 2 denote 2.4-GHz resonators, and those with numbers 3' and 4' denote 5.2-GHz resonators. Prime marks are appended to indicate the use of the spiral-type feed lines. Resonators 1 and 2 in this figure are the same as those used in Section 3. $Q'_{ex1,\ in}$ and $Q'_{ex1,\ out}$ are the external quality factors at the input and output ports for 2.4-GHz resonators, respectively, and $Q'_{ex2,\ in}$ and $Q'_{ex2,\ out}$ are those for 5.2-GHz resonators. M_{12} and $M_{3'4'}$ are the coupling coefficients for 2.4-GHz resonators and 5.2-GHz resonators, respectively. M_{12} is the same as the value used in Section 3 because it is not affected by new feed lines.

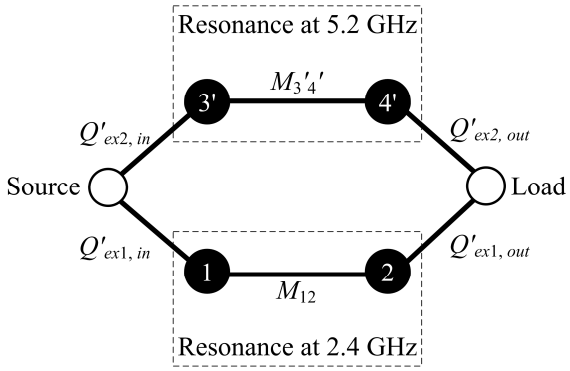

Fig. 35. Coupling structure of BPFs using spiral-type feed lines. Solid circles with numbers 1 or 2 denote 2.4-GHz resonators, and those with numbers 3′ or 4′ denote 5.2-GHz resonators. Prime marks are appended to indicate the use of the spiral-type feed lines.

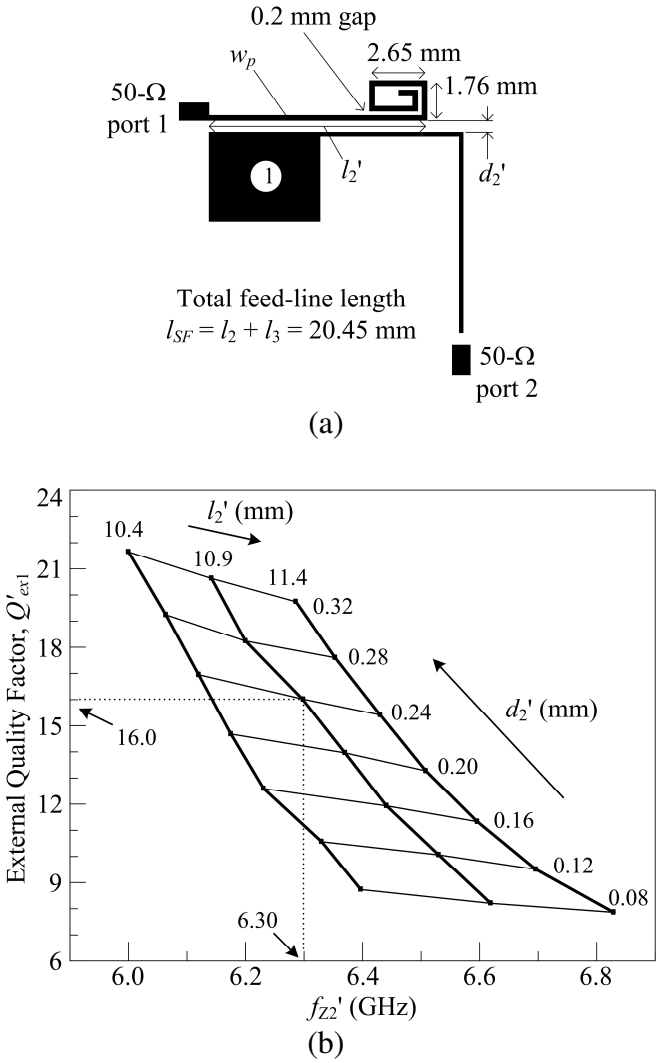

Fig. 36. Analysis of an external quality factor Q'_{ex1}. (a) Arrangement for EM simulation. (b) Design graph for a spiral-type feed line. A feed-line width w_p and a total feed-line length l_{SF} are the same as those of the hook-type feed lines.

A. 2.4-GHz BPF using spiral-type feed lines

The two-pole (n = 2) Butterworth BPF with the FBW of 8.6 % is designed for 2.4-GHz filters. By using (11) and (12), the coupling coefficient and the external quality factor at the input or output ports are calculated as M_{12} = 0.061 and $Q'_{ex1,\,in} = Q'_{ex1,\,out} = Q'_{ex1}$ = 16.4, respectively. For resonators 1 or 2, the design parameters decided in Fig. 27

are used again. For the design of the spiral-type feed lines, three design parameters and three decided dimensions are shown in Fig. 36(a). Three dimensions in this figure are for a spiral size and a gap between spiral lines, and they are schemed for an appropriate shape of a 5.2-GHz resonator. Total length of the spiral-type feed line l_{SF} and its width w_p are assumed to be the same as those of the hook-type feed lines: $l_{SF} = l_2 + l_3 = 20.45$ mm and $w_p = 0.27$ mm. Thus the coupled-section length l_2' and gap d_2' between the feed lines and the resonator need to be determined. A transmission zero f_{Z2}', created by the coupled section between the feed line and the resonator, tends to move to lower frequencies as the feed lines are extended. By allowing for both the suppression of the second resonant frequency f_2 by the coincidence of f_{Z2}' and the given value of Q'_{ex1}, the design parameters are decided as $l_2' = 10.9$ mm, $d_2' = 0.24$ mm for $Q'_{ex1} = 16.0$ and $f_{Z2}' = 6.30$ GHz, as shown in Fig. 36(b).

Fig. 37(a) shows the layout of the 2.4-GHz BPF using the spiral-type feed lines. The measured and simulated results are compared in Fig. 37(b). Measured f_2 shows the suppression level of 28.0 dB. The estimated f_{Z1} (= 3.08 GHz) from Fig. 27(b), measured one (= 3.07 GHz), and simulated one (= 3.06GHz) are in good agreement. Measured results of the passband show that the insertion loss is about 2.15 dB and the return loss is larger than 10.79 dB. In addition, the measured ratio of f_3 / f_1 is 4.06, which is very close to the calculated value of 4.17 in Fig. 25.

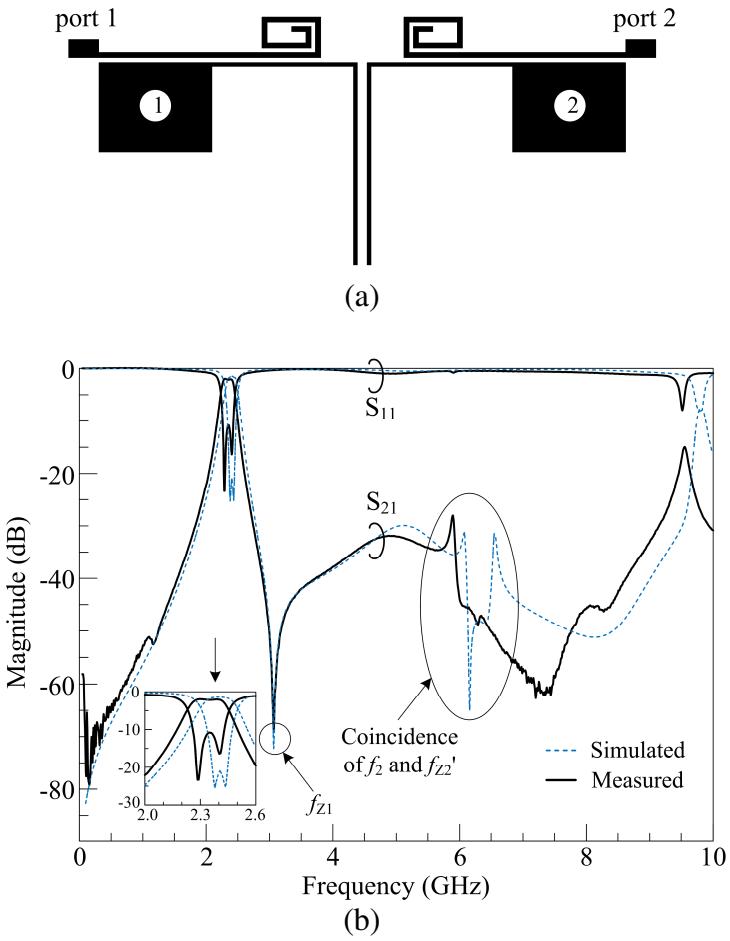

Fig. 37. 2.4-GHz BPF using the spiral-type feed line. (a) Layout. (b) Simulated and measured results.

B. 5.2-GHz BPF using spiral-type feed lines

5.2-GHz resonators can be designed by considering f_2 / f_1 > 1.93 (the same condition used in Section 3-B), the prospective locations of via-holes, and the shape of the spiral-type feed lines. The values of u and K are chosen in Fig. 25 as u = 0.30 and K = 0.31, and dimensions of the resonator shown in Fig. 24 are determined as follows: L_1 = 7.71 mm, W_1 = 0.37 mm, L_2 = 3.30 mm and W_2 = 2.87 mm. The two-pole (n = 2) Butterworth BPF is designed with the FBW of 5.1 %.

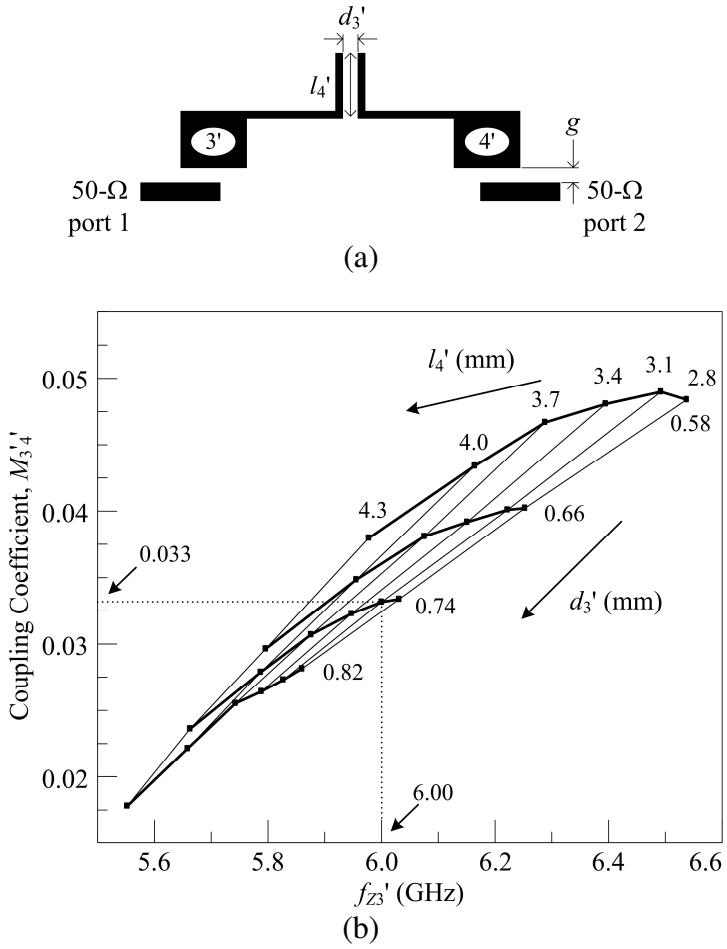

Fig. 38. Analysis of a coupling coefficient $M_{3'4'}$. (a) Arrangement for EM simulation. (b) Design graph for resonators 3' and 4'.

The coupling coefficients and external quality factors of this filter can be calculated by using (11) and (12), respectively, and the results are $M_{3'4'} = 0.036$ and $Q'_{ex2,\ in} = Q'_{ex2,\ out} = Q'_{ex2} = 27.7$, where Q'_{ex2} is the external quality factor at the input or output ports for resonators 3' or 4'. Using the same manners in Section 3-B, $M_{3'4'}$, Q'_{ex2}, and two transmission zeros can be extracted by EM simulations with varied design parameters in Figs. 38(a) and 39(a). From the design graphs plotted in Fig. 38(b), the design parameters are chosen as $l_4' = 3.1$ mm, $d_3' = 0.74$ mm while $M_{3'4'} = 0.033$, $f_{Z3}' = 6.00$

GHz. Also from Fig. 39(b), d_4' is chosen to be 0.23 mm when Q'_{ex2} = 27.1 and f_{Z4}' = 3.35 GHz. f_{Z3}' is designed to appear at the upper side of the passband by the coupling between resonator 3' and 4', and f_{Z4}' is created at the lower side of the passband by the coupling between resonators 3' and the spiral-type feed lines. Either figure of Fig. 39(b) has the same information, and Q'_{ex2} is observed to be in almost direct proportion to both f_{Z4}' and d_4'.

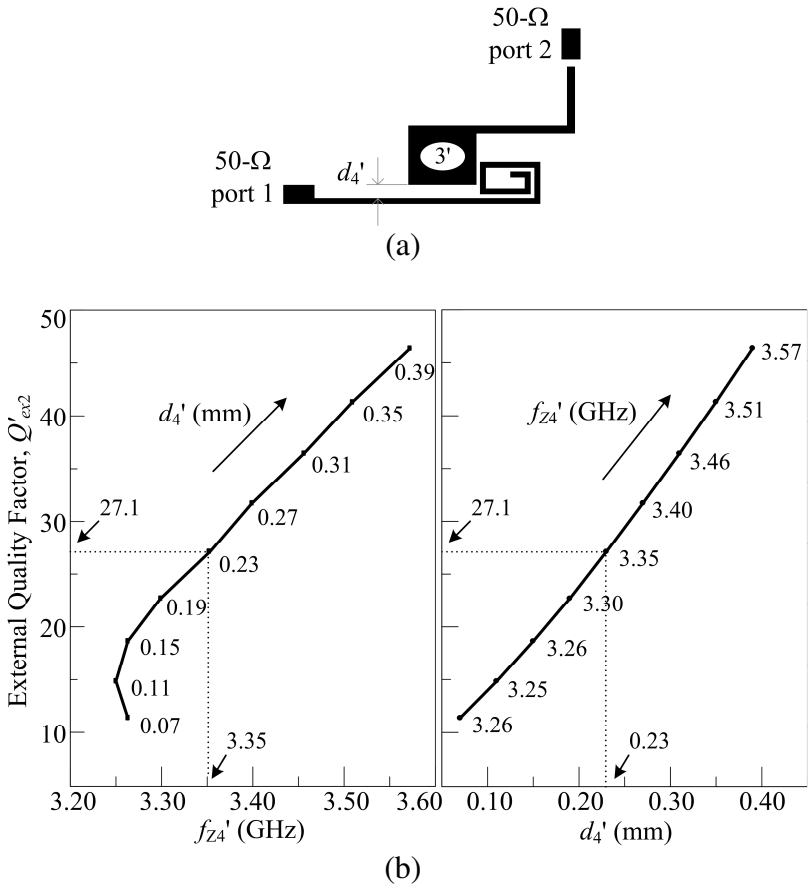

Fig. 39. Analysis of an external quality factor Q'_{ex2}. (a) Arrangement for EM simulation. (b) Design graphs for a gap d_4'.

The layout of the 5.2-GHz BPF using the spiral-type feed lines is shown in Fig. 40(a), and the measured and simulated results are compared in Fig. 40(b). In this figure,

the estimated f_{Z3}' and f_{Z4}' (6.00 and 3.35 GHz), obtained from Figs. 38 and 39, can be compared with the measured results (6.92 and 3.92 GHz) and the simulated results (6.33 and 4.14 GHz), respectively. Measured results of the passband show that the insertion loss is about 2.01 dB and the return loss is larger than 15.65 dB. These loss responses are better than the results from the 5.2-GHz BPF using hook-type feed lines in Section 3-B, and this would be due to the simpler coupling between the resonators 3' or 4' and the spiral-type feed lines, where resonators 3' or 4' lie very near to the 50-Ω ports.

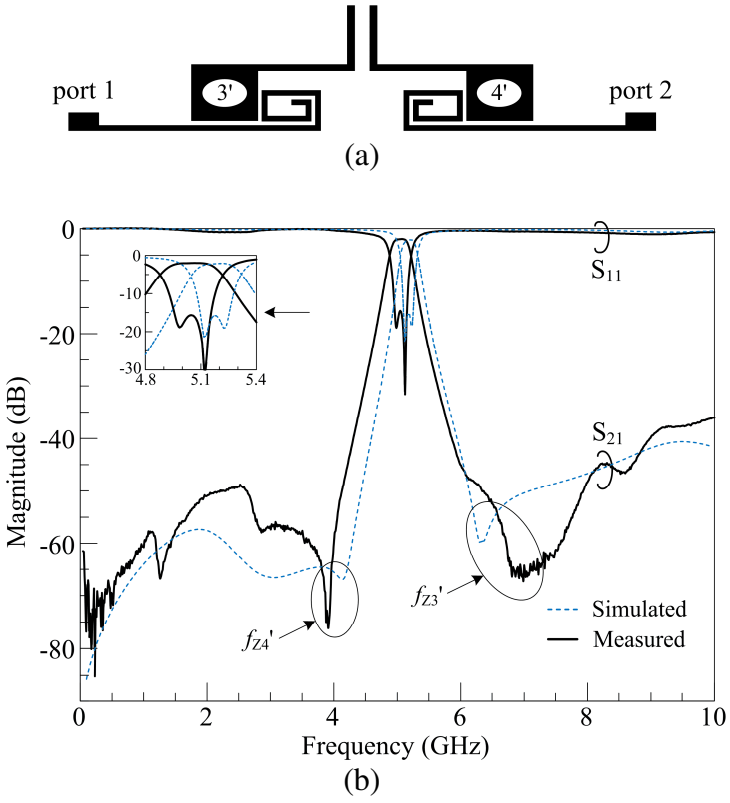

Fig. 40. 5.2-GHz BPF using the spiral-type feed line. (a) Layout. (b) Simulated and measured results.

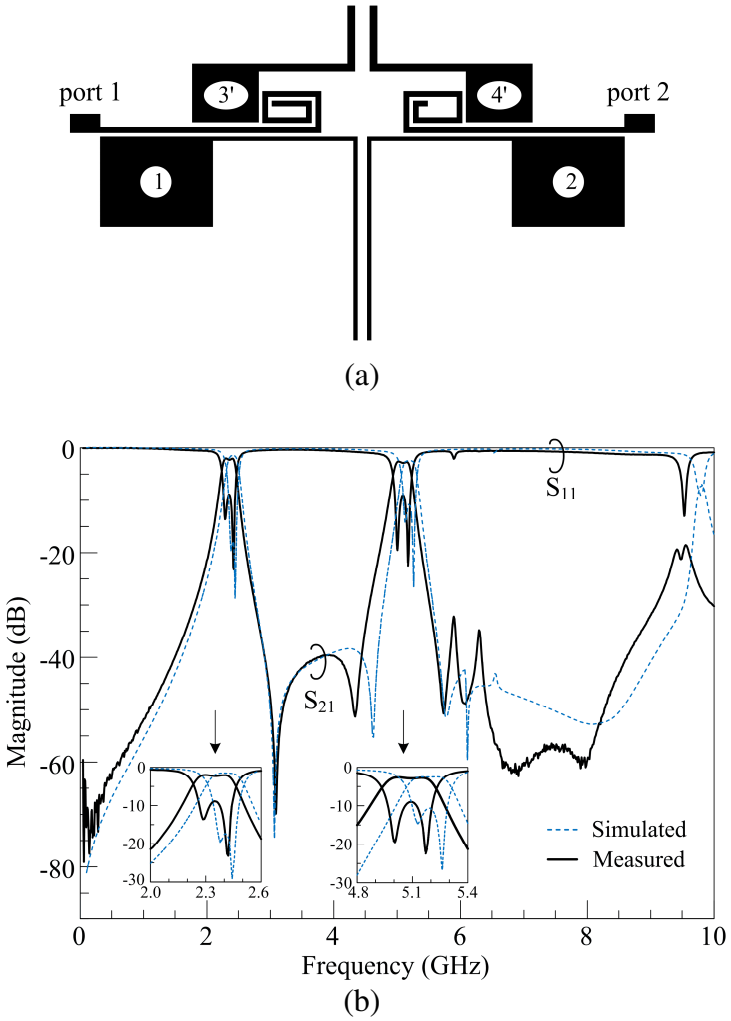

Fig. 41. Dual-band BPF using the spiral-type feed line. (a) Layout. (b) Simulated and measured results.

Table 5. Geometric parameters in Fig. 41.

2.4-GHz resonator				5.2-GHz resonator				unit is mm
L_1	W_1	L_2	W_2	L_1	W_1	L_2	W_2	
17.1	0.2	5.6	4.5	7.71	0.37	3.30	2.87	
l_1	l_2'	l_4'	d_1	d_2'	d_3'	d_4'	w_p	l_{SF}
10.0	10.9	3.1	0.48	0.24	0.74	0.23	0.27	20.45(+1.0/-0.25)

C. Dual-band BPF using spiral-type feed lines

The layout of the dual-band BPF using spiral-type feed lines is shown in Fig. 41(a), and the simulated and measured results are compared in Fig. 41(b). For the effective suppression of the second resonant frequency of the resonators 1 or 2 by the overlap of f_{Z2}', as already shown in Fig. 37(b), either length of the spiral-type feed lines can be made different to make two transmission zeros. That is, total length of the feed line l_{SF} is increased by 1.0 mm or decreased by 0.25 mm for the left and right feed lines, respectively, without changing l_2' (= 10.9 mm) in Fig. 36. As a result, the suppression is measured up to the level of 32.2 dB in Fig. 41(b). In this figure, the measured results show that the FBWs are 10.3 and 6.0 %, insertion losses are approximately 2.27 and 2.88 dB, and return losses are larger than 8.88 and 9.00 dB for the lower and higher passbands, respectively. As mentioned earlier in Section 3, the unexpected coupling between resonators 1 and 3' or between resonators 2 and 4' could make loss responses a little bit worse than those in Figs. 37(b) and 40(b). The geometric dimensions used in the layout of Fig. 41(a) are listed in Table 5.

5. Design of a switchable dual-band BPF

To design an independently controllable dual-band filter, the layout in Fig. 41(a) is used. In addition to this basic layout, four PIN diodes (MACOM, MA4AGSBP907), used as switches for connecting or disconnecting 2.4- or 5.2-GHz signal paths, and four inductors L_1 ~ L_4 with 330 nH, used as RF chokes, are inserted as shown in Fig. 42. Four via-holes are also needed for bypassing 2.4- or 5.2-GHz signals into the ground plane

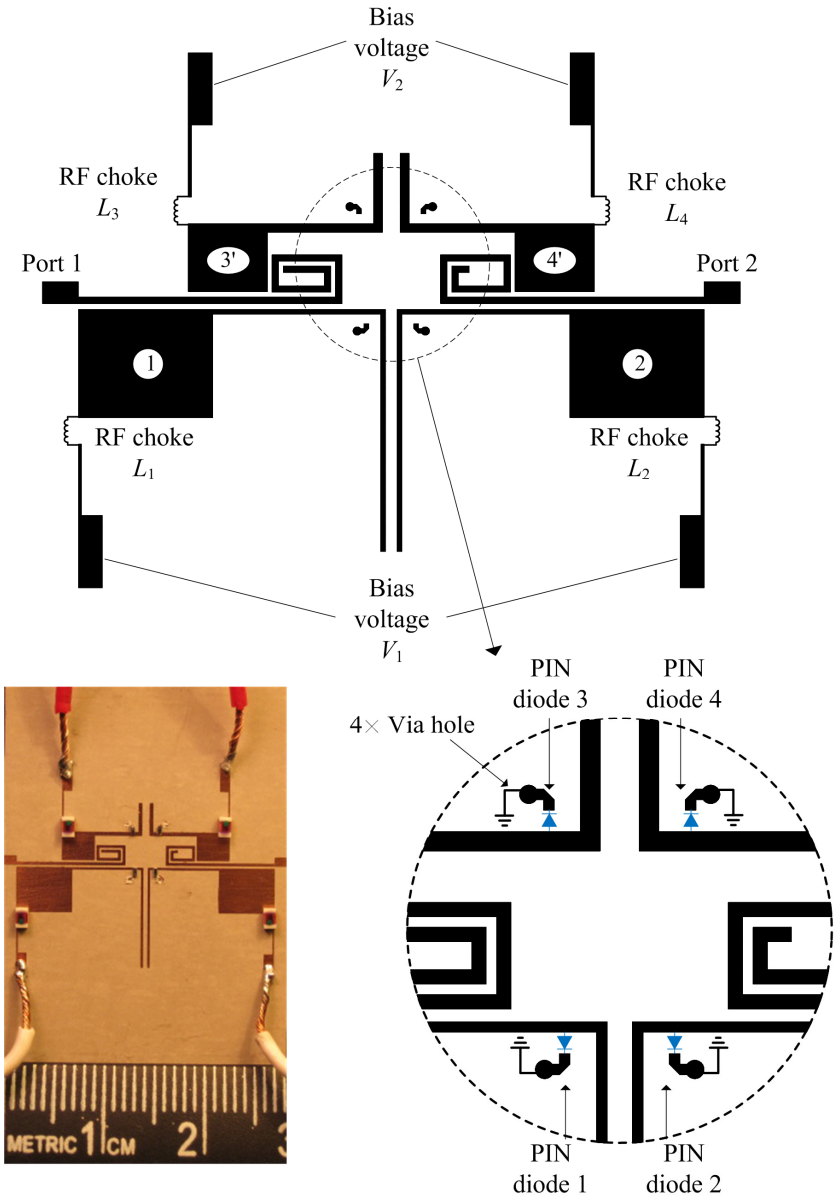

Fig. 42. The independently controllable dual-band BPF using four PIN diodes. Basic layout is the same as the one in Fig. 41(a).

when a particular signal path is disconnected by the PIN diodes. The most effective locations for disconnecting the signal paths are investigated by EM simulations, and then PIN diodes and via-holes are decided to be located at right-angled corners of each

resonator, as shown in Fig. 42. For the simulations, the PIN diodes are replaced with 4-Ω resistors or 25-fF capacitors for expressing on- or off-states, respectively. Because the via-holes could affect the resonant frequency in a certain state that does not need ground, the diameter of the via-hole is chosen as 0.34 mm, the smallest feasible size. Also, the via-holes are attempted to be located at appropriate points, far from resonators but near the PIN diodes. There are two bias voltages V_1 and V_2, and V_1 controls PIN diodes 1 and 2, and V_2 controls PIN diodes 3 and 4 at a time. The PIN diodes stay turned off if there are no bias voltages.

In Fig. 43, measured and simulated results are shown for four states of the dual-band BPF. For the case of no bias voltage at V_1 and V_2, 2.4 and 5.2-GHz peaks are well observed in Fig. 43(a) because all the PIN diodes remain turned off. By adding only V_1 of 1.2V with forward current of 2 mA, PIN diodes 1 and 2 are turned on. Then RF signals, supposed to make 2.4-GHz resonances by passing through resonators 1 and 2, go to the ground plane through the via-holes. Therefore, only a 5.2-GHz peak is observed in Fig. 43(b). Conversely, by adding only V_2, PIN diodes 3 and 4 are turned on. Then RF signals in resonator 3' and 4' go to the ground plane, and only a 2.4-GHz resonant peak appears in Fig. 43(c). For the case of adding V_1 and V_2 at the same time, no resonances are observed in Fig. 43(d), as expected, because all the PIN diodes are turned on and then RF signals in all the resonators are sent to the ground plane. For the 5.2-GHz peaks in Figs. 43(a) and (b), slight discrepancies between the simulation and the measured result are observed. These could result from the reason that the smaller resonators 3' and 4' could be disturbed by the via-holes, relatively large inductors, and

conductive glue, used for bonding PIN diodes and inductors, more seriously than resonators 1 and 2.

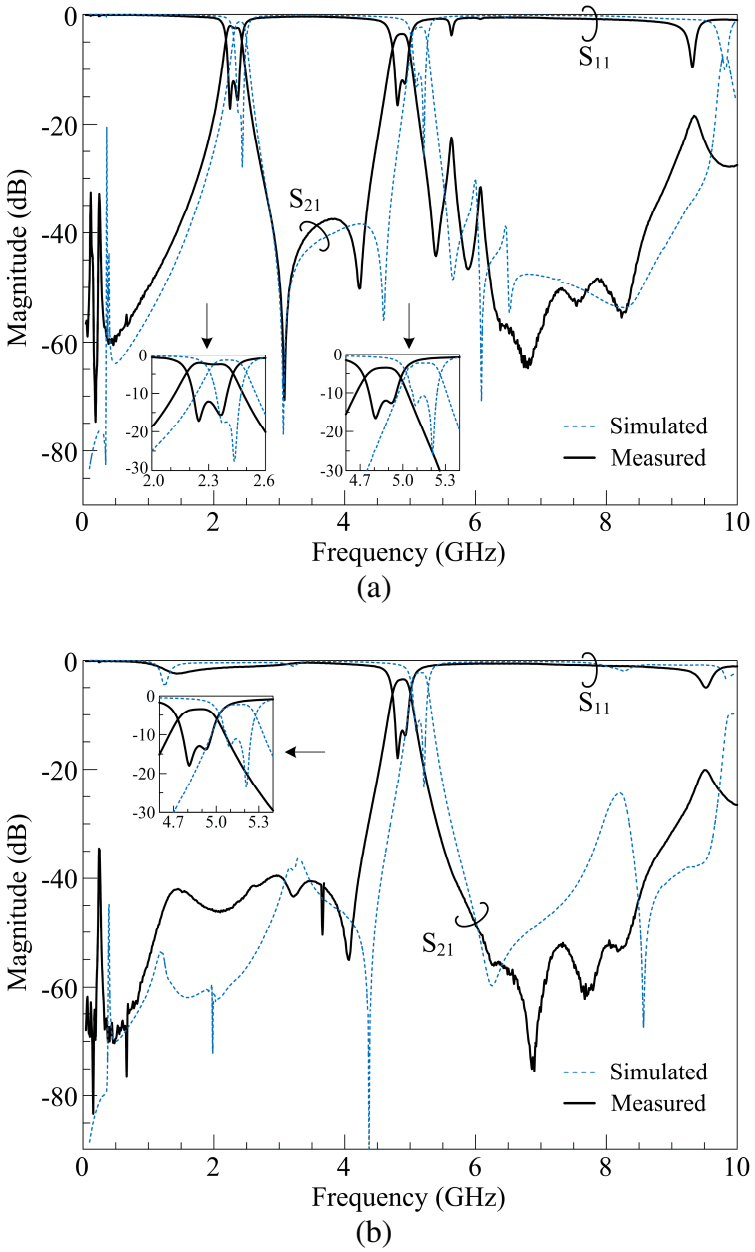

Fig. 43. Measured and simulated results in four states of the dual-band BPF in Fig. 42. (a) With no bias. (b) With bias V_1 added. (c) With bias V_2 added. (d) With bias V_1 and V_2 added simultaneously.

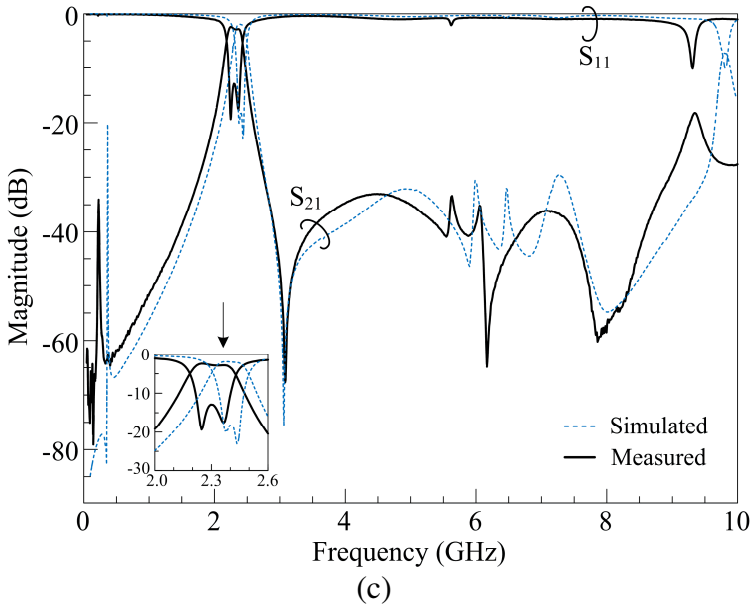

(c)

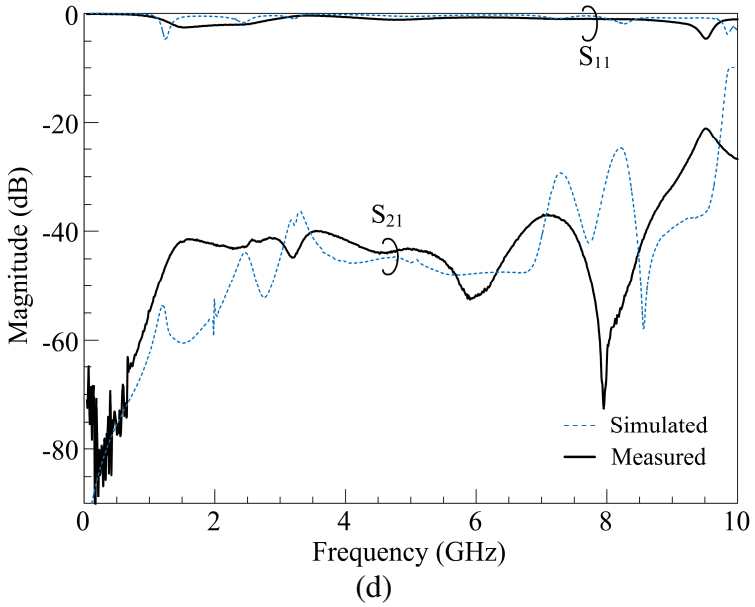

(d)

Fig. 43. Continued.

In measured results of dual bands in Fig. 43(a), minimum insertion losses are 2.06 and 3.50 dB, and return losses are larger than 12.14 and 11.99 dB at the lower and upper passbands, respectively. In measured results of each single band in Figs. 43(b) and

(c), minimum insertion losses are 3.43 and 2.40 dB, and return losses are larger than 12.96 and 12.91 dB, respectively.

6. Conclusion

An independently switchable dual-band filter has been developed by using asymmetric SIRs and extended feed lines. The asymmetric SIRs have been designed by considering the ratio of the harmonic frequencies, and the second resonant frequency of the 2.4-GHz resonator has been suppressed by the transmission zero created by the extended feed lines. Design graphs for geometric parameters and transmission zeros have been provided. While plotting the design graphs regarding the coupling coefficients M_{12}, M_{34}, and $M_{3'4'}$, a flowchart has been supplemented for extracting precise transmission zeros f_{Z1}, f_{Z3}, and $f_{Z3'}$, respectively. Hook- and spiral-type feed lines have been developed, and the latter is chosen for achieving the feature of switchable bands. By controlling the bias voltages added to PIN diodes, four states of responses, such as a 2.4-GHz band only, a 5.2-GHz band only, dual bands, and no transmission state, are clearly presented.

CHAPTER V

MINIATURIZED PIEZOELECTRIC TRANSDUCER CONTROLLED PHASE SHIFTERS USING MEANDERED MICROSTRIP LINES

1. Introduction

A phase shifter plays an important part in microwave and millimeter wave systems. Most significantly, antenna beams can be steered by using the electrical delay made by the phase shifters. The conventional phase shifter, using dielectric perturbation controlled by piezoelectric transducer (PET), is usually realized on straight microstrip lines, and it is useful in very wideband applications because the perturbation just makes a slight effect on the characteristic impedance [48]. To obtain more phase shifts, PET-controlled phase shifters are also realized on a coplanar waveguide [49] and a coplanar strip line [50]. They provide 50 % more phase shifts compared to microstrip lines, but these methods do not reduce the size of the circuit effectively.

In this chapter, compact meandered microstrip lines and a miniaturized dielectric perturber are designed to obtain comparable differential phase shifts as achieved by PET-controlled phase shifter with straight microstrip lines. To perturb the meandered microstrip line effectually, a pyramid-shaped perturber is designed. In addition, adapter circuits are added to the phase shifter circuit for measuring the differential phase shift appropriately. The differential phase shifts are measured and compared with the results of the conventional phase shifter using straight microstrip lines.

2. Meandered microstrip lines and pyramid-shaped perturber

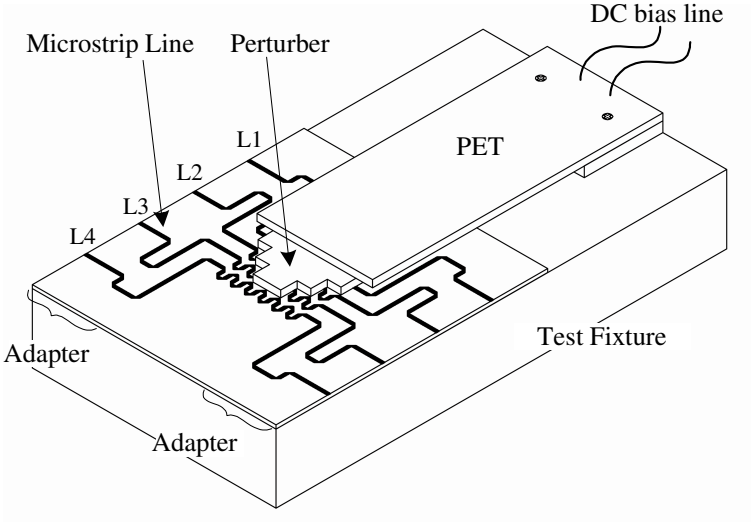

Fig. 44. Configuration of a phase shifter using dielectric perturbation controlled by a PET on meandered microstrip lines.

Fig. 44 shows the configuration of the proposed phase shifter, where four meandered microstrip lines are used with a dielectric perturber to obtain a progressive phase shift Φ from each line. The perturber is attached to the end of a PET, and it can be moved down to touch microstrip lines as applied DC voltage increases up to 90 V. There is no deflection of the PET at 0 V. As the air gap between the microstrip line and the perturber is varied according to the change of voltage, the line capacitance is varied [51]. Then, the capacitance variations cause the variations in the effective dielectric constant and the phase shift on each microstrip line. For the comparison with the PET-controlled phase shifter realized on straight microstrip lines in [52], the same measuring conditions are set up. Specifically, a 25 mil-thick RT/Duroid 6010.8 substrate with a dielectric

constant of 10.8, a 22 mil-width microstrip line, a 50 mil-thick perturber with a dielectric constant of 10.8, and the PET of the same size in [52] are used. The phase shifter in [52] utilize four straight microstrip lines, which produce differential phase shifts of 70, 140, and 210º at 10 GHz. These differential phase shifts are aimed to achieve for the proposed phase shifter, and the size reducing effect of the new phase shifter is examined.

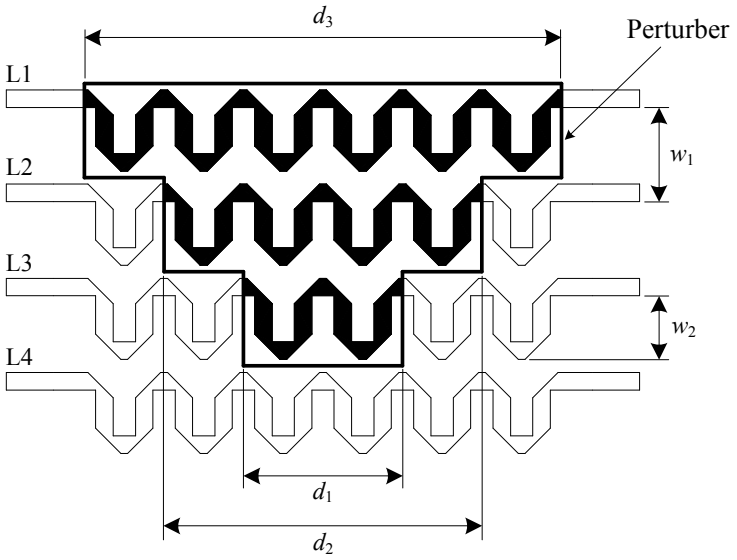

Fig. 45. Layout of meandered microstrip lines and pyramid-shaped perturber. (d_1 = 0.2 in, d_2 = 0.4 in, d_3 = 0.6 in, w_1 = 0.12 in, w_2 = 0.08 in)

The layout of the meandered microstrip lines is shown in Fig. 45. The optimum amount of chamfering is determined by the empirical expressions in [53]. The pyramid-shaped perturber is used to perturb different lengths of each three line L1, L2, and L3, and to achieve the aimed phase shifts from each line. The microstrip lines under the perturber are represented as solid line in Figs. 45 and 46. In Fig. 46, the meandered microstrip lines are compared with straight lines in terms of size. By using this novel

design of the proposed phase shifter, the length of the circuit in the longitudinal direction is reduced to 1/3, and the weight of perturber is reduced to 16 % as compared to the straight-line circuit. The reduced weight should significantly reduce the response time and increase the beam-steering speed for radar and communication systems. Fig. 47 shows the fabricated miniaturized phase shifter composed of the meandered microstrip lines and the pyramid-shaped perturber.

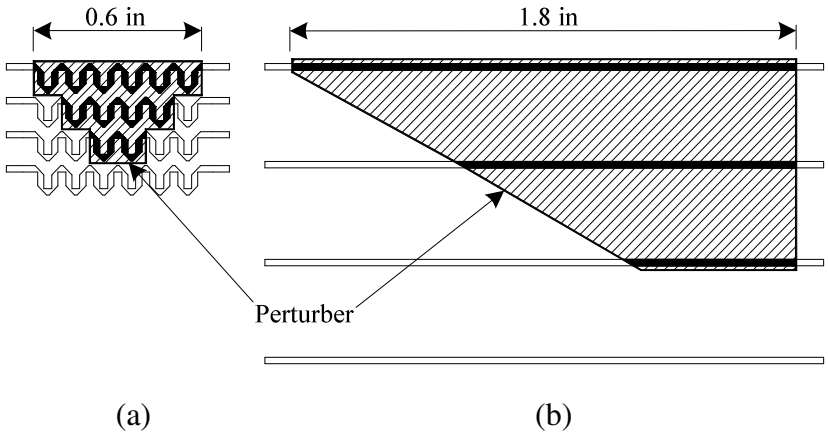

Fig. 46. Size comparison: (a) meandered microstrip line circuit and (b) straight microstrip line circuit in [52].

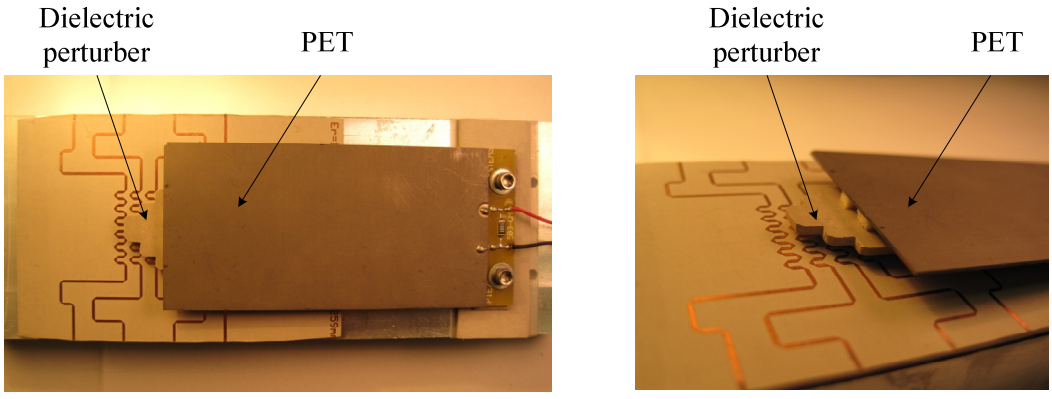

Fig. 47. A fabricated miniaturized phase shifter controlled by a PET.

3. Experimental results

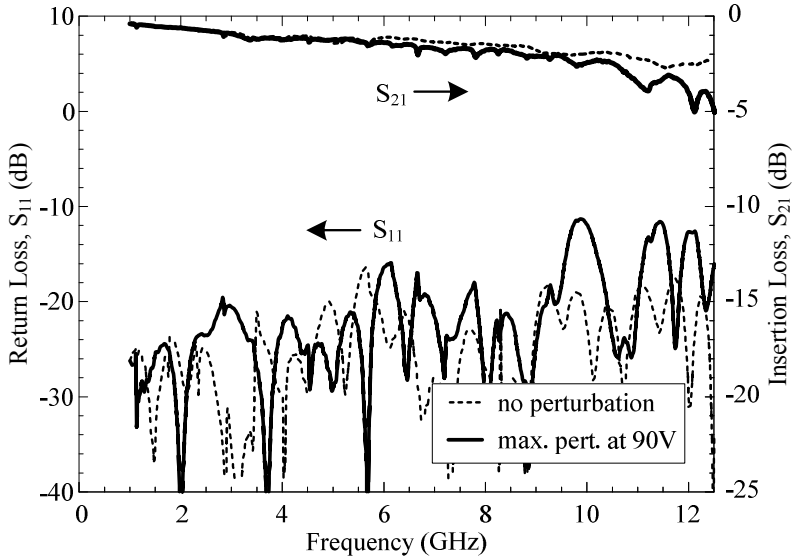

Fig. 48. S-parameter of the PET controlled phase shifter using meandered microstrip lines with and without dielectric perturbation on line 1.

Fig. 48 shows that the insertion loss (S_{21}) of less than 5 dB and the return loss of better than 10 dB are measured up to 12.5 GHz in line 1, denoted by L1, in Figs. 44 and 45, under maximum perturbation. Without the adapter circuits in Fig. 44 and connectors used in the measurements, the loss would be reduced by 2 to 3dB. In the actual integrated circuit system applications, the adapter circuits and connectors are not needed.

Fig. 49 shows the differential phase shifts $\Delta\Phi_n$, which are expressed by

$$\Delta\Phi_n = \Phi_{4,\,unpert} - \Phi_{n,\,pert}, \quad n = 1, 2, \text{ and } 3 \tag{17}$$

where $\Phi_{4,\,unpert}$ is the phase shift of the unperturbed line L4, and $\Phi_{n,\,pert}$ is the phase shift of the perturbed line, L1, L2, and L3. $\Phi_{n,\,pert}$ is usually larger than $\Phi_{4,\,unpert}$, so $\Delta\Phi_n$ has a negative value. Even if the perturber seems to lie very close to line L4 in Fig. 45, the

phase shift of this line L4 is barely affected by the perturber. Therefore, especially when $n = 4$, $\Delta\Phi_4$ with maximum perturbation, i.e. with the applied voltage of 90 V, is mostly less than 1° up to 12.5 GHz. For the line L1, L2, and L3, as the applied voltage increases,

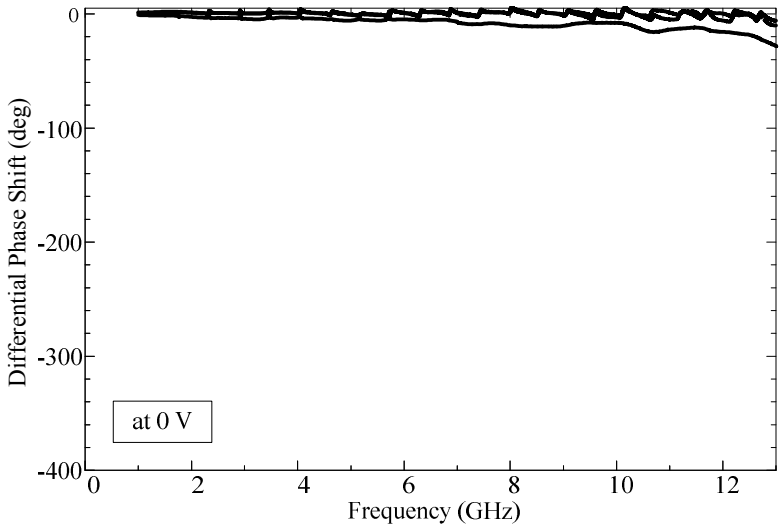

(a)

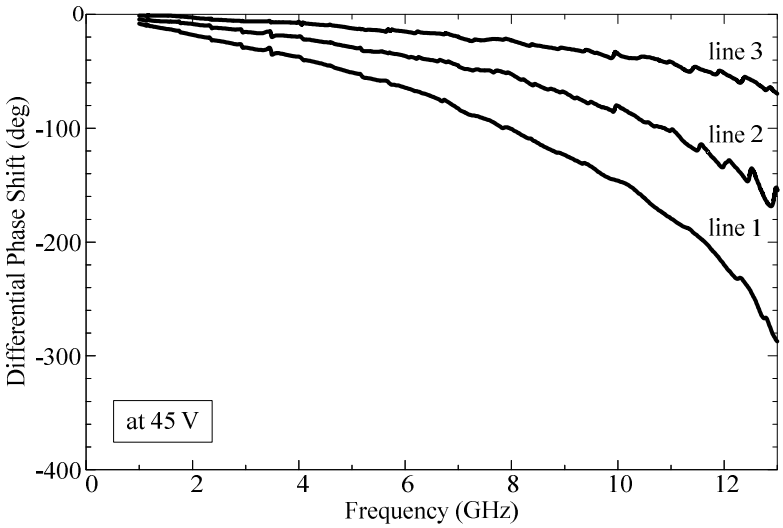

(b)

Fig. 49. Differential phase shifts with respect to the line 4 versus frequency at different PET applied voltages. (a) 0 V. (b) 45 V. (c) 90 V.

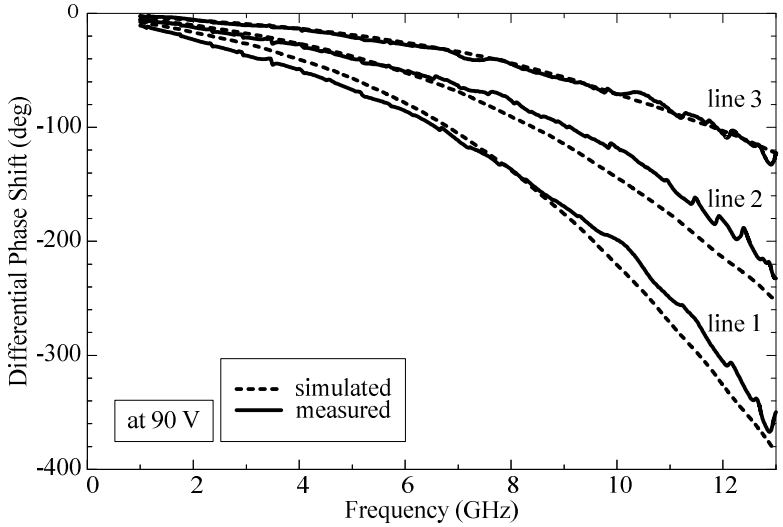

(c)

Fig. 49. Continued.

the differential phase shift of each line also increases progressively as shown in Figs. 49(a), (b), and (c). As mentioned earlier, the differential phase shifts of 70, 140, and 210º for the line L1, L2, and L3 at 10GHz are the designed values when applied voltage is 90 V. Measured results at 90 V are shown in Fig. 49(c), and they are compared to the simulated results carried out by Ansoft's High Frequency Structure Simulator (HFSS). Good agreement has been achieved between the measured and the simulated results. However, the losses of the meandered microstrip line, shown in Fig. 48, result in the nonlinear increase of the differential phase shifts particularly in the region of frequencies higher than about 10 GHz.

In Fig. 50, differential phase shifts vs. applied voltages are shown for 6, 10, and 12.5 GHz. Differential phase shifts of about 114, 201, and 336º are achieved at 12.5 GHz

under the maximum perturbation. Specially, Fig. 50(b) compares the measured results of meandered microstrip lines with those of straight microstrip lines in [52]. In this figure,

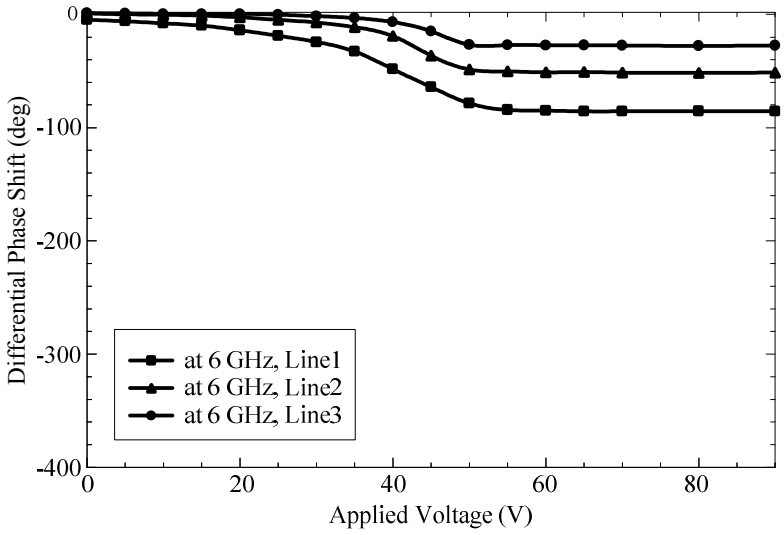

(a)

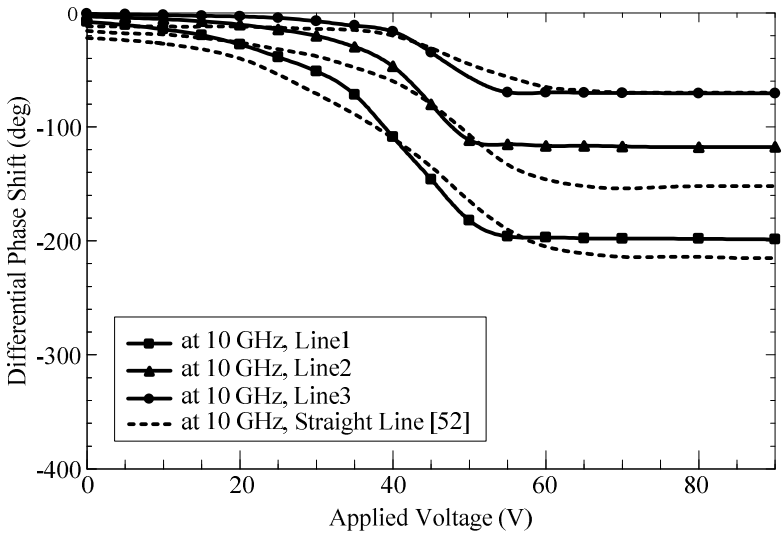

(b)

Fig. 50. Differential phase shifts with respect to the line 4 versus applied voltage at different frequencies. (a) 6 GHz. (b) 10 GHz. (c) 12.5 GHz.

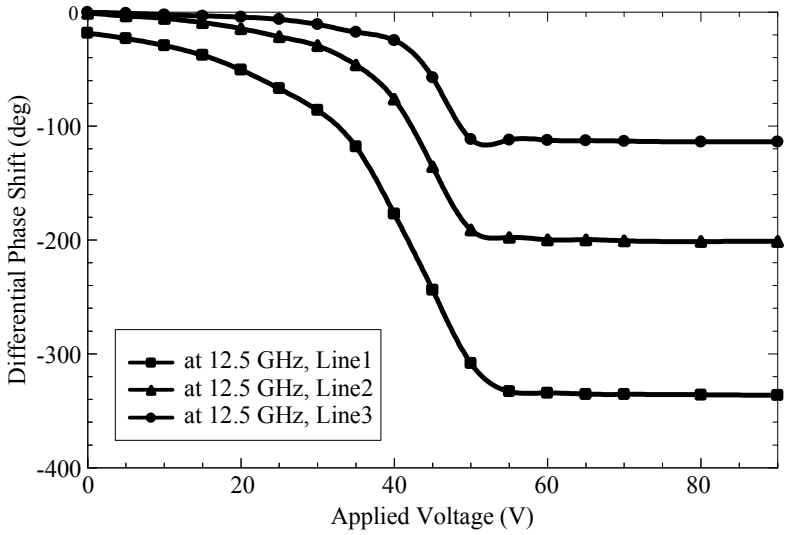

(c)

Fig. 50. Continued.

phase shifts in line L2 and L3 are slightly deviated from those of straight lines mainly over 55 V. Except for this minor difference, progressive variations of the differential phase shifts are very similar to those results from straight microstrip lines. Besides, the required bias voltage is only up to 60 V in the same way for the straight microstrip lines, as shown in Fig. 50.

4. Conclusion

A miniaturized phase shifter using meandered microstrip lines controlled by a PET has been demonstrated. Simulation results of the differential phase shifts at the maximum perturbation agree very well with the measured data. Compared to the conventional phase shifter using straight microstrip lines, comparable differential phase shifts are achieved. In the longitudinal direction, the length of the novel circuit is

reduced to 1/3, and the response time or scan speed of the antenna systems could be improved by the weight reduction of the dielectric perturber.

CHAPTER VI

A REFLECTION-TYPE PHASE SHIFTER CONTROLLED BY A PIEZOELECTRIC TRANSDUCER*

1. Introduction

The concept of using dielectric perturbation controlled by a piezoelectric transducer (PET) in analog phase shifters is useful in applications demanding the characteristics of wide bandwidths, low losses, and low cost [48], [52], [54]. The size of air gap between a dielectric perturber attached to the PET and microstrip lines can be varied by applied DC voltage, and this changes the propagation constant of microstrip lines. In order to take advantage of constant insertion loss over a wide phase tuning range, reflection-type phase shifters using quadrature couplers and varactors were proposed [55], [56]. These phase shifters are operating at a fixed frequency, and an optimal equalization resistance is necessary for minimizing the insertion-loss variation.

In this chapter, the reflection-type phase shifter using a quadrature coupler tuned by the PET is introduced. The dielectric perturber is used to perturb two reflection loads of the quadrature coupler for achieving differential phase shifts at 9.7GHz with low insertion losses and low insertion-loss variations. The quadrature coupler combines the reflected signals from the open-circuited microstrip lines under the dielectric

perturbation. Compared to solid-state tunable phase shifters, this phase shifter has the advantages of high power handling capabilities and simple bias schemes.

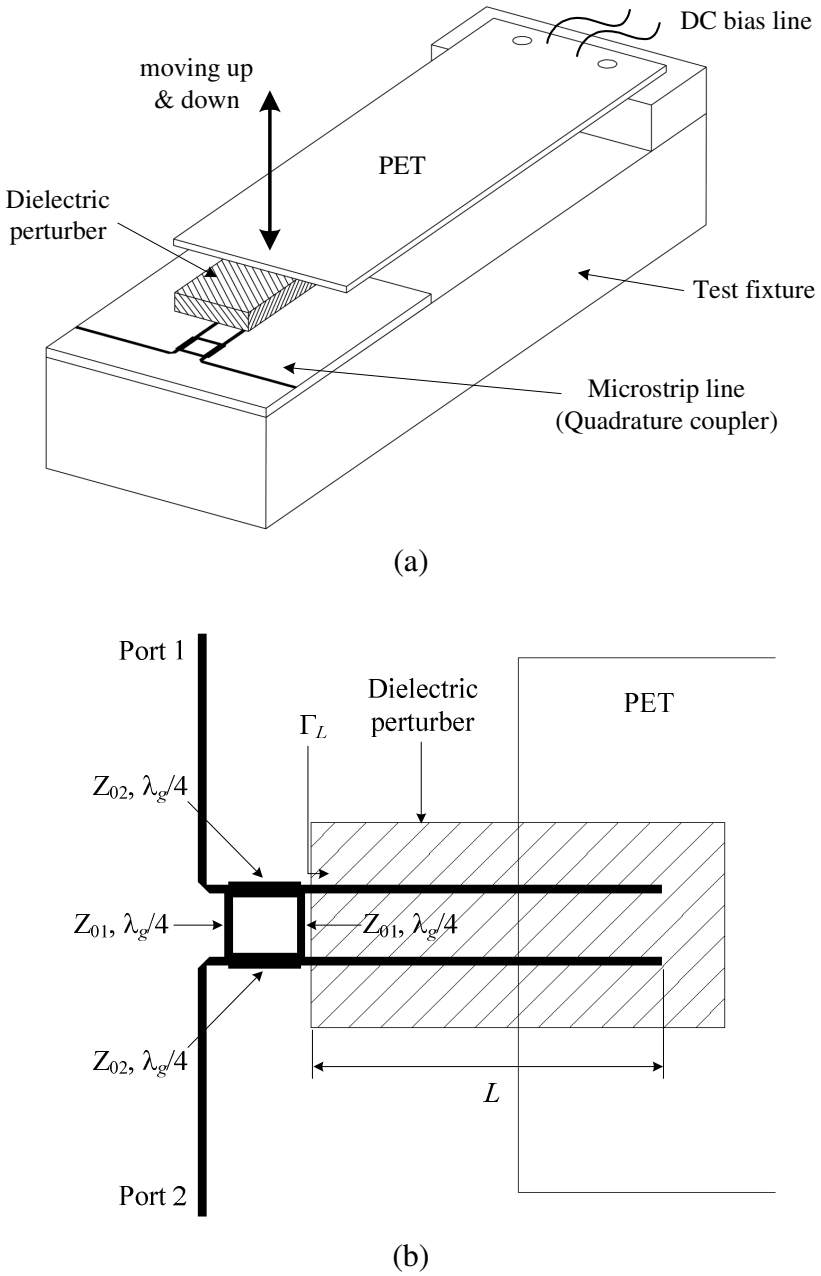

Fig. 51. Configuration of the reflection-type phase shifter controlled by a PET. (a) Three-dimensional view. (b) Top view.

2. Phase shifter design

Fig. 51(a) shows the configuration of the proposed phase shifter, which consists of a microstrip quadrature coupler and a dielectric perturber. The dielectric perturber gives perturbation on two open-circuited microstrip lines, which are the reflection loads of the quadrature coupler. The perturber moves down to microstrip lines as the applied voltage is increased up to 100 V. According to this variation, the size of air gap between the microstrip line and the perturber is reduced and the line capacitance is increased [51]. As a result, the variations in the effective dielectric constant caused by the capacitance variations give rise to the phase shift to the output port. Fig. 51(b) shows the top view of the proposed phase shifter, where Z_{01} and Z_{02} are the characteristic impedances of each branch of the quadrature coupler, L is the length of the microstrip line under the dielectric perturbation, and λ_g is the guided wavelength of the desired frequency. Following the similar procedures in [55], S_{21} and its phase can be expressed as, respectively,

$$S_{21} = j\alpha^2\Gamma_L = j\alpha^2 \exp(-2j\beta L) = j\alpha^2 \exp\left(-2j\frac{2\pi}{\lambda_0}\sqrt{\varepsilon_{eff}}L\right) \tag{18}$$

$$\angle S_{21} = \frac{\pi}{2} + \left(-\frac{4\pi}{\lambda_0}\sqrt{\varepsilon_{eff}}L\right) \tag{19}$$

where α is the loss of the quadrature coupler, which is equal to 1 for the ideal coupler, β is the propagation constant, ε_{eff} is the effective relative dielectric constant of the microstrip line, λ_0 is the free-space wavelength, and Γ_L is the reflection coefficient of the one reflection load with the length of L as shown in Fig. 51(b). A differential phase shift,

defined as the phase of the perturbed microstrip lines with respect to the phase of unperturbed microstrip lines, can be calculated as

$$\Delta\phi = \angle S_{21,\,pert} - \angle S_{21,unpert} = -\frac{4\pi}{\lambda_0} L\left(\sqrt{\varepsilon_{eff\,,\,pert}} - \sqrt{\varepsilon_{eff\,,unpert}}\right)$$
$$= 2 \cdot L \cdot \frac{2\pi}{\lambda_0}\left(\sqrt{\varepsilon_{eff\,,unpert}} - \sqrt{\varepsilon_{eff\,,\,pert}}\right) \tag{20}$$

where $\varepsilon_{eff,\ unpert}$ and $\varepsilon_{eff,\ pert}$ are the effective relative dielectric constants of the unperturbed and perturbed microstrip line, respectively. Usually, because $\varepsilon_{eff,\ pert}$ is larger than $\varepsilon_{eff,\ unpert}$, $\Delta\phi$ has a negative value. The first "2" in the result of (20) is due to the assumption of total reflection from the open-circuited microstrip lines and the ideal 3 dB coupler. Moreover, the "2" represents exactly double the phase shifts resulting from the conventional PET-controlled phase shifters [48], [52], [54].

The proposed phase shifter is fabricated on a 15 mil-thick RT/Duroid 6010.2 substrate with a relative dielectric constant of 10.2. Each branch of the coupler is a quarter-wavelength microstrip line, which has the characteristic impedance of 50 and $50/\sqrt{2}$ Ω for Z_{01} and Z_{02}, respectively, as shown in Fig. 51(b). The dimensions of each branch of the quadrature coupler are 0.33 mm × 3.1 mm for the Z_{01}-microstrip line and 0.65 mm × 3.1 mm for the Z_{02}-microstrip line. For the microstrip lines of two ports and two open-circuited reflection loads, 50 Ω lines are used. The dielectric perturber is 1.27 mm thick with a relative dielectric constant of 10.2, and PET has the size of 70 mm × 32 mm × 0.635 mm. The perturbed length L in Fig. 51(b) is selected as 15 mm for measurements. The fabricated reflection-type phase shifter is shown in Fig. 52.

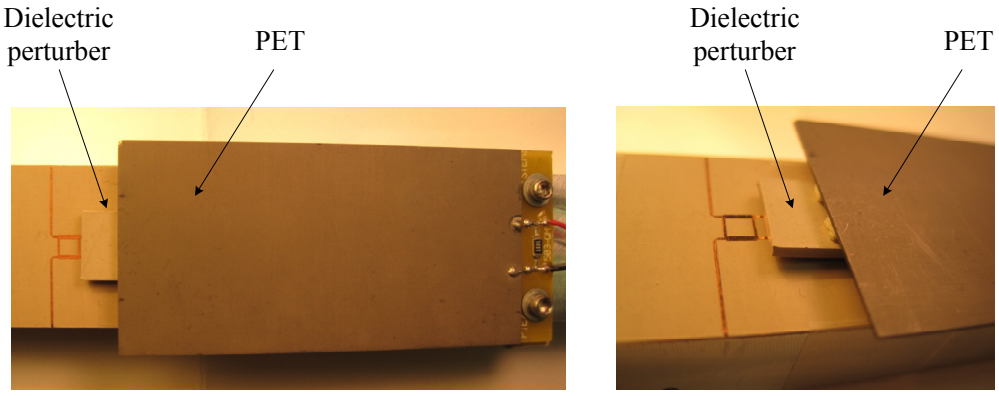

Fig. 52. A fabricated reflection-type phase shifter controlled by a PET.

3. Phase shift analysis and measurement

Fig. 53 shows that the insertion loss (S_{21}) is less than 1.85 dB and the return loss (S_{11}) is better than 14.2 dB at 9.7 GHz during the variation of the applied voltage. Specially, the variation of the insertion loss (S_{21}) is within ± 0.46 dB at 9.7 GHz. Fig. 54(a) shows the measured relative phase shifts, and Fig. 54(b) shows the measured differential phase shifts, defined in (20). The maximum measured differential phase shift is observed as 132º, and the maximum value calculated from (20) is 152º at 9.7 GHz. For this calculation, electromagnetic (EM) simulation software Zeland IE3D is used. The imperfect contact between the microstrip line and the dielectric perturber at the maximum voltage could be considered as one of the reasons for this difference. In Fig. 54(c), the differential phase shifts versus applied voltages are shown for 9.5, 9.7 and 9.9 GHz. The differential phase shifts vary slowly from 0 to 30 V, and then show very significant variations from 30 to 60 V. The maximum differential phase shifts for each frequency are 114, 132, and 140º when the applied voltage is 100 V.

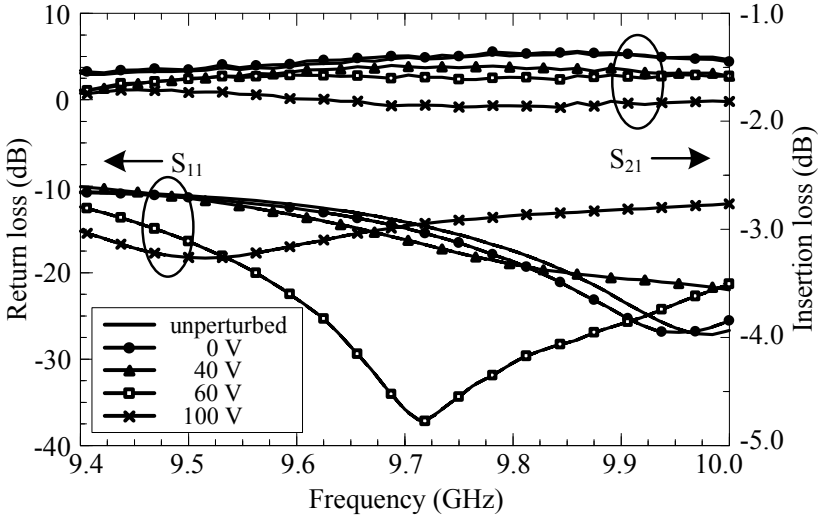

Fig. 53. Measured S-parameters at different applied voltages.

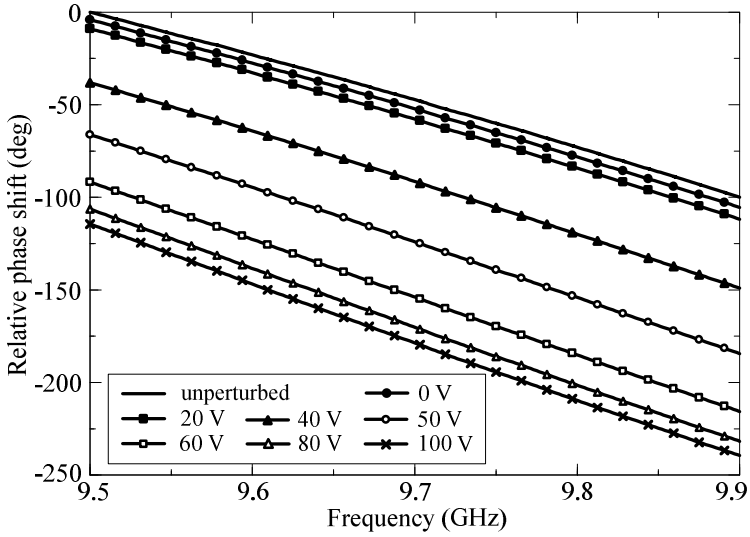

(a)

Fig. 54. Measured phase shifts. (a) Relative phase shifts versus frequency. (b) Differential phase shifts versus frequency. (c) Differential phase shifts versus applied voltage.

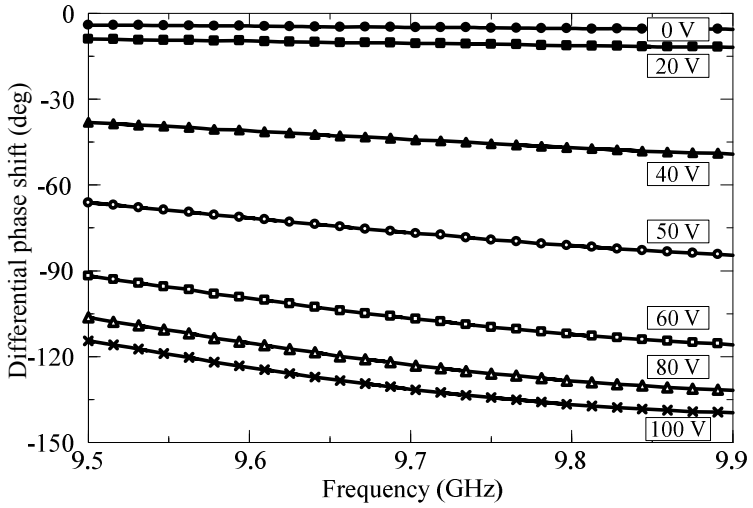

(b)

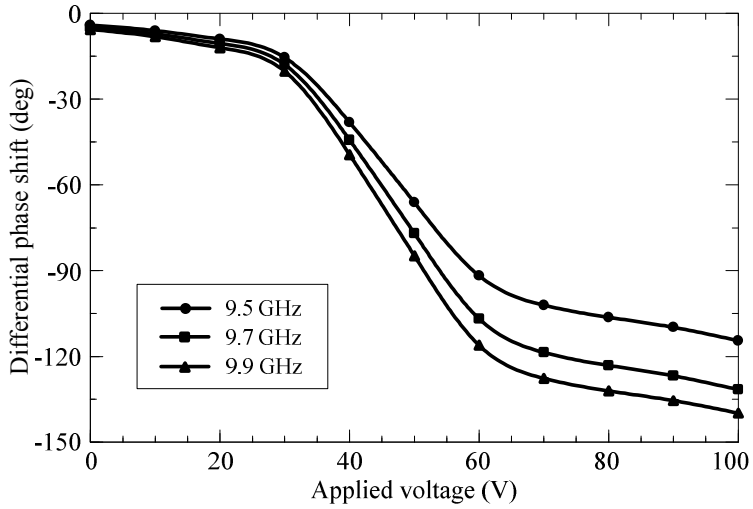

(c)

Fig. 54. Continued.

4. Conclusion

A tunable reflection-type phase shifter using the PET has been presented. By giving perturbation on two open-circuited microstrip lines at the same time, double phase shifts are achieved by calculation compared to the conventional microstrip line perturbation using the PET. While the applied voltages to the PET are varied, the

differential phase shifts are produced by the perturbation. The maximum value is 132º at 9.7 GHz, which is about 15% lower than the calculated result. At this frequency, the variation of the insertion loss (S_{21}) is just within ± 0.46 dB, and the insertion loss (S_{21}) and the return loss (S_{11}) are better than 1.85 dB and 14.2 dB, respectively.

CHAPTER VII

IMAGE-GUIDE LEAKY-WAVE ANTENNAS WITH WIDE BEAM-SCAN ANGLE*

1. Introduction

Dielectric leaky-wave antennas have been interesting topics for its high beam-scan ability at millimeter wave frequencies as well as the characteristics of low losses, lightweight and easy fabrication. In previous researches, PIN diodes were attached to the metal strips [57] or on the sidewalls of the guide [58] for realizing switchable main-beam angles at a fixed frequency operation. Recently, moveable grating films on the image line antenna were demonstrated [59]. This antenna system has a wide beam-scan angle, which is asymmetrical to the broadside beam. A dual-beam grating antenna was introduced later with wide and symmetrical beam-steering angle to the broadside beam [60], but this antenna needs two beamports and a microwave combiner to combine power passing through the beamports.

This chapter presents a dielectric film with metal strips fed by the image line made of a high dielectric constant material. By using a 10.8 relative dielectric constant image line, wide and symmetrical beam-steering angle is achieved with a simple structure. Antenna size is also reduced as compared to the image line antenna made of a low dielectric constant material [59].

---

2. Antenna design concept

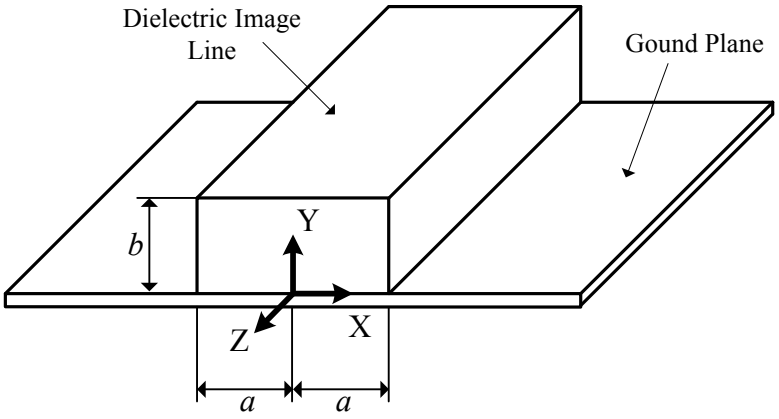

Fig. 55. Configuration of an image line.

A dielectric image guide line, shown in Fig. 55, is made of a material with a relative dielectric constant ε_r, width $2a$, height b, lying on a perfectly conducting ground plane. This structure supports $E_{mn}^{\ y}$ mode [61], whose transverse field components are E_y and H_x. The transverse propagation constants in the x and y direction are denoted by k_x and k_y, respectively, and can be expressed by [61]

$$ak_x = \frac{m\pi}{2} - \tan^{-1}\left(\frac{k_x}{k_{x0}}\right), \qquad m = 1,2,3,... \tag{21}$$

$$bk_y = \frac{n\pi}{2} - \tan^{-1}\left(\frac{k_y}{\varepsilon_r k_{y0}}\right), \qquad n = 1,2,3,... \tag{22}$$

where

$$k_{x0} = [(\varepsilon_{re} - 1)k_0^{\ 2} - k_x^{\ 2}]^{1/2},$$

$$k_{y0} = [(\varepsilon_r - 1)k_0^{\ 2} - k_y^{\ 2}]^{1/2},$$

$$\varepsilon_{re} = \varepsilon_r - (k_y / k_0)^2,$$

$$k_0 = \frac{2\pi}{\lambda_0}.$$

λ_o and ε_r are the free-space wavelength and the relative dielectric constant, respectively. After obtaining k_x and k_y from the previous equations, the longitudinal propagation constant in the z direction is expressed by

$$k_z = (\varepsilon_{re} k_0^{\,2} - k_x^{\,2})^{1/2} = (\varepsilon_r k_0^{\,2} - k_x^{\,2} - k_y^{\,2})^{1/2} \tag{23}$$

and the longitudinal guided wavelength can be calculated by

$$\lambda_g = 2\pi / k_z. \tag{24}$$

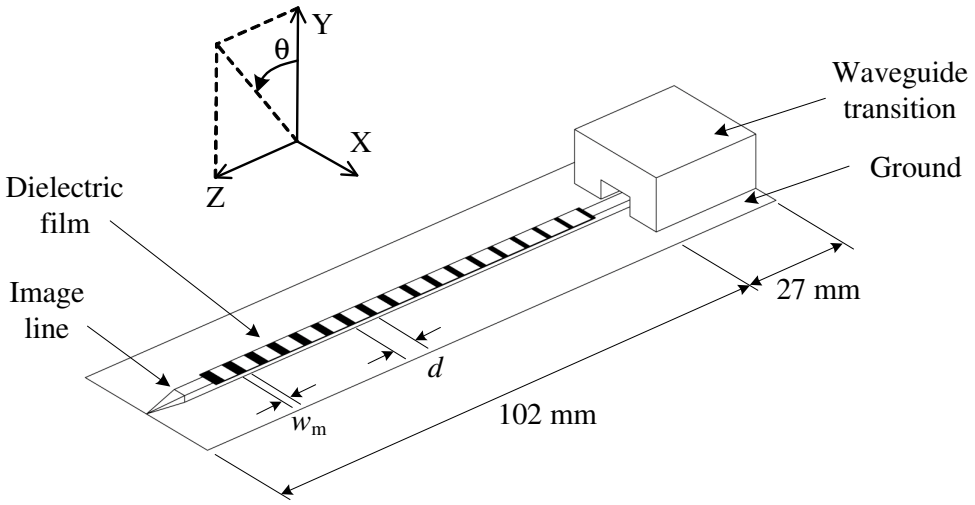

Fig. 56. Antenna configuration.

The leaky-wave antenna in this chapter uses metal strips on top of the image line as a perturbation, which causes energy to be radiated as a fan-shaped beam into space. The configuration of the proposed leaky-wave antenna is shown in Fig. 56. Metal strips

are etched along the bottom of the thin and narrow dielectric film, and they are illustrated as if they were visible in the figure. The calculated value of λ_g from (24) helps to determine the angle of radiation of the leaky-wave antenna beam, which is given by

$$\theta = \sin^{-1}(\lambda_o / \lambda_g + n\lambda_o / d) \tag{25}$$

where d is the metallic strip spacing, and n is the index of the space harmonic (0, ±1, ±2,…), which is conventionally chosen as -1 [62]. Therefore, for the leaky-wave antenna, which uses the proposed image line and operates at a certain frequency, the angle of the radiated beam can be controlled by using the metallic strip spacing d, as shown in Fig. 56. Alternating the films, which have different strip spacing d, shifts the main-beam angle along Θ in y-z plane. For better contact between metal strips and the dielectric image line, a water-soluble low-loss glue is used while in the antenna measurement.

As far as the grating lobes in the visible range are concerned, the research results in [62] are useful to achieve low level of the grating lobes. Fig. 57 shows the relation between d / λ_o and r (= λ_o / λ_g), in which five kinds of curved lines are drawn by taking advantage of the equations in [62]. In this figure, according to the variation of d, the beam-scan angle changes vertically at a certain value of r, which depends on a, b, ε_r, and the operating frequency. From the analyses of this figure, it is advantageous to choose d from the shaded area for the lowest level of grating lobes. The high dielectric constant is more favorable for achieving wide scan-angle because the high dielectric constant means large r. When r is larger than about 3.0, the shaded area supports full beam-scan angle in the visible region. Thus, the appropriate choice of the cross-section dimensions and the high dielectric constant of the image line would make the antenna beam steer fully

between endfire angle (Θ = 90º) and backfire angle (Θ = -90º) without seeing any grating lobe.

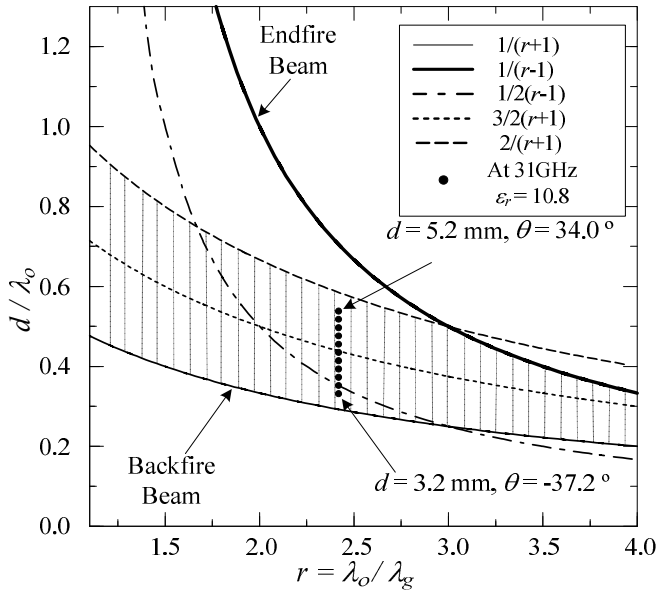

Fig. 57. Range of d / λ_o [62]. Solid circles represent calculated results in measuring condition.

The size of the cross section of the image line is one of the parameters that affect the operating frequency range. From the results in [61], the widest separation between the propagation modes is provided by the cross section for which $a / b = 1$, so we choose 1.27 mm for both a and b of the image line. Since increasing the relative dielectric constant has the effect of decreasing the frequency range for a single mode operation, 10.8 is chosen as the relative dielectric constant. Fig. 58 shows the resulting dispersion curves of E_{11}^{y} and E_{21}^{y} modes. The single mode-operating band appears approximately from 18 GHz to 30 GHz.

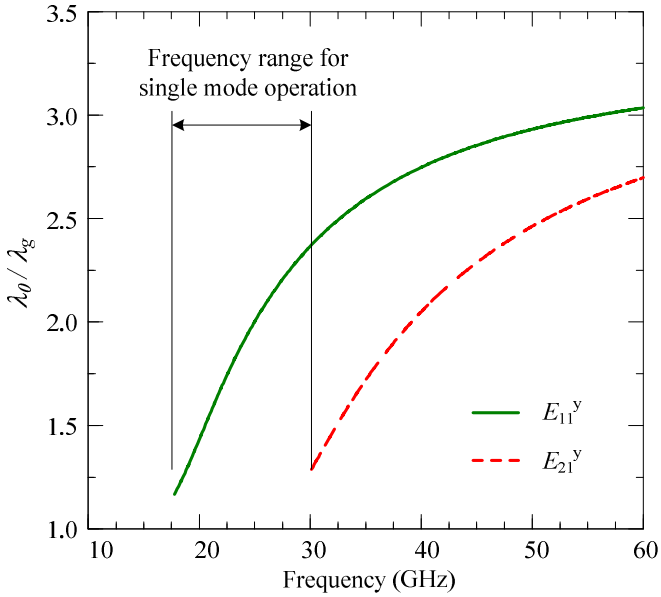

Fig. 58. Dispersion curves for the image line with ε_r = 10.8, a = 1.27 mm, b = 1.27 mm.

To increase the efficiency of converting the guided energy into a radiated beam, the width of the mth strip w_m, as shown in Fig. 56, is calculated using the following empirical relation [63]:

$$w_m = \begin{cases} (0.15 + 0.015(m-1))\lambda_g, & for \;\; m \le 18 \\ 0.4\lambda_g, & for \;\; m > 18 \end{cases} \tag{26}$$

where λ_g is assumed to be equal to d in calculating w_m for each film.

3. Theoretical and experimental results

The dimension of the proposed antenna is shown in Fig. 56. The image line is fabricated from RT/Duroid 6010 (ε_r = 10.8) and attached to an aluminum ground plane using the low-loss epoxy. The thin dielectric film is fabricated from 0.127- mm thick

RT/Duroid 5880 (ε_r = 2.2) and approximately 5-mm wide and 80-mm long. A three-section waveguide transition method [64] is used, and Arc DD-10214 silicon absorber is used to reduce the reflection from the end of the image line. The fabricated antenna and the constituent parts are shown in Figs. 59(a) and (b), respectively.

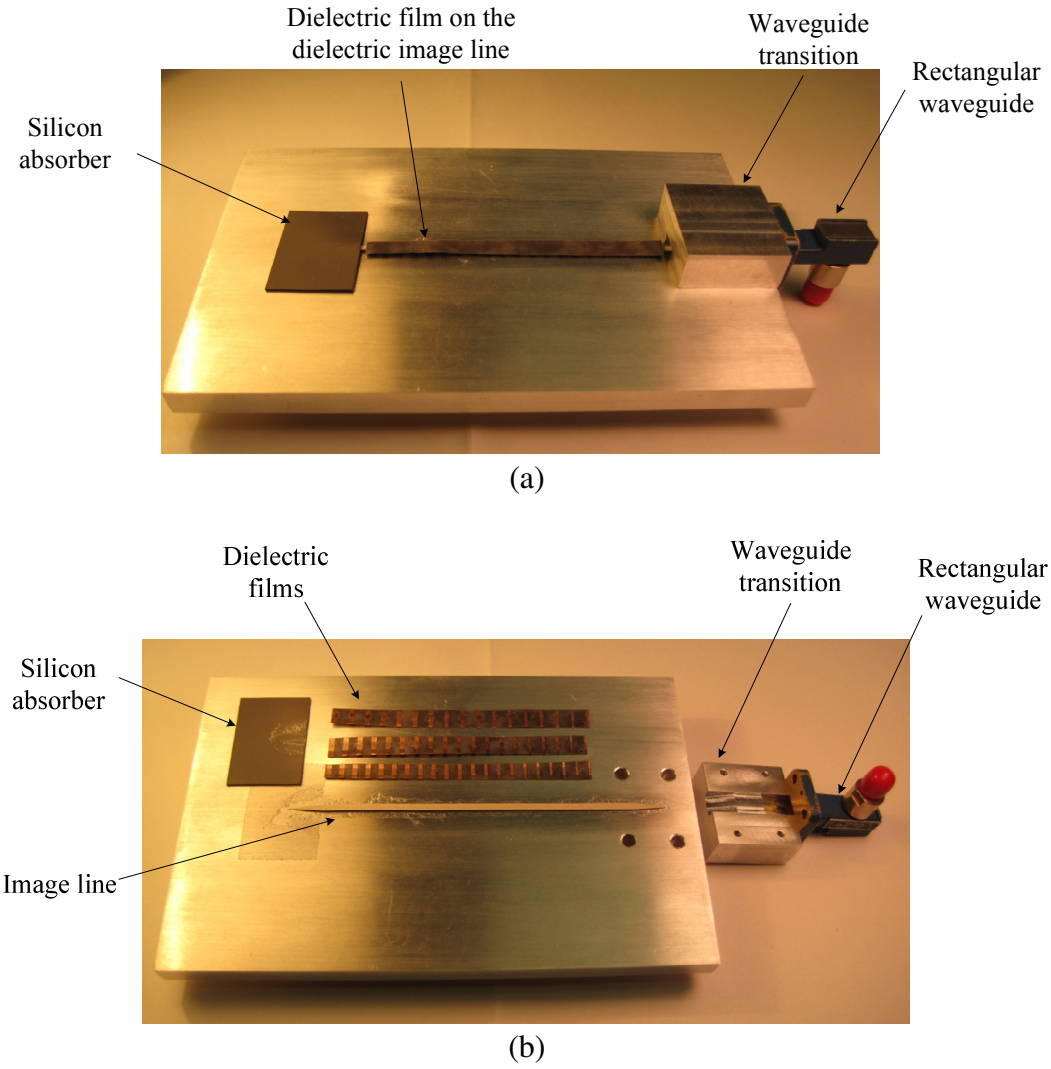

Fig. 59. Configuration of an image-guide leaky-wave antenna. (a) A fabricated antenna. (b) Parts of the antenna.

The radiation patterns of the antenna are measured at 31 GHz, and Fig. 60 compares the measured and calculated main-beam angles as strip spacing *d* is varied. Measured results agree very well with the calculated data. The range of strip spacing *d* for effective radiation is determined to be from 3.2 mm to 5.2 mm, which is confirmed to be in the shaded range in Fig. 57. The solid circles in Fig. 57 represent the calculated results using the parameters of the proposed antenna such as the 10.8 relative dielectric constant, the 1.27 × 2.54 mm cross-section image line, and the 31-GHz operating frequency for the 11-different strip spacing.

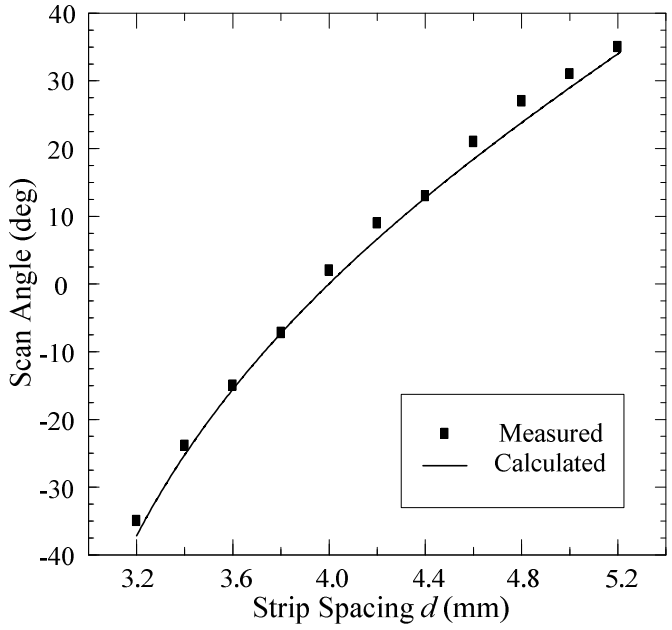

Fig. 60. Measured and calculated beam-scan angle along Θ at 31 GHz.

Fig. 61 illustrates the overlap of the *E*-plane radiation patterns measured by using 11 dielectric films with different strip spacings. Beam-steering angle of 70 degrees

which is approximately symmetric to the broadside radiation (Θ = 0º) is achieved including the results of 3.2-mm and 5.2-mm strip spacings in the figure. The average of isotropic gains is 10.47 dBi and the average of 3-dB beamwidth is 9.29 degrees. Compared to the leaky-wave antenna with a low dielectric constant material [59], the gain becomes lower and 3-dB beamwidth becomes wider, resulting from the smaller aperture size of the proposed antenna. The average of the sidelobe level is greater than 9.78 dB below the main beam. Cross polarization level at the main-beam angle is about 22 dB down for the 4.2-mm strip spacing. Fig. 62 shows the measured isotropic gain of the main beam and the return loss as *d* is varied. The return losses are better than 14.9 dB across the beam-scan region, and the gain has the highest value as 14.82 dBi when the return loss is at the lowest level as 26 dB.

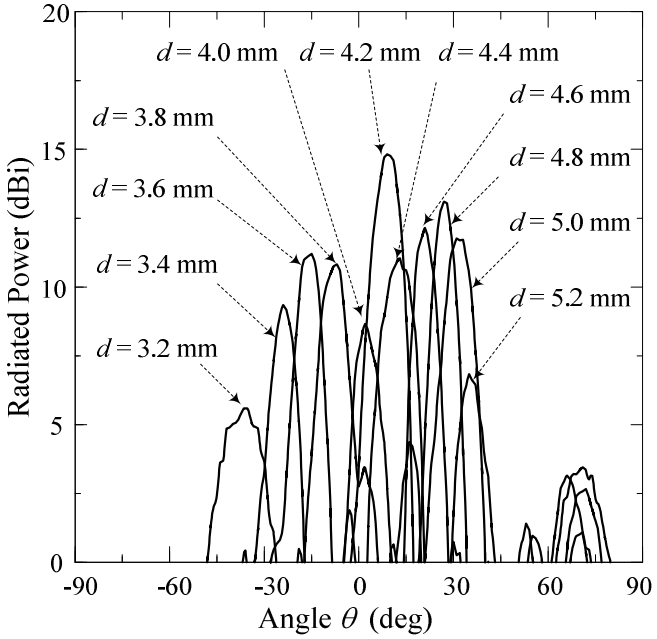

Fig. 61. Overlap of *E*-plane radiation patterns as strip spacing *d* is changed at 31 GHz.

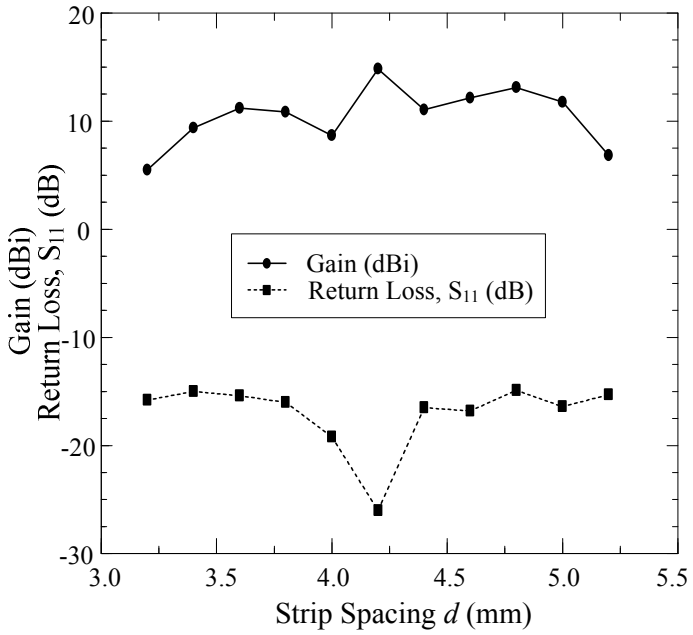

Fig. 62. Isotropic gain and input return loss at 31 GHz.

4. Conclusion

A leaky-wave antenna with the image line made of a 10.8-relative dielectric constant material has been described. After considering both the single mode operation and the wide beam-scan angle of the radiated beam, the size of the cross section and the relative dielectric constant of the image line are decided. Alternating the films with different strip spacing d varies the main-beam angle in the E-plane effectively. Due to the high dielectric constant of the image line, 70-degree beam-scan angle is achieved with the steering angle approximately symmetric to the broadside radiation.

CHAPTER VIII

SUMMARY

In this dissertation, reconfigurable microstrip bandpass filters and microwave components to achieve a scanning antenna beam such as phase shifters using piezoelectric transducers and image-guide leaky-wave antennas have been studied.

In Chapter II, wideband ring bandpass filters using multiple stepped-impedance stubs and interdigital-coupled feed lines have been demonstrated. Through the analyses of the resonant frequencies and transmission zeros, the stepped impedance stubs are designed. Especially, optimized lengths of each section of the stubs are determined for the separate control of mid-lower and mid-upper passband bandwidths. The length of the interdigital-coupled feed lines is adjusted to suppress unwanted harmonic resonances, resulting in a wide upper stopband. PIN diodes controlling input impedances of the multiple open stubs cause narrow or wide passband bandwidths. The measured passband switching ratio is 1.22:1.13:1.

In Chapter III, the ring resonator bandpass filters with open-circuited stubs are developed to be applied to the ultra wideband spectrum. The analyses of the equivalent circuits show that the ring resonator with the high characteristic impedance has the characteristics of the wide bandwidth. The interdigital-coupled feed lines with asymmetric structures are developed to create a notch band at 5.41 GHz to avoid the interference with the WLAN signals.

In Chapter IV, dual-band (2.4 and 5.2 GHz) bandpass filters using asymmetric stepped impedance resonators (SIRs) have been demonstrated to have each band appear or disappear separately. To decide the precise location of the transmission zeros, the external quality factor (Q_{EX}) of the resonators at the 50-Ω port needs to be fixed. When Q_{EX} = 1, the supplemented flowchart is very useful for extracting the exact transmission zeros. Unwanted harmonic resonances are suppressed by the transmission zeros created by the extended feed lines. A little bit different extending amount of the input and output feed lines gives the effective suppression by creating two little different transmission zeros. In order to achieve the coupling coefficients and the external quality factors, several design graphs are drawn by using the extracted simulation data. Hook- and spiral-type feed lines have been developed, and PIN diodes are used to switch on or off each band separately.

In Chapter V, the phase shifter using meandered microstrip lines under the perturbation of a piezoelectric transducer (PET) has been demonstrated. Because of the geometric characteristics of the meandered lines, the insertion loss increases rapidly when frequency becomes higher than approximately 10 GHz. Differential phase shifts also show the characteristics of a nonlinear increase over the same frequency region because of the increase of the losses. However, up to 10 GHz, comparable differential phase shifts are achieved when compared to those of the conventional phase shifter using the perturbation on the straight microstrip lines. The meandered microstrip lines used in the demonstrated phase shifter result in the realization of the compact-size phase shifter circuits.

In Chapter VI, the PET perturbation has been applied to the reflection-type phase shifter. Two open-circuited microstrip lines, perturbed at the same time, create double phase shifts compared to the conventional single line perturbation at 9.7 GHz.

In Chapter VII, leaky-wave antennas using an image line made of a 10.8-relative dielectric constant material have been discussed to achieve symmetric wide beam-scan angle to the broadside radiation. Both the cross-section dimensions and the relative dielectric constant of the image line affect the frequency band of single mode operation and the scan angle of the radiated beam. Main-beam angle varies in the *E*-plane by alternating the spacing of the metal strips, and approximately symmetric 70-degree beam-scan angle is achieved to the broadside radiation.

REFERENCES

[1] K. Chang, "Antenna systems," in *RF and Microwave Wireless Systems*. New York: Wiley, 2000, ch. 3, pp. 67–110.

[2] M. Makimoto and S. Yamashita, "Bandpass filters using parallel coupled stripline stepped impedance resonators," *IEEE Trans. Microw. Theory Tech.*, vol. 28, no. 12, pp. 1413–1417, Dec. 1980.

[3] L. Zhu, S. Sun, and W. Menzel, "Ultra-wideband (UWB) bandpass filters using multiple-mode resonator," *IEEE Microw. Wireless Compon. Lett.*, vol. 15, no. 11, pp. 796–798, Nov. 2005.

[4] Y.-C. Chiou, J.-T. Kuo, and E. Cheng, "Broadband quasi-chebyshev bandpass filters with multimode stepped-impedance resonators (SIRs)," *IEEE Trans. Microw. Theory Tech.*, vol. 54, no. 8, pp. 3352–3358, Aug. 2006.

[5] Y.-C. Chiou, Y.-F. Lee, J.-T. Kuo, and C.-C. Chen, "Planar multimode resonator bandpass filters with sharp transition and wide stopband," in *Proc. IEEE MTT-S Int. Microw. Symp. Dig.*, 2008, pp. 439–442.

[6] Y.-C. Chang, C.-H. Kao, M.-H. Weng, and R.-Y. Yang, "Design of the compact wideband bandpass filter with low loss, high selectivity and wide stopband," *IEEE Microw. Wireless Compon. Lett.*, vol. 18, no. 12, pp. 770–772, Dec. 2008.

[7] M. Matsuo, H. Yabuki, and M. Makimoto, "Dual-mode stepped impedance ring resonator for bandpass filter applications," *IEEE Trans. Microw. Theory Tech.*, vol. 49, no. 7, pp. 1235–1240, Jul. 2001.

[8] J. T. Kuo and C.-Y. Tsai, "Periodic stepped-impedance ring resonator (PSIRR) bandpass filter with a miniaturized area and desirable upper stopband characteristics," *IEEE Trans. Microw. Theory Tech.*, vol. 54, no. 3, pp. 1107–1112, Mar. 2006.

[9] L.-H. Hsieh and K. Chang, "Compact, low insertion-loss, sharp-rejection, and

wideband microstrip bandpass filters," *IEEE Trans. Microw. Theory Tech.*, vol. 51, no. 4, pp. 1241–1246, Apr. 2003.

[10] Y.-Z. Wang, C.-A. Wang, and K.-Y. Lin, "Miniaturized dual-mode quasi-elliptic function bandpass filter with wide rejection bandwidth," in *Proc. Asia-Pacific Microw. Conf.*, 2006, pp. 1569–1574.

[11] S. Sun and L. Zhu, "Wideband microstrip ring resonator bandpass filters under multiple resonances," *IEEE Trans. Microw. Theory Tech.*, vol. 55, no. 10, pp. 2176–2182, Oct. 2007.

[12] C. H. Kim and K. Chang, "Wideband ring resonator bandpass filter with dual stepped impedance stubs," in *Proc. IEEE MTT-S Int. Microw. Symp. Dig.*, 2010, pp. 229–232.

[13] K. Chang, *Microwave Ring Circuits and Antennas*. New York: Wiley, 1996.

[14] K. Chang and L.-H. Hsieh, *Microwave Ring Circuits and Related Structures*. New York: Wiley, 2004.

[15] C. Rauscher, "Reconfigurable bandpass filter with a three-to-one switchable passband width," *IEEE Trans. Microw. Theory Tech.*, vol. 51, no. 2, pp. 573–577, Feb. 2003.

[16] C. Lugo and J. Papapolymerou, "Electronic switchable bandpass filter using PIN diodes for wireless low cost system-on-a-package applications," *Proc. Inst. Electr. Eng.-Microw. Antennas Propag.*, vol. 151, no. 6, pp. 497–502, Dec. 2004.

[17] C. Lugo and J. Papapolymerou, "Single switch reconfigurable bandpass filter with variable bandwidth using a dual-mode triangular patch resonator," in *Proc. IEEE MTT-S Int. Microw. Symp. Dig.*, 2005, pp. 779–782.

[18] W.-H. Tu, "Compact low-loss reconfigurable bandpass filter with switchable bandwidth," *IEEE Microw. Wireless Compon. Lett.*, vol. 20, no. 4, pp. 208–210, Apr. 2010.

[19] A. Miller and J.-S. Hong, "Wideband bandpass filter with reconfigurable

bandwidth," *IEEE Microw. Wireless Compon. Lett*., vol. 20, no. 1, pp. 28–30, Jan. 2010.

[20] M. Sanchez-Renedo, R. Gomez-Garcia, J. I. Alonso, and C. Briso-Rodriguez, "Tunable combline filter with continuous control of center frequency and bandwidth," *IEEE Trans. Microw. Theory Tech*., vol. 53, no. 1, pp. 191–199, Jan. 2005.

[21] Federal Communications Commission, "Revision of part 15 of the commission's rules regarding ultra-wideband transmission systems," FCC, Washington, DC, Tech. Rep. ET-Docket 98-153, FCC02-48, Apr. 2002.

[22] H. Shaman and J.-S. Hong, "Ultra-wideband (UWB) bandpass filter with embedded band notch structures," *IEEE Microw. Wireless Compon. Lett*., vol. 17, no. 3, pp. 193–195, Mar. 2007.

[23] S. W. Wong and L. Zhu, "Implementation of compact UWB bandpass filter with a notch-band," *IEEE Microw. Wireless Compon. Lett*., vol. 18, no. 1, pp. 10–12, Jan. 2008.

[24] G.-M. Yang, R. Jin, C. Vittoria, V. G. Harris, and N. X. Sun, "Small ultra-wideband (UWB) bandpass filter with notched band," *IEEE Microw. Wireless Compon. Lett*., vol. 18, no. 3, pp. 176–178, Mar. 2008.

[25] Z.-C. Hao, J.-S. Hong, J. P. Parry, and D. P. Hand, "Ultra-wideband bandpass filter with multiple notch bands using nonuniform periodical slotted ground structure," *IEEE Trans. Microw. Theory Tech*., vol. 57, no. 12, pp. 3080–3088, Dec. 2009.

[26] R. Li and L. Zhu, "Compact UWB bandpass filter using stub-loaded multiple-mode resonator," *IEEE Microw. Wireless Compon. Lett*., vol. 17, no. 1, pp. 40–42, Jan. 2007.

[27] C. H. Kim and K. Chang, "Ring resonator bandpass filter with switchable bandwidth using stepped-impedance stubs," *IEEE Trans. Microw. Theory Tech*.,

vol. 58, no. 12, pp. 3936–3944, Dec. 2010.

[28] J.-T. Kuo, T.-H. Yeh, and C.-C. Yeh, "Design of microstrip bandpass filters with a dual-passband response," *IEEE Trans. Microw. Theory Tech.*, vol. 53, no. 4, pp. 1331–1337, Apr. 2005.

[29] C.-F. Chen, T.-Y. Huang, and R.-B. Wu, "Design of dual- and triple-passband filters using alternately cascaded multiband resonators," *IEEE Trans. Microw. Theory Tech.*, vol. 54, no. 9, pp. 3550–3558, Sep. 2006.

[30] M.-L. Chuang, M.-T. Wu, and S.-M. Tsai, "Dual-band filter design using L-shaped stepped impedance resonators," *IET Microw. Antennas Propag.*, vol. 4, no. 7, pp. 855–862, 2010.

[31] F.-C. Chen and Q.-X. Chu, "Novel multistub loaded resonator and its application to high-order dual-band filters," *IEEE Trans. Microw. Theory Tech.*, vol. 58, no. 6, pp. 1551–1556, Jun. 2010.

[32] Q.-X. Chu, F.-C. Chen, Z.-H. Tu, and H. Wang, "A novel crossed resonator and its applications to bandpass filters," *IEEE Trans. Microw. Theory Tech.*, vol. 57, no. 7, pp. 1753–1759, Jul. 2009.

[33] S. Luo, L. Zhu, and S. Sun, "A dual-band ring-resonator bandpass filter based on two pairs of degenerate modes," *IEEE Trans. Microw. Theory Tech.*, vol. 58, no. 12, pp. 3427–3432, Dec. 2010.

[34] J. Lee and K. Sarabandi, "A synthesis method for dual-passband microwave filters," *IEEE Trans. Microw. Theory Tech.*, vol. 55, no. 6, pp. 1163–1170, Jun. 2007.

[35] G.-L. Dai, Y.-X. Guo, and M.-Y. Xia, "Dual-band bandpass filter using parallel short-ended feed scheme," *IEEE Microw. Wireless Compon. Lett.*, vol. 20, no. 6, pp. 325–327, Jun. 2010.

[36] X. Y. Zhang and Q. Xue, "Novel centrally loaded resonators and their applications to bandpass filters," *IEEE Trans. Microw. Theory Tech.*, vol. 56, no. 4, pp. 913–

921, Apr. 2008.

[37] X. Y. Zhang and Q. Xue, "High-selectivity tunable bandpass filters with harmonic suppression," *IEEE Trans. Microw. Theory Tech.*, vol. 58, no. 4, pp. 964–969, Apr. 2010.

[38] Y.-S. Lin, P.-Y. Chang, and Y.-S. Hsieh, "Compact electronically switchable parallel-coupled microstrip bandpass filter with wide stopband," *IEEE Microw. Wireless Compon. Lett.*, vol. 18, no. 4, pp. 254–256, Apr. 2008.

[39] J. Lee and K. Sarabandi, "An analytic design method for microstrip tunable filters," *IEEE Trans. Microw. Theory Tech.*, vol. 56, no. 7, pp. 1699–1706, Jul. 2008.

[40] J. S. Hong and M. J. Lancaster, *Microstrip Filters for RF/Microwave Applications*. New York: Wiley, 2001.

[41] M. Matsuo, H. Yabuki, and M. Makimoto, "The design of a half-wavelength resonator BPF with attenuation poles at desired frequencies," in *IEEE MTT-S Int. Microw. Symp. Dig.*, 2000, pp. 1181–1184.

[42] C.-W. Tang and Y.-K. Hsu, "A microstrip bandpass filter with ultrawide stopband," *IEEE Trans. Microw. Theory Tech.*, vol. 56, no. 6, pp. 1468–1472, Jun. 2008.

[43] L.-H. Hsieh and K. Chang, "Dual-mode quasi-elliptic-function bandpass filters using ring resonators with enhanced-coupling tuning stubs," *IEEE Trans. Microw. Theory Tech.*, vol. 50, no. 5, pp. 1340–1345, May 2002.

[44] G. L. Matthaei, L. Young, and E. M. T. Jones, *Microwave Filters, Impedance-Matching Networks, and Coupling Structures*. Dedham, MA: Artech House, 1980, ch. 11, pp. 651–723.

[45] J.-T.Kuo, S.-P. Chen, and M. Jiang, "Parallel-coupled microstrip filters with over-coupled end stages for suppression of spurious responses," *IEEE Microw. Wireless Compon. Lett.*, vol. 13, no. 10, pp. 440–442, Oct. 2003.

[46] M. Jiang, M.-H. Wu, and J.-T. Kuo, "Parallel-coupled microstrip filters with over-coupled stages for multispurious suppression," in *IEEE MTT-S Int. Microw. Symp. Dig*., 2005, pp. 687–690.

[47] S.-C. Lin, "Microstrip dual/quad-band filters with coupled lines and quasi-lumped impedance inverters based on parallel-path transmission," *IEEE Trans. Microw. Theory Tech*., vol. 59, no. 8, pp. 1937–1946, Aug. 2011.

[48] T.-Y. Yun and K. Chang, "A low-loss time-delay phase shifter controlled by piezoelectric transducer to perturb microstrip line," *IEEE Microw. Guided Wave Lett*., vol. 10, no. 3, pp. 96–98, Mar. 2000.

[49] S.-G. Kim, T.-Y. Yun, and Kai Chang, "Time-delay phase shifter controlled by piezoelectric transducer on coplanar waveguide," *IEEE Microw. Wireless Compon. Lett*., vol. 13, no. 1, pp. 19–20, Jan. 2003.

[50] L. Yang, N. Ito, C. W. Domier, N. C. Luhmann, and A. Mase, "20 to 40 GHz beam shaping/steering phased antenna array system using fermi tapered slot antennas," in *IEEE MTT-S Int. Microw. Symp. Dig*., 2007, pp. 1887–1890.

[51] B. Bhat and S. K. Koul, "Unified approach to solve a class of strip and microstrip-like transmission lines," *IEEE Trans. Microw. Theory Tech*., vol. 30, no. 5, pp. 679–686, May 1982.

[52] T.-Y. Yun and K. Chang, "A low-cost 8 to 26.5 GHz phased array antenna using a piezoelectric transducer controlled phase shifter," *IEEE Trans. Antennas Propag*., vol. 49, no. 9, pp. 1290–1298, Sep. 2001.

[53] R. J. P. Douville and D. S. James, "Experimental study of symmetric microstrip bends and their compensation," *IEEE Trans. Microwave Theory Tech*., vol. 26, no. 3, pp. 175–182, Mar. 1978.

[54] T.-Y. Yun, C. Wang, P. Zepeda, C. T. Rodenbeck, M. R. Coutant, M.-Y. Li, and K. Chang, "A 10- to 21-GHz, low-cost, multifrequency, and full-duplex phased-array antenna system," *IEEE Trans. Antennas Propag*., vol. 50, no. 5, pp. 641–650, May

2002.

[55] C.-S. Lin, S.-F. Chang, C.-C. Chang, and Y.-H. Shu, "Design of a reflection-type phase shifter with wide relative phase shift and constant insertion loss," *IEEE Trans. Microw. Theory Tech*., vol. 55, no. 9, pp. 1862–1868, Sep. 2007.

[56] C.-S. Lin, S.-F. Chang, and W.-C. Hsiao, "A full-360° reflection-type phase shifter with constant insertion loss," *IEEE Microw. Wireless Compon. Lett*., vol. 18, no. 2, pp. 106–108, Feb. 2008.

[57] L. Huang, J. C. Chiao, and M. P. De Lisio, "An electronically switchable leaky wave antenna," *IEEE Trans. Antennas Propag*., vol. 48, no. 11, pp. 1769–1772, Nov. 2000.

[58] R. E. Horn, H. Jacobs, E. Freibergs, and K. L. Klohn, "Electronic modulated beam-steerable silicon waveguide array antenna," *IEEE Trans. Microw. Theory Tech*., vol. 28, no. 6, pp. 647–653, June 1980.

[59] C. T. Rodenbeck, M.-Y. Li, and K. Chang, "A novel millimeter-wave beam-steering technique using a dielectric-image line-fed grating film," *IEEE Trans. Antennas Propag*., vol. 51, no. 9, pp. 2203–2209, Sep. 2003.

[60] C. T. Rodenbeck, M.-Y. Li, and K. Chang, "Design and analysis of a reconfigurable dual-beam grating antenna for low-cost millimeter-wave beam-steering," *IEEE Trans. Antennas Propag*., vol. 52, no. 4, pp. 999–1006, Apr. 2004.

[61] R. M. Knox and P. P. Toulios, "Integrated circuits for the millimeter through optical frequency range," in *Proc. Symp. Submillimeter Waves*, 1970, pp. 497–516.

[62] S. Kobayashi, R. Lampe, R. Mittra, and S. Ray, "Dielectric rod leaky-wave antennas for millimeter-wave applications," *IEEE Trans. Antennas Propag*., vol. 29, no. 5, pp. 822–824, Sep. 1981.

[63] T. N. Trinh, R. Mittra, and R. J. Paleta, "Horn image-guide leaky-wave antenna," *IEEE Trans. Microw. Theory Tech*., vol. 29, no. 12, pp. 1310–1314, Dec. 1981.

[64] S. K. Koul, *Millimeter Wave and Optical Dielectric Integrated Guides and Circuits*. New York: Wiley, 1997.

VITA

Chan Ho Kim was born in Republic of Korea. He received two Bachelor of Engineering degrees both in mechanical engineering and in electrical engineering from Chung-Ang University, Seoul, Korea, in 2000 and from Korea University, Seoul, Korea, in 2002, respectively. He received a Master of Science degree in electrical engineering from University of Maryland, College Park, MD, in 2007.

From 2002 to 2003, he was with Samsung Networks Inc., Seoul, Korea, as a computer network engineer. From February to June 2004, he was with Defense Quality Assurance Agency, Seoul, Korea, as a Researcher involved with defense quality management. From February 2005 to May 2007, he was with Cosmic Ray Physics Group, University of Maryland at College Park, as a Research Assistant. From August 2007, he started working towards his Ph.D. degree in electrical engineering at Texas A&M University, College Station, TX, and was advised by Professor Kai Chang in the Electromagnetics and Microwave Laboratory. His research interests include passive and active microwave circuits and phased-array antenna systems. He can be reached through Professor Kai Chang, Department of Electrical and Computer Engineering, Zachry Engineering Center, Texas A&M University, College Station, TX 77843-3128.